

Building Lithium Fluoride Nanoparticle Films for Organic Photovoltaics

by

Taner Aytun

**Submitted to Graduate School of Faculty of Engineering and Natural Sciences
in partial fulfillment of the requirement for the degree of**

Master of Science in Materials Science and Engineering

at

Sabanci University

August 2010

© 2010 Taner Aytun

All rights reserved.

Abstract

Organic solar cells are primarily composed of conjugated carbon based materials which are actively involved in light absorption and charge transfer. Although organic photovoltaics have advantages such as long time stability, cheapness and easy processibility with comparison to their inorganic competitors, due to its low conversion efficiency (5-6%) there is still a need for research to commercialize these devices. Lithium fluoride is commonly used to enhance conversion efficiency and charge injection at electrode bilayers in organic electronics. However, the conventional processing of lithium fluoride typically requires high vacuum methods, such as thermal evaporation.

This thesis focuses on the development of an ambient, solution processable alternative, in which polymeric reverse micelle reactors are used to synthesize lithium fluoride particles. Apart from controlling the synthesis of lithium fluoride nanoparticles, micelles has a role in the deposition of nanoparticles into a well-ordered, two dimensional layer during spin coating on the donor substrate. The formation of lithium fluoride particles inside micelles were proved by electron and x-ray diffraction measurements. To assess the performance of the solution-processed lithium fluoride, inverted device fabrication and comparative work function measurements were carried out together with thermal evaporated lithium fluoride. Both results support the suitability of solution-processed lithium fluoride for electrode bilayers in organic solar cells. Additionally, different nano transfer printing studies were carried out to integrate solution processed lithium fluoride particles to organic devices and further studies are needed to achieve complete transfer.

Özet

Organik güneş pilleri genel olarak konjuge karbon bazlı maddelerden oluşmaktadırlar ve bu maddeler aktif bir şekilde ışığın emilimi ve yük transferinde etkilidirler. Organik güneş pillerinin inorganik güneş pillerine kıyasla uzun süre kararlılık, ucuzluk ve kolay işlenebilirlik gibi avantajları olsa da düşük verimleri (5-6%) sebebiyle bu cihazların ticari önem kazabilmesi için hala araştırmaya ihtiyaç vardır. Lityum florür, organik elektronik cihazlarda verimi ve yük iletimini artırmak için genel olarak kullanılmaktadır. Fakat lityum florürün geleneksel yollardan işlenmesi, ısı buharlaştırma gibi yüksek vakum ortamındaki metodları gerektirmektedir.

Bu tez çalışması alternatif olarak normal hava ortamında, polimerik ters misel reaktörlerin yardımı ile çözeltide hazırlanabilen lityum florür parçacıkların sentezlenmesine yoğunlaşmaktadır. Lityum florürün sentezini yönlendirmesinin dışında miseller, döndürme kaplama yöntemi kullanılarak verici yüzey üzerine nanoparçacıkların iki boyutta düzgün bir dizilimle yerleştirilmesini sağlarlar. Lityum florür parçacıkların miseller içinde oluşumu elektron ve x-ray kırınım teknikleri ile ispatlanmıştır. Çözeltiden hazırlanan lityum florürlerin performansını ölçmek için, bu parçacıklarla ters cihaz düzeni üretilmiştir ve ısı buharlaştırma yolu ile üretilen lityum florür ile karşılaştırmalı iş fonksiyonu ölçümleri yapılmıştır. Her iki sonuç çözeltide hazırlanan lityum florürün organik güneş pillerde kullanıma elverişli olduğunu göstermiştir. Ayrıca çözeltide hazırlanan lityum florür parçacıkları organik cihazlara entegre etmek için farklı nano transfer baskı çalışmaları yapılmıştır ve tam transferin gerçekleştirilmesi için daha fazla çalışma yapılması gereklidir.

Acknowledgements

This Master's thesis carried out in collaboration between Sabanci University (SU) and Max Planck Institute for Metals Research (MPI-MF). Therefore there are several contributors from both institutes.

First and foremost, I would like to express my deep and sincere gratitude to my thesis advisor Prof. Cleva Ow-Yang for her supervision, advices for this research and motivating me throughout my master's studies. Besides teaching me various subjects and techniques, under her guidance I learned as the most important treasure which is 'how to do science'. In addition, in order to enhance the research quality as well as my career, she pushed all the opportunities to the limits in the last five years that we have been working together. Because of her efforts, I was able to have experience in the World's best research institutions such as MPI and MIT, and attended many conferences. And again because of her efforts in boosting my career I will have my PhD education in Northwestern University. As I am leaving for my PhD education to US, I want to thank her for her endless support and do not making me regret any moment of my master's studies at SU.

As being my co-advisor, I gratefully acknowledge Dr. Ayşe Turak from MPI-MF for coming up with the initial idea of this thesis. Dr. Turak was always supportive and open to new ideas throughout our studies. Not only with the great knowledge on organic devices but also helping with the device fabrication and ANKA XRD experiments, her contribution to this project was very crucial. Moreover, by inviting me to MPI she introduced me to new experiences and new people. Experiments performed at MPI along with the access of many types of equipment were milestones of this thesis.

Special thanks go to Dr. Beri N. Mbenkum from MPI-MF for her guidance on micelle technique and coming to SU for my thesis defense. Her knowledge and tricks on the issue as well as her assistance with characterization in the early stage helped me to obtain results faster and better. In addition, her support and friendship during my MPI visit gave me a lot of strength to do research.

I would like to thank Prof. Mehmet Ali Gülgün for his endless support with electron microscope and fruitful discussion for the progress of the project. He always made us love

in with Materials Science with the classes he thought. By enlarging our vision he showed us what we are capable of doing.

I would also like to thank Prof. Levent Demirel for being my thesis jury member and giving me important advices. His critical comments in our manuscripts were very helpful to construct a more mature article.

Many thanks go to people at MPI-MF, starting with my officemates, Felix Maye for his help in lab and with equipments in general, Minh Nguyen and Deniz Ergün for their help with charging experiments. I would like to acknowledge Dr. Alina Vlad for helping with ANKA experiments, Dr. Udo Welzel for helping XRD characterization, M. Weiland and L. P. H. Jeurgens for helping XPS measurements and Esra Burcu Yarar for helping adhesive tape experiments. I also would like to acknowledge Prof. Joachim Spatz for the access of SEM, plasma system and spin coater and Ioanis Grigoridis for orientation of the devices.

I want to thank to Dr. Iain Baikie and Dr. Grzegory Halek of KP Technology, Scotland, for kelvin probe work function measurements. Their contribution to this porject was very critical for understanding particle properties. I want to acknowledge Dr. S. Strun and Dr. M. Ceh from Jozef Stefan Institute for the access to TEM.

I am grateful to Murat Eskin for his help with furnaces and charging experiments, Selman Erkal for his great efforts and discussions to nanotransfer printing and Mahmut Tosun for the discussions about adhesive tapes. In addition, I appreciate the help of Ani Kamer from Stanfor University for transfer experiments.

I convey special acknowledgement to Prof. Yusuf Menceloğlu for the great discussions at several points of the research, and Prof. Alpay Taralp for the important assistance for chemistry parts in the micellar reactor project. I also want to thank other professors in our department, Prof. Canan Atılgan, Prof. Yuda Yürüm, Prof. Burç Mısırlıoğlu Prof. Melih Papila, Prof. Mehmet Yıldız, Prof. Selmiye Alkan, who thought me in classes and made me enjoy learning along with my other professors what I know as a materials scientist today.

I am grateful to the previous members of Ow-Yang group, Osman El-Atwani and Ömer Faruk Mutaf for their significant contributions to micellar reactor and AFM work. I especially want to thank Ömer Faruk Mutaf for his great friendship and support that with

patience we together prepared two publications. In addition, I want to thank to Alim Solmaz for his excellent work with AFM nanoindentation and introducing the technique to SU community. Moreover, I want to thank to previous and current group member Hasan Kurt for the photoluminescence measurements.

Again from MPI- MF I acknowledge the help of Dr. Vesna Srot and Dr. Peter van Aken in micellar reactor study. In addition I want to acknowledge Dr. Julia Deuschle for her help with nanoindentation studies and Mrs. Claudia Sussdorff for her kind helps for my MPI travels. I also acknowledge Omer Faruk Deniz from GYTE for aid in TEM measurements.

From Istanbul Technical University, I want to thank to Prof. Metin Acar and Dr. Şebnem İnceoğlu for introducing me the interesting field of baroplastics. Their challenging but at the same time amazingly ordered samples cause me to learn more AFM and polymer.

From MIT, I would like to acknowledge Prof. Francesco Stellacci for allowing me to be in his group and giving me the taste of their research environment, and Dr. Javier Gomez Reguerra for teaching me particle purification methods and particle synthesis with multiple ligands.

I also would like to acknowledge Prof. Yaşar Gürbüz, Bülent Koroğlu and Saravan Kallempudi for clean room access and plasma trials, Burçin Yıldız for NMR measurements in other projects, and Sibel Pürçüklü for material and chemical purchases.

I am greatly indebted to my senior colleagues, Dr. Çınar Öncel, Özge Malay and İbrahim İnanç for teaching me most of the equipments and laboratory techniques during my undergraduate education.

There are several SU members who indirectly contributed this work in several ways. I am grateful to Dean Prof. Albert Erkip, Zehra Öner, Zuhale Bakkal and Figen Şahin from Dean's Office, Mehmet Manyas, Asuman Akyüz and Hilmi Çelik from Information Center, people in Research and Graduate Policy, people in Project Management Office.

It is a pleasure to pay tribute to my dear friend Ahmet Tüysüzoğlu who hosted me during my Boston visits. Ahmet's support and motivation always made me ambitious and willing in my studies for my future career.

I warmly thank my colleagues in SU, Salih Yiğit, Özlem Kocabaş, Cem Burak Kılıç, Sinem Taş, Firuze Okyay, Gökay Toprak, Elif Özden, Mehmet Çelik, Burcu Özel, Ferhat Şen, Burcu Saner, Selime Shawuti, Melike Mercan Yıldızhan, Erim Ülkümen, Yeliz Ekinci, Mustafa Baysal, Ayça Abakay and Kaan Bilge for building a pleasant research environment and helping me to focus with their small coffee and tea breaks.

I would like to thank to my parents, my brother, my sister and my little nephews and niece for their love and endless support. Feeling their presence even from long distances always made me relaxed.

A. Turak acknowledges funding from Marie Curie International Incoming Fellowship within the 7th European Community Framework Programme.

I acknowledge Institute for Complex Adaptive Matter, ICAM/I2CAM, for reimbursing my travels to Boston 3 times, without their financial aid it would not have been possible to attend the conferences and visit MIT.

Finally, I am grateful to TUBITAK BİDEB 2210 Master's Scholarship Program for their generous scholarship throughout my Master's studies.

Table of Contents

Contents

CHAPTER 1. INTRODUCTION	- 20 -
1.1 Nanoparticle Synthesis via Diblock Copolymer Micelles	- 20 -
1.2 Effect of LiF on Photovoltaic Devices	- 25 -
1.3 Nanotransfer Printing	- 32 -
1.4 Aim of the Thesis	- 49 -
Chapter 1 References	- 50 -
CHAPTER 2. EXPERIMENTAL	- 57 -
2.1 Materials	- 57 -
2.2 Lithium Fluoride Formation	- 57 -
2.2.1 Lithium Fluoride Synthesis in Toluene	- 57 -
2.2.2 Lithium Fluoride Nanoparticle Synthesis in Polystyrene block poly(2-vinyl pyridine) copolymers (Plan A and Plan B reactions)	- 58 -
2.2.3 Understanding aging effect	- 59 -
2.3 Post Processing After Synthesis	- 59 -
2.3.1 Coating on substrates	- 59 -
2.3.2 Plasma Etching	- 60 -
2.4 Device Formation in Inverted Structure With Direct Coating of Nanoparticles	- 60 -
2.5 Effect of Direct Coating of Particles on Organic Surfaces	- 61 -
2.6 Nanotransfer printing Experiments	- 62 -
2.6.1 PDMS Curing	- 62 -
2.6.2 PDMS Pressing	- 64 -
2.6.3 PMMA Cooling	- 65 -
2.6.4 Electrostatic Charging of PMMA	- 65 -
2.6.5 Adhesive Tape Experiments	- 66 -
2.7 Characterization	- 66 -
2.7.1 Dynamic Light Scattering (DLS)	- 66 -
2.7.2 Scanning electron microscope (SEM)	- 67 -
2.7.3 Atomic force microscope (AFM)	- 67 -
2.7.4 Transmission electron microscope (TEM)	- 67 -
2.7.5 X-ray photoelectron spectroscopy (XPS)	- 68 -

2.7.6	X-ray diffraction (XRD).....	- 68 -
2.7.7	Kelvin probe work function measurements	- 68 -
	Chapter 2 References.....	- 69 -
	CHAPTER 3. RESULTS AND DISCUSSION	- 70 -
3.1	Lithium Fluoride Formation.....	- 70 -
3.1.1	Lithium Fluoride Synthesis in Toluene	- 70 -
3.1.2	Lithium Fluoride Nanoparticle Synthesis in Polystyrene block poly(2-vinyl pyridine) copolymers	- 71 -
3.2	Work Function Measurements	- 83 -
3.3	Fabrication of Inverted Device	- 91 -
3.4	Effect of Direct Coating Conditions on Organic Surfaces	- 94 -
3.5	Nanotransfer Printing Experiments.....	- 99 -
3.5.1	PDMS Results	- 99 -
3.5.2	PMMA Results.....	- 111 -
3.5.3	Electrostatic Charging Results.....	- 114 -
3.5.4	Adhesive Tape Experiments	- 116 -
	Chapter 3 References.....	- 121 -
	CHAPTER 4. CONCLUSION	- 124 -

Abbreviations and Symbols

AFM	: Atomic force microscope
Al	: Aluminum
Alq₃	: Tris(8-hydroxyquinoline)
C₆₀	: Buck-minsterfullerene
CdS	: Cadmium sulfate
CdSe	: Cadmium selenide
E_F	: Fermi energy
FTIR	: Fourier transform infrared spectroscopy
GaAs	: Gallium arsenide
HF	: Hydrofluoric acid
HOMO	: Highest occupied molecular orbital
HRTEM	: High resolution transmission electron microscope
ITO	: Indium tin oxide
KP	: Kelvin probe
LiAc	: Lithium acetate
LiF	: Lithium fluoride
LiOH	: Lithium hydroxide
LUMO	: Lowest unoccupied molecular orbital
M	: Micelle
MEH-PPV	: Poly(2-methoxy,5-(2'-ethyl-hexyloxy)-p-phenylene vinylene)
MgO	: Magnesium oxide
NH₄F	: Ammonium fluoride
NIL	: Nanoimprint lithography
nTP	: Nanotransfer printing
OLED	: Organic light emitting diode
OPV	: Organic photovoltaic
P2VP	: Poly(2-vinylpyridine)
P4VP	: Poly(2-vinylpyridine)
PDMS	: Poly(dimethylsiloxane)
PEDOT:PSS	: Poly(3,4- ethylenedioxythiophene):poly(styrene sulfonate)
PFO	: Poly(9,9-dioctyl-fluorene)
PMAA	: Polymethacrylic acid
PMMA	: Poly (methyl methacrylate)
PS	: Polystyrene
PS-b-P2VP	: Polystyrene block poly(2-vinylpyridine)
QE_{PL}	: Photoluminescence quantum efficiency
SAM	: Self assembling monolayer
SEM	: Scanning electron microscope
Si	: Silicon
TEM	: Transmission electron microscope
T_g	: Glass transition temperature
TMA-OH	: Tetramethyl ammonium hydroxide
XRD	: X-ray diffraction
ZnO	: Zinc oxide
Φ	: Work function
γ	: Surface energy

List of Figures

Figure 1. 1: Schematic illustration of ZnO nanoparticle synthesis in two step reaction inside PS- <i>b</i> -P2VP reverse diblock copolymer micelle.....	- 24 -
Figure 1. 3: Schematic illustration of an organic photovoltaic device	- 26 -
Figure 1. 4: Schematic illustration of energy levels (a) in an OLED and (b) an OPV	- 27 -
Figure 1. 5: Brightness decay under continuous operation at constant current at 85 °C for devices with a LiF/Al and BaF ₂ /Al cathode (taken from Ref 30 without permission) ...	- 29 -
Figure 1. 6: Schematic illustration of nanoimprint lithography (NIL) (a) and schematic illustration of the formation of topographically patterned molds (or stamps, depending on the application) and replication	- 33 -
Figure 1. 7: Schematic diagram of the processes involved in embossing titania: (a) preparing AAO template, (b) infiltrating PMMA, (c) coating on PDMS (d) retrieving mold by wet chemical etching, (e) embossing sol-gel TiO ₂ and (f) removing the mold (taken from Ref 58 without permission)	- 34 -
Figure 1. 8: SEM images of (a) typical initial AAO template, (b) typical embossed TiO ₂ structures after PMMA removal with acetonitrile (c) embossed TiO ₂ structures (d) smaller-diameter pores with one showing 20 nm diameter, and (e) embossed TiO ₂ at a larger scale showing uniformity of the replication. (taken from Ref 58 without permission).....	- 35 -
Figure 1. 9: (a) Schematic illustration of steps for noncovalent transfer printing. Contacting a metal coated stamp to a substrate, followed by moderate heating causes the metal to remain on the substrate after removing the stamp. (b) Optical micrograph of arrays of Au (30 nm thick) dots printed over an area of 0.5 cm× 0.5 cm on a plastic substrate. (c) SEM micrograph of a small region of the printed pattern. (d) Optical micrograph of various Ti(2nm)/Au(30 nm) device patterns printed onto a SiO ₂ /Si substrate. (e) Optical and SEM micrographs of a small region of the printed pattern. (Taken from Ref 59 without permission)	- 37 -
Figure 1. 10: Schematic illustration of the generic process flow for the transfer printing solid objects. The process begins with the preparation of an assemblage of microstructures on a donor substrate by solution casting, micromachining, self-assembly or other suitable means. (i) Laminating a stamp against a donor substrate and then quickly peeling it away (ii) pulls the microstructures from the donor substrate onto the stamp. Contacting the stamp to another substrate (receiving substrate (iii)) and then slowly peeling it away transfers the microstructures from the stamp to the receiver (iv). The peeling rate determines the strength of adhesion and, therefore, the direction of the transfer. (Taken from Ref 60 without permission).....	- 39 -
Figure 1. 11: Images of transfer printed objects with sheet-like and globular geometries. a, 100-nm-thick mica ribbons cleaved from a mica substrate with a PDMS stamp, and then transfer-printed onto SiO ₂ (blue). b, Graphite sheet, ranging from 3 to 12 nm thick, cleaved from a highly ordered pyrolytic graphite substrate and printed onto SiO ₂ with a stamp. c,d, Silica microspheres (c) and African Violet pollen grains (d) picked up from and subsequently printed onto silicon wafers by means of PDMS stamps. Relief features in the stamp define the stripe pattern in c. (Taken from Ref 60 without permission).....	- 40 -

Figure 1. 12: Schematic illustration of nanotransfer printing (nTP) on GaAs: (a) native oxide is removed from the wafer surface before 1,8-octanedithiol molecules are deposited; (b) a gold-coated (20 nm) elastomeric stamp is brought into contact with the treated surface; and (c) the stamp is removed to complete the printing. (Taken from Ref 62 without permission) - 41 -

Figure 1. 13: a-c) Schematic representation of the processes to fabricate patterns of nanoparticles using chemical templates in combination with (a) or without physical barriers (b). The polymer templates were prepared by nanoimprint lithography, SAMs were formed by gas phase deposition, and nanoparticles were attached using a vertical deposition set-up (c), in which the samples were withdrawn vertically from the nanoparticle suspension. (Taken from Ref 65 without permission)..... - 42 -

Figure 1. 14: SEM images of 55 nm carboxylate-functionalized SiO₂ nanoparticles assembled on PMMA-imprinted sub-300 nm patterns with aminoalkyl SAMs. The initial polymer height was 100 nm, and the residual layer was removed by exposure to O₂ plasma for 10 s. The withdrawal speed was 1 μm s⁻¹. After particle adsorption, the polymer template was removed by sonication in acetone for 1 min. The effect of confinement on the particle assembly is apparent by using lines with linewidths of a) 100 nm and b) 60 nm, and holes with diameters of c) 180 nm and d) 100 nm. (Taken from Ref 65 without permission) - 43 -

Figure 1. 15: Typical reaction conditions for catalytic stamp lithography (1 min inking and 20 min stamping) and the concept of localized catalysis. Catalytic hydrosilylation takes place only underneath Pd nanoparticles. (Taken from Ref 66 without permission) - 44 -

Figure 1. 16: (a) AFM height image of a parent Pd catalytic stamp with nanoparticle diameters of 40 nm and a center-to-center spacing of 110 nm. (b) 1-Octadecyne-stamped Si(111)-H surface and corresponding phase image (c). (d) Section analysis along the dashed line in (b). (e) AFM height image of a 1-octadecyne-stamped Si(111)-H surface, followed by wet chemical etching with 40% NH₄F (aq). (f) SEM image of the sample from (e). (Taken from Ref 66 without permission)..... - 45 -

Figure 1. 17: Scheme 1) gold nanoparticle preparation and supramolecular nanostamping cycle, (a) AFM height image of Au nanoparticle master (b) AFM height image of printed pattern (Taken from Ref 67 without permission) - 46 -

Figure 1. 18: (LEFT) Principle of electrical micro contact printing. (A) The flexible, metal-coated stamp is placed on top of a thin film of PMMA supported on a doped, electrically conducting silicon wafer. (B) An external voltage was applied between the Au and the silicon to write pattern of the stamp into the electret. (C) The stamp was removed; the PMMA was left with a patterned electrostatic potential. (RIGHT) Optical microscope and SEM images of different types of particles trapped at patterned charge and transferred onto second substrates. (A) 50-μm-wide parallel lines of toner particles, <20 μm in size; (B) 5-μm-wide parallel lines of iron beads, <2 μm in size; (C) 2.5 and 10- μm-wide lines of red iron oxide particles, <500 nm in size. (Taken from Ref 68 without permission)..... - 48 -

Figure 2. 1: Chemical structure of PS-b-P2VP copolymers - 57 -

Figure 2. 2: Shrinkage graph of Sylgard 184 PDMS depending on the curing temperature (Taken from Ref 1 without permission) - 64 -

Figure 2. 3: Press set-up used for PDMS pressing and other purposes.....	65 -
Figure 3. 1: (a) SEM image and (b) XPS spectra of LiF crystals produced from direct reaction of LiOH and HF in toluene.....	71 -
Figure 3. 2: SEM image of PS-P2VP micelles loaded with LiOH and etched with O ₂ plasma.....	72 -
Figure 3. 3: Dynamic light scattering result for empty and LiOH loaded micelles, average size increased from 16.7 nm to 67 nm upon loading of LiOH.	73 -
Figure 3. 4: LiOH and HF loaded micelles etched with (a) O ₂ plasma and (b)H ₂ plasma-	74 -
Figure 3. 5: SEM images of LiOH and HF loaded micelles after 3 days of HF addition (a) and after 15 days of HF addition (b).....	75 -
Figure 3. 6: SEM image of LiOH and HF loaded micelles etched with O ₂ plasma after 3 days of HF addition	76 -
Figure 3. 7: SEM image of LiOH and HF loaded micelles, spin coated on Si ₃ N ₄ substrate and etched with O ₂ plasma after 15 hours of HF addition. FFT is given on the upper right corner.....	76 -
Figure 3. 8: SEM images of only HF loaded micelles coated and etched after 3 days (a) and 15 hours stirring (b)	77 -
Figure 3. 9: FTIR spectra of 4 samples, PS film, PS+HF(1%), PS+HF(5%) and PS+HF(40%)	78 -
Figure 3. 10: SEM image of M+LiAc+NH ₄ F on silicon substrate after O ₂ plasma etching ...	80 -
Figure 3. 11: SEM image of M+LiOH+HF prepared in glass vial and spin coated on silicon substrate, after etched with O ₂ plasma	80 -
Figure 3. 12: (a) Electron diffraction (Cleva Ow-Yang) and (b) background subtracted x-ray diffraction pattern formed from LiF-loaded polymeric micelles (Udo Welzel).....	82 -
Figure 3. 13: TEM micrograph of LiF nanoparticles on Si ₃ N ₄ grid. Likely particles are highlighted, showing both crystalline and amorphous particles. Line profiles through the background and some particles are highlighted by the blue lines	82 -
Figure 3. 14: Grazing incidence x-ray diffraction spectra of LiF nanoparticles coated on MgO substrate (Ayşe Turak)	83 -
Figure 3. 15: ITO surface – (a) as received ITO (b) ITO surface after O ₂ plasma (MPI6) (non-contact AFM). RMS roughness = 0.6nm and 0.94nm respectively (Ayşe Turak) .-	84 -
Figure 3. 16: Schematic illustration of monolayer of micelle spin coated on ITO before (a) and after (b) O ₂ plasma etching. SEM images of (c) a single layer of micelle-assisted solution-processed LiF, after etching with O ₂ plasma; and (d) three layers of solution-processed LiF, formed by successive spin coating and O ₂ plasma etching.....	85 -
Figure 3. 17: (a) MPI3: 10Å LiF thermally evaporated on ITO (b) masked region of MPI3 showing the ITO surface. (non-contact AFM) (c) Overlay of stereographic projection for LiF with indication of the 100 and 111 poles and the measured pole figures for the 111 (left) and 200 (right) reflections of thermally evaporated LiF (Ayşe Turak).....	85 -
Figure 3. 18: Thermally evaporated LiF (5Å by QCM) on diindenoperylene (5ML) (non-contact AFM) (b) corresponding height profile (Felix Maye)	86 -

Figure 3. 19: Surface work function map (scanning Kelvin probe) of the electrode bilayer consisting of solution-processed LiF on ITO. The scan area was over $11.2 \times 10 \text{ mm}^2$ with tip radius 2mm. The scans were performed, while maintaining a constant tip-to-sample spacing, in order to facilitate comparison of different samples to the tip. - 87 -

Figure 3. 20: Schematic illustration of experimental procedure for fabrication of inverted device with LiF nanoparticles produced with PS-b-P2VP copolymer reverse micelles. - 92 -

Figure 3. 21: M+LiOH+HF solution that is used on Al substrate, spin coated on glass at 2000 rpm and etched with O_2 plasma with 150 W, 0.1 mbar for 45 minutes. - 93 -

Figure 3. 22: I-V curves for the devices produced from only thermal evaporated LiF films. Unmasked (O776) (a) and masked (O779) devices (b). - 94 -

Figure 3. 23: I-V curves for the devices produced from solution based LiF nanoparticles. Unmasked (O777) (a) and masked (O778) devices (b). - 94 -

Figure 3. 24: AFM images of (from left to right) initial surface- after toluene exposure- after H_2 etching of CHB 204B (a), CHB 203B (b), CHB 202B (c), O665 (d), O643 (e), O571 (f), O 559 (g). - 97 -

Figure 3. 25: SEM of DIP surface initially coated with LiOH and HF loaded micelles and etched with H_2 plasma - 98 -

Figure 3. 26: Schematic illustration for direct printing and SEM result for P3HT-PCBM film upon heating. - 99 -

Figure 3. 27: AFM images of (from left to right) initial surface- after PDMS pressing of CHB204B (a), CHB 203B (b), CHB 202B (c), O665 (d), O643 (e), O571 (f), O 559 (g). - 104 -

Figure 3. 28: AFM image of micelles (3mg/ml) loaded with LiOH, and after HF addition, spin coated (2000 rpm) on normal (100) silicon substrate, before etching (a), on ITO after etching with O_2 plasma (b) and corresponding height profile (c) - 105 -

Figure 3. 29: AFM image of micelles (3mg/ml) loaded with LiOH, and after HF addition, spin coated (2000 rpm) on ITO substrate (a), afterwards etched with O_2 plasma (150 W, 0.1 mbar, 1 hour), after PDMS pressing; and corresponding profiles (b)-(c) - 106 -

Figure 3. 30: AFM image of micelles (3mg/ml) loaded with LiOH, and after HF addition, spin coated (2000 rpm) on H-terminated silicon substrate (a), afterwards etched with O_2 plasma (150 W, 0.1 mbar, 1 hour), after PDMS pressing; and corresponding profiles (b)-(c) - 106 -

Figure 3. 31: AFM image of micelles (3mg/ml) loaded with LiOH, and after HF addition, spin coated (2000 rpm) on normal (100) silicon substrate (a), afterwards etched with O_2 plasma (150 W, 0.1 mbar, 1 hour), BEFORE PDMS pressing; and corresponding profiles (b)-(c). - 106 -

Figure 3. 32: AFM image of micelles (3mg/ml) loaded with LiOH, and after HF addition, spin coated (2000 rpm) on normal (100) silicon substrate (a), afterwards etched with O_2 plasma (150 W, 0.1 mbar, 1 hour), AFTER PDMS pressing; and corresponding profiles (b)-(c). - 107 -

Figure 3. 33: SEM image of silicon surface of NTP11 experiment - 107 -

Figure 3. 34: Electron micrographs of Au nanoparticles on borosilicate glass and SiO_x/Si substrates: (a) SEM image showing a tilted view (45°) of Au nanoparticles on a borosilicate glass. HRTEM images of Au nanoparticles on SiO_x/Si (b,d) and glass (c)

substrates after a H₂ plasma burning process. (b) Zoom-in image of a Au nanoparticle with a diameter of about 9 nm. The particle is partly embedded in an amorphous SiO_x layer. (c) Au nanoparticles partially embedded in a topographically rough glass substrate as compared to the relatively flat SiO_xSi substrate shown in panel d. (Taken from Ref 21 without permission)- 110 -

Figure 3. 35: Schematic illustration of heating/cooling experiments with PMMA.....- 112 -

Figure 3. 36: SEM image of PMMA surface after heating-cooling experiment.- 113 -

Figure 3. 37: Schematic illustration of PMMA charging experiments.....- 114 -

Figure 3. 38: SEM results of charging experiments. Both PMMA and glass surfaces are shown after experiment.- 115 -

Figure 3. 39: Schematic illustration of direct charging experiment- 115 -

Figure 3. 40: Schematic illustration of a Scotch adhesive tape experiment.....- 117 -

Figure 3. 41: SEM of LiF nanoparticle-coated-glass surface after transfer experiment- 117 -

-

Figure 3. 42: SEM of adhesive tape surface after transfer experiment- 118 -

Figure 3. 43: Schematic illustration of transfer printing experiment that will be carried out by REVALPHA thermal release tape.....- 119 -

Figure 3. 44: AFM images of glass substrate coated with LiF particles (x3), before (left) and after (right) peeling.- 120 -

List of Tables

Table 1. 1: External QE and operating voltage of BaF ₂ /Al devices are presented (taken from Ref 30 without permission)	- 28 -
Table 1. 2: EQ _{PL} of different structure devices based on MEH-PPV is presented (taken from Ref 30 without permission)	- 29 -
Table 3. 1: Summary of extracted work function (Φ) from KP using a 2mm calibrated polycrystalline Au tip (calibrated to Au surface with $\Phi = 5.1\text{eV}$).	- 88 -
Table 3. 2: List of organic layers that were analyzed	- 95 -
Table 3. 3: List of substrates on which PDMS curing was tried	- 100 -
Table 3. 4: Surface energies of common substrates and surfaces.	- 102 -
Table 3. 5: Summary of most nano transfer printing experiments	- 109 -
Table 3. 6: Summary of experiment for weakening particle-substrate interaction	- 111 -
Table 3. 7: Summary of PMMA cooling/heating experiments	- 113 -
Table 3. 8: Summary of charging experiments.....	- 116 -

CHAPTER 1. INTRODUCTION

In 1959 Richard Feynman said “There is a plenty of room at the bottom... What I want to talk about is the problem of manipulating and controlling things on a small scale”. It is impressive that Feynman was aware of research opportunities at the nanoscale about five decades ago, and his vision was an inspiration for the rapidly growing research on nanotechnology. In fact, in that statement, he illuminated the key challenge that we face today, that of manipulation of the nano-objects into a useful form, as an enabling layer in a device. The primary objective of this thesis is the manipulation of nanoparticles to enhance the performance of electrode bilayers in photonic devices.

1.1 Nanoparticle Synthesis via Diblock Copolymer Micelles

In the last two decades, interest in the synthesis and properties of colloidal nanoparticles has grown, due to their potential catalytic, optical and electrical applications, which stem from the confinement-induced quantization of most electronic properties^{1,2,3}. Particles at the nanoscale can be produced by “top-down” and “bottom-up” approaches. Top down approach uses various types of lithography to make nanoscale patterns. The mostly used techniques are “bottom-up,” which involve wet chemistry procedures.

The formation of nanoparticles by wet chemical procedures requires the optimization of nucleation and growth. To obtain monodisperse particles, the nucleation time should be distinctly separate from the growth regime. If they overlap, different nucleation sites will evolve with different growth durations, which results in a broader size distribution. Apart from nucleation and growth, in order to synthesize high quality nanoparticles, passivation of a surface is required. Metal or semiconductor clusters will have high surface activity in the nanoscale regime, and therefore they should be stabilized by surface-capping ligands, which will enable engineering the interactions between nanoparticles⁴. Among the many different types of ligands, diblock copolymer micelles were employed as reactor vessels for nanoparticle synthesis in this study.

In the last decade, intense research has been done on synthesis of metallic and semiconducting nanoparticles by use of amphiphilic diblock copolymer (reverse) micelles because these systems enable high degree of monodispersity and directed assembly of 2-dimensional periodic arrays^{5,6,7,8}. In polymeric micelles, the functionality of the nanoreactor stems from the selectively soluble nature of one block and the metal coordination capability of the other block. The final stable structure of diblock copolymer micelle is based on its molecular weight and the polarity difference between the two blocks and hence the size of the nanoreactor can be adjusted by changing the overall and relative block lengths^{9,10,11}. Synthesis in the micelle can be limited by the amount of precipitated material that could be accommodated inside the micelle, which thus enables better control over the size distribution. In addition, with the only criteria being for a reactant to coordinate with the core block of micelle, the micelle technique is applicable to the synthesis of a broad range of nanoparticle systems. Metal nanoparticles such as gold, silver, platinum, Co-Fe core-shell structures, as well as semiconducting nanoparticles, such as cadmium sulfate (CdS), cadmium selenide (CdSe), and zinc oxide (ZnO) have been demonstrated by the use of diblock copolymer micelles^{6,12,13,14}.

Until now, different diblock copolymers have been used in nanoparticle synthesis and most of them have a common shell, which is polystyrene (PS). The core region of diblock copolymer micelles must like metals and in most cases coordinate with them. To fulfill such a requirement, different inner metal-binding blocks have been used such as poly(4-vinylpyridine) (P4VP), poly(2-vinylpyridine) (P2VP), polyethyleneoxide (PEO), polybutadiene (PB) and polymethacrylic acid (PMAA)^{11,15}. In their diblock form with PS, those polymers can form reverse micelles in a selective solvent such as toluene, which dissolves the PS block but not other block, such as P2VP, due to their relatively polar nature. In addition, using an organic solvent suitable for reverse micellization has another advantage, which is the segregation of polar metal salts to the core of the reverse micelles. In the core of the micelle, metal cations are held by forming a bond with the polar blocks¹¹. Among the commercially available diblock copolymers, mostly PS-*b*-P2VP and PS-*b*-P4VP were used because the strong interaction of the inner block with metal cations and the stabilizing effect of the outer block. The difference between PS-*b*-P2VP and PS-*b*-P4VP is the nature of micelle formation. Because P4VP has a more polar character than P2VP, PS-*b*-P4VP can form stable micelles themselves and form stronger bonds with metal cations, while PS-*b*-P2VP exhibits metal induced micellization, especially for

symmetric blocks (blocks which have the same molecular weight) and blocks with the lower molecular weight PS¹⁶.

After nanoparticle synthesis, post processing is required in order to remove the polymeric micelles from the nanoparticles. A commonly used technique for removing polymeric micelles is plasma etching with O₂, H₂, and N₂^{11,16,74}. The importance of removing micelles with a plasma cleaner is to preserve the 2-D arrangement and enable the production of one nanoparticle per micelle, despite the strong tendency for the formation of several nanocrystals per micelle. M. Aizawa and J. M. Buriak produced metal nanoparticles arranged in an ordered 2-D layer by the use of diblock copolymer micelles and observed the removal of particles along with the micelles by ultrasonication in a toluene bath. Hence they resorted to the use of plasma cleaning for removal of micelles¹⁷. This finding is significant for device application, because any change in the arrangement of nanoparticles will influence new patterns that will subsequently be formed on top of the nanoparticle layer. M. Haupt and coworkers prepared 2-D arranged gold nanoparticles with diblock copolymer micelles and coated a monolayer of them on a gallium arsenide (GaAs) substrate. After cleaning the polymeric part with plasma etching, they applied an anisotropic etching on the hexagonal pattern and created a well-defined quantum well between each nanoparticle¹⁸. In a similar study, C. Lee and colleagues used PS-*b*-P4VP for the synthesis of an ordered layer of cobalt (Co) nanoparticles, which will act as a charge storing layer for a charge trap flash memory device¹⁹. To keep the 2-D arrangement unaltered, plasma etching was used for removal of PS-*b*-P4VP around Co nanoparticles. Furthermore, plasma etching can be used to reduce nanoparticles simultaneously^{74,75}. Rather than using a reducing agent such as hydrazine, Mbenkum et al. showed that H₂ plasma or O₂ plasma can be employed to reduce Au nanoparticles and remove the polymeric micelles at the same time⁷⁴. Similarly, core-shell nanoparticles can be synthesized with micelles by loading the desired metallic salts (such as FeCo) together and then reducing them with plasma etching⁷⁵. For such system, reducing with plasma etching also directs the homogeneous coalescence of different metallic salts into one core-shell nanoparticle per micelle.

For some cases, in addition to cleaning the polymeric part, plasma etching was also used for reducing nanoparticles or creating diatomic semiconductor nanoparticles. As an example, synthesis of ZnO nanoparticles by micellar route was achieved by oxidation of

ZnCl₂ nanoclusters which were previously loaded to PS-*b*-P2VP diblock copolymer micelle²⁰. Here, O₂ plasma processing was used both to remove polymeric part and to oxidize Zn particles to form ZnO nanoparticles. In fact, a similar secondary gas phase-reaction was also used to form CdS and PbS nanoparticles **Hata! Başvuru kaynağı bulunamadı.** However, in these methods diblock copolymer micelles were not used as true nanoreactor vessels. To be able to employ diblock copolymer micelles as true nanoreactor vessels El-Atwani et al. recently reported two step reaction inside micelle for ZnO nanoparticle synthesis¹⁴. In this study, initially zinc acetate (ZnAc) was loaded inside micelles and loading was proved with Fourier transform infrared spectroscopy (FTIR), which displayed a small shift in characteristic C-N bond in pyridine unit. This shift had resulted from coordination of Zn⁺ with pyridine unit. After successful loading of the metal salt, tetramethyl ammonium hydroxide (TMA-OH) was used as second reactant and oxygen source. Then the following reaction lead to ZnO nanoparticle formation inside micelle without any post treatment:



All the process is illustrated in Figure 1. 1. This study enabled realization of two step reaction inside polymeric micelles and made the micelle technique to be applicable wider variety of diatomic nanoparticle synthesis.

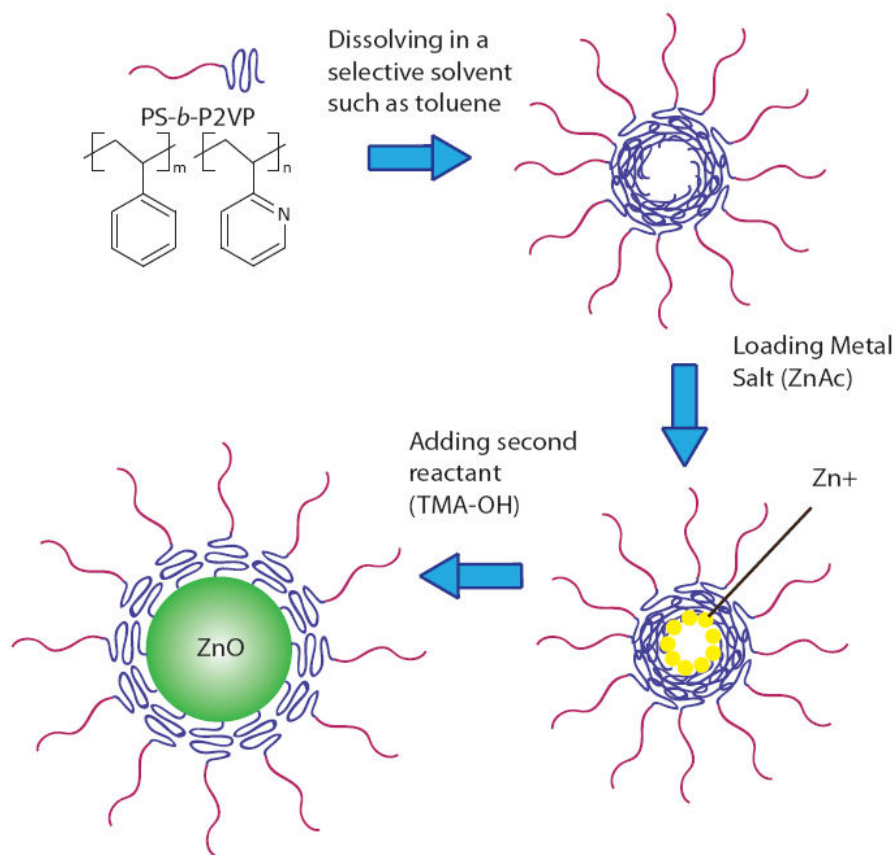


Figure 1. 1: Schematic illustration of ZnO nanoparticle synthesis in two step reaction inside PS-*b*-P2VP reverse diblock copolymer micelle

As discussed in this section of the thesis, the nanoparticle synthesis by use of diblock copolymer micelles can be outlined as following:

- a) Formation of micelle by dissolving diblock copolymer in a selective organic solvent
- b) Adding metal salt to micelle solution in which metal salts will precipitate inside micelles and coordinate to polar block
- c) Adding the reducing agent (for metal nanoparticles) or second reactant (for diatomic molecules and semiconductors) to make reaction that will yield nanoparticles
- d) Post processing to remove polymeric micelles around nanoparticles, preferably by plasma etching techniques.

Since the chemical variability is one of the most significant advantages of the micellar route in nanoparticle synthesis, the synthesis of lithium fluoride (LiF) nanoparticles, for the

first time, was demonstrated by use of diblock copolymer micelles in this thesis study. Following the ZnO nanoparticle synthesis, a two step reaction inside micelle was planned for LiF nanoparticle formation.

1.2 Effect of LiF on Photovoltaic Devices

In the last decade the understanding of polymer-based photovoltaic devices has increased significantly, due to the heightened research activity in the field. This serious effort has paid off, enabling devices with power conversion efficiencies as high as $\sim 6.7\%$ ²². Although this is still below the 10% efficiency required for mass production and commercialization, having advantages such as stability over a lifetime of 10^4 hours, low-cost and relative processability render them more compelling in comparison to their inorganic competitors and pushes continuing intense research on organic photovoltaic devices²³. With the further improvements, it is expected that this devices will enter markets soon. A typical polymer based photovoltaic device is given in Figure 1. 2. The most important part of the organic photovoltaic device is its active region. This part can be composed of an organic bilayer with an electron donating and electron accepting properties. Poly(2-methoxy,5-(2'-ethyl-hexyloxy)-p-phenylene vinylene) or MEH-PPV for a common donor layer and buckminster fullerene or C_{60} film for a common acceptor layer can be given as an example for the heterojunction. In order to increase the interfacial area, the same molecules have also been used in the form of a phase-separated, interpenetrating network (bulk heterojunction), as the active layer of photovoltaic device with a higher efficiency²⁴. Apart from the active region and electrodes, there are additional layers. These include an electron-injection (hole-blocking) layer, such as LiF, and hole-injection (electron-blocking) layer, such as poly(3,4-ethylenedioxythiophene):poly(styrene sulfonate) (PEDOT:PSS). These layers play a vital role in the charge-collection process and increase the efficiency of the device. Moreover, for the device to absorb the light efficiently, one of the electrodes (usually the anode) has to be transparent. In most cases, indium tin oxide (ITO) is used as transparent electrode in organic photovoltaic devices.

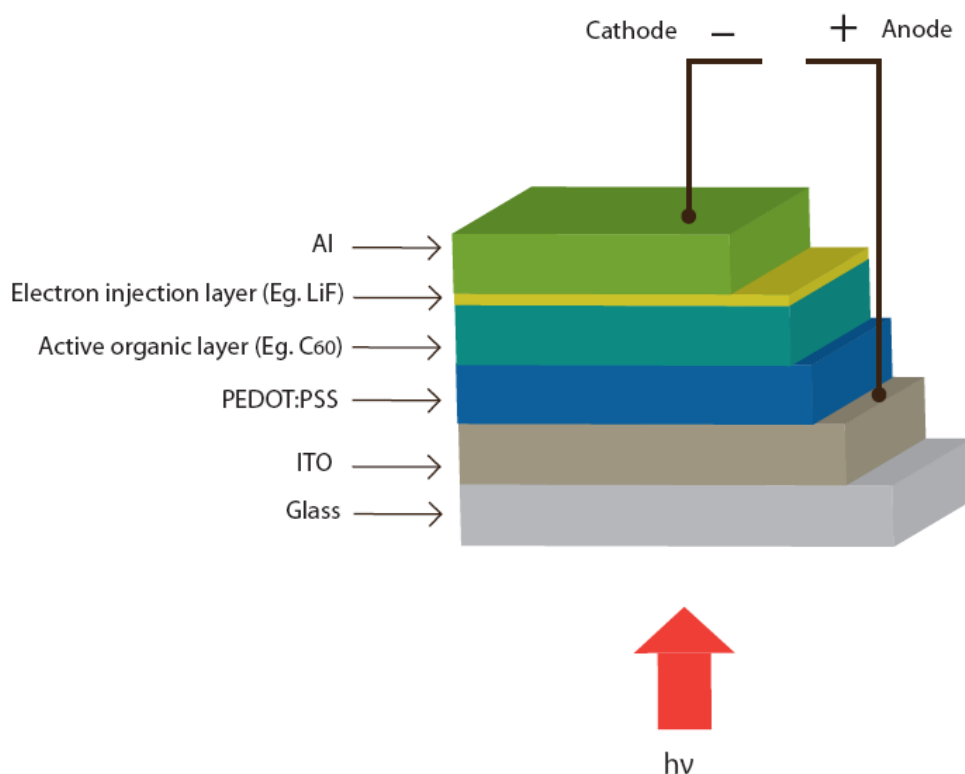


Figure 1. 2: Schematic illustration of an organic photovoltaic device

Although the details of different active layers used in organic photovoltaics is out of scope of this study, the device physics and interfacial phenomena are relevant for further discussion. When organic materials are used in a device application, either in organic light emitting diodes (OLEDs) or in organic photovoltaics (OPVs), the function of the device is very much dependent on the organic/metal interface. When organics are used for OLEDs, energy level alignment occurs at the interface and band bending occurs in thicker regions for OPVs²⁵. After alignment, energy levels in OLEDs and OPVs appear as shown in Figure 1. 3. In OLEDs, electron transfer from the low work function (high Fermi energy [E_F]) electrode to the organic electron transfer layer occurs with the assistance of an applied voltage. At the same time, hole transfer occurs from the high work function (low E_F) electrode to the organic hole transport layer. Then at the BHJ interface, electron-hole combination results in electroluminescence and the device emits light. On the other hand, almost reverse of this phenomenon happens in OPVs. With the absorption of light by the active organic layer, electron-hole pair forms. Holes are collected in higher work function electrode such as ITO and electrons are collected in lower work function electrode such as aluminum (Al).

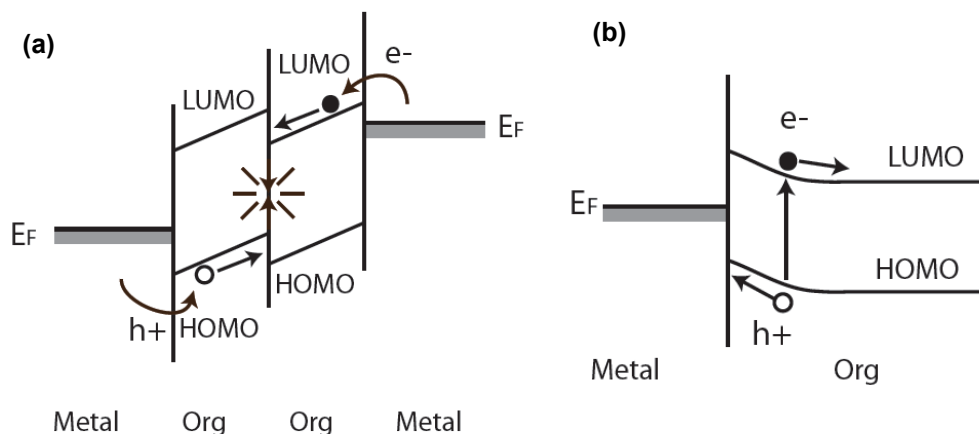


Figure 1. 3: Schematic illustration of energy levels (a) in an OLED and (b) an OPV

For OLEDs, efficient light emission can be achieved through reducing or eliminating energy barriers at organic/metal interface and balancing hole and electron injection²⁶. Among hole and electron, usually it is electron injection that is limited. To increase the electron injection, the barrier between the cathode such as Al and the organic layer such as tris(8-hydroxyquinoline) (Alq_3) need to be decreased. Using a relatively lower work function metal is also possible but such metals are readily oxidized and limit the lifetime of the devices. Rather than using a lower work function metal with comparison to Al, several groups have reported that the barrier height between Al and Alq_3 can be decreased by inserting a thin layer of LiF^{26,27,28}. Thin layer of LiF (usually below than 2 nm grown by thermal evaporation) decreases the energy barrier by resulting in band bending of Alq_3 towards Al²⁹. However, the real mechanism behind this barrier reduction is still under debate.

In order to explain the mechanism behind the improved electron injection with the presence of LiF, various theories have been presented in the literature: tunneling, dipole layer formation, protection during metal deposition and dissociation of LiF. In the presence of the LiF layer, sufficient potential difference may be maintained between Al and Alq_3 . This can result in tunneling injection. Hung et al., showed with photoelectron emission measurements that the energy bands of Alq_3 were bent downwards by more than 1 eV when the Alq_3 surface is in contact with LiF, thus lowering the electronic barrier height of Alq_3 -Al interface²⁶.

On the other hand, Yang et al. reported that the experimental results contradict with tunneling mechanism³⁰. The tunneling mechanism predicts a strong dependence of the electron injection to the thickness of the metal-fluoride layer. After investigating the performances of different thickness of LiF, CsF, CaF₂ and BaF₂ layers, the quantum efficiencies were found to be almost independent of the thickness of the fluoride layers within the range of 1-8 nm, as illustrated in Table 1. 1.

Table 1. 1: External QE and operating voltage of BaF₂/Al devices are presented (taken from Ref 30 without permission)

BaF₂ thickness (nm)	Voltage (V)	Current (mA)	QE (%)
8	5.0	27.8	2.4
4	5.0	26.0	2.3
2	5.0	33.8	2.3
1	5.0	23.0	2.3

It was reported that the effective work function of Al cathode was reduced significantly when LiF layer was introduced because the 1.0 V of open circuit voltage was increased to above 1.4 V³⁰. This shift of the effective work function of Al reduced the barrier height at the polymer/cathode interface, improved the quantum efficiency, and supported the aligned dipole mechanism initially proposed by Shaheen et al³¹. According to this mechanism, the LiF molecules (under the influence of Al nearby) induce dipole moments at the cathode interface. The large dipole moment decreases the surface potential of Al and also leads to a significant reduction of the effective work function. As a proof, Yang and coworkers reported the photoluminescence quantum efficiency (QE_{PL}) results in **Hata! Başvuru kaynağı bulunamadı.**³⁰. It can be observed from the results that thickness of the LiF layer does not change the efficiency significantly, but inserting a thin layer of Ba rather than LiF results in significant reduction of the QE_{PL}. This can be interpreted as alkali metals have much smaller cation size and larger mobility compared with alkaline-earth

metals, PL quenching would be expected if the alkali metal ions diffuse into the polymer layer.

Table 1. 2: EQ_{PL} of different structure devices based on MEH-PPV is presented (taken from Ref 30 without permission)

Structure	EQ _{PL}
Glass/MEH-PPV (100 nm)	18.9%
Glass/MEH-PPV (100 nm)/Al (150 nm)	14.8%
Glass/MEH-PPV (100 nm)/LiF (1 nm)/Al (150 nm)	15.6%
Glass/MEH-PPV (100 nm)/LiF (4 nm)/Al (150 nm)	15.4%
Glass/MEH-PPV (100 nm)/Ba (4 nm)/Al (150 nm)	12.2%

In addition to the Q_{EPL} results, the dipole mechanism claim was also supported by heating experiments. When devices with LiF/Al and BaF₂/Al cathode were heated, it was observed that the dipole moment is lost during operation of the LiF-containing device at 85 °C, as shown in Figure 1. 4. However, BaF₂/Al cathode showed a higher operation lifetime, and this supported the dipole mechanism that, at an elevated temperature, thermal movement at the interface creates disorder and decreases the orientation of the dipoles. Since the heavier metal fluoride is less mobile, a better lifetime is expected.

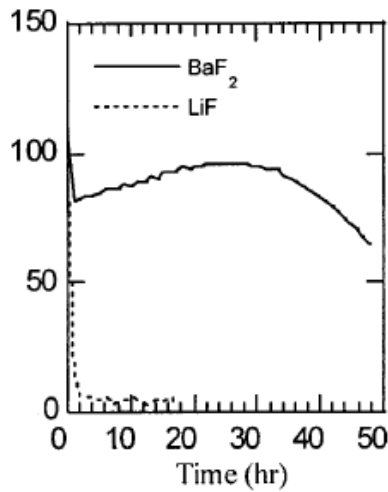


Figure 1. 4: Brightness decay under continuous operation at constant current at 85 °C for devices with a LiF/Al and BaF₂/Al cathode (taken from Ref 30 without permission)

Salaneck and coworkers studied the deposition of Li and LiF on poly(9,9-dioctyl-fluorene) (PFO)³². In the case of Li-deposition on PFO films, doping occurred and resulted in the formation of polaronic charge carriers at low doping levels and bipolaronic charge carriers at high doping levels. LiF-deposition on PFO did not cause doping of the polymer films, nor did the LiF dissociate at the interface. Neither significant shifts in a binding energy of the core levels nor any changes in the work function occurred. Hence, the Al/LiF/PFO interfaces are dramatically different from the ones reported for Alq₃. In PFO, no dissociation of LiF takes place and no new gap states are formed. There is no significant surface dipole formation at the LiF/PFO interface, though there is an evidence of a weak dipole at the interface between LiF and clean Al. Therefore, they suggest that for the case of PFO, and possibly other polymers as well, a thin LiF interfacial layer will mainly improve device performance by protecting the polymer during Al-deposition and reduce the number of quenching sites at the interface. The presence of LiF may also stabilize the interface and prevent diffusion of the metal atoms of the cathode.

Furthermore, Piroreun et al. showed that as in the case of Alq₃ with LiF/Al cathodes, introduction of a thin layer of CsF between MEH-PPV and Al leads to a considerable improvement in the device performance³³. To understand this, firstly the role of Al was explored by comparing devices, in which CsF later was covered with Al and Au. The difference was striking that no emission was observed, when Au was deposited on top the CsF. The experimental result lead to proposing the following mechanism: When Al is deposited on CsF, it attacks and dissociated it to form AlF₃, releasing metallic Cs. Since the Fermi level of Cs (work function 1.9 eV) is well above the LUMO of MEH-PPV (3.0 eV), Cs will dope MEH-PPV, creating an ohmic contact for electron injection. On the other hand, because Au is inert, the dissociation of CsF is prohibited and therefore the composite cathode does not dope MEH-PPV.

This mechanism was proved for LiF/Al cathodes afterwards by Y. D. Jin et al³⁴. They studied with poly [2-methoxy-5-(3',7'-dimethyloctyloxy)]-1,4-phenylene vinylene (OC1C10) with LiF modified cathodes. When cathodes with LiF rather than only Al were used it was observed that device performance improved significantly. This can be attributed to enhanced electron injection due to decrease of the electron injection barrier. Cathodes composed of ultra-thin films of LiF [0.6 nm)/Al(1 nm) or LiF:Al (2 nm) covered

by Ag (100 nm) show the same performance as LiF(0.6 nm)/Al bilayer cathode or a LiF:Al composite cathode, indicating that the enhancement is specific to LiF and Al. Thus, those experiments can be concluded as Li-ions can dissociate from LiF and diffuse into the OC1OC10 layer, leading to an n-type zone close to the polymer/cathode interface. This n-doped layer at the interface facilitated electron injection at the cathode/polymer interface and eventually leads to the formation of ohmic contact.

The controversial role of LiF for organic photovoltaics is not very different. It has been reported by several groups that insertion of a thin LiF layer improves device performance and increases the efficiency but the real mechanism is still not well understood^{35,36,37}. However, in general LiF is believed to reduce the barrier height between polymer blend film and the electrode either through the lower effective work function of LiF or through the dipole alignment of LiF nanoparticles³⁶. Moreover, it has been also reported that for an Al and C₆₀ interfaces, LiF introduction provides effective passivation for the contacts by preventing Al oxidation³⁸. This is noteworthy for C₆₀/Al contacts because it was previously reported that these contacts degrade from an ohmic contact to a blocking one after exposure to air due to the emergence of a potential barrier between the top electrode Al and C₆₀ film³⁹. In addition, C₆₀ is very sensitive to oxygen and moisture that upon oxygen adsorption the decrease in the conductivity for several orders of magnitude was reported⁴⁰. However, by addition of 0.5 nm LiF interlayer at the Al/C₆₀ interface can successfully suppress the interfacial oxidation which degrades the electrical contact⁴¹.

Thus, addition of LiF between organic layer and metal cathode improves the performance of device. However, as the general trend in research and development of photovoltaic elements is aiming more and more for low cost devices and advances in non vacuum deposition of metals and use of active layers from solution processed polymer blends necessitates non vacuum techniques for interlayer formation^{24,42,43}. Therefore, it is important to achieve production of LiF layers with non vacuum techniques for the realization of fully ambient manufacturing of organic devices.

1.3 Nanotransfer Printing

With the recent advances in nanofabrication, either through “top-down” or “bottom-up” techniques, the use of nanostructures with exceptional properties in new applications such as electronics, biomedicine, and materials science has engendered growing interest in nanotechnology^{44,45}. New emerging technologies require the integration of small-sized materials to be organized in new, higher-ordered systems. In most cases, it is easier to produce nanoscale objects on different surfaces by lithographic techniques based on molding, embossing and printing^{46,47,48}.

Molding and embossing techniques can be divided in two categories, according to the stiffness of the mold: (i) molding and embossing nanostructures with a hard mold and (ii) molding and embossing of nanostructures with a soft (elastomeric) mold⁴⁹. Molding is a conventional method that is being used in industry for the production of materials. For nanofabrication purposes, molding usually involves curing a precursor against a topographically patterned substrate at the nanoscale. On the other hand, embossing, also known as imprinting, technique involves transfer of the mold with topographical structures into an initially flat polymer film. Among the different embossing techniques, nanoimprint lithography is worthy of more detailed description.

Nanoimprint lithography (NIL) is used to transfer patterns from a rigid mold to a thermoplastic polymer film heated above its glass transition temperature with the assist of pressure (as given in Figure 1. 5a)⁴⁹. Because this method involves heating, it can also be also called “hot embossing”. It was reported that for application in nanogap metal contacts, NIL allowed fabrication of 5 nm linewidth and 14 nm linepitch in resist and uniform patterning in a full 4 inch wafer⁵⁰.

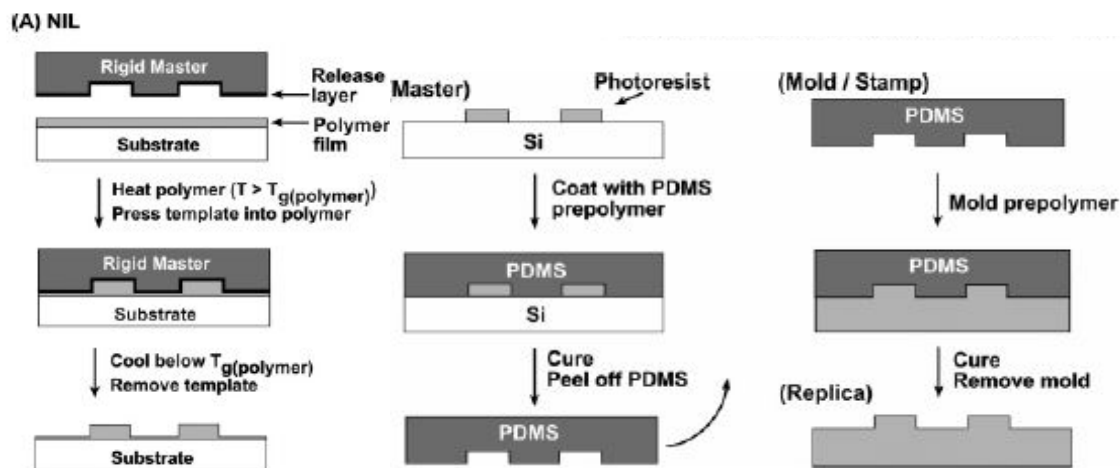


Figure 1. 5: Schematic illustration of nanoimprint lithography (NIL) (a) and schematic illustration of the formation of topographically patterned molds (or stamps, depending on the application) and replication (taken from Ref 49 without permission)

Soft pattern elements of embossing involve preparation of a soft mold or stamp by casting a liquid polymer precursor against a topographically patterned master (see Figure 1. 5b). For such purposes an elastomer, such as poly(dimethylsiloxane) (PDMS), have been successfully employed⁵¹. Apart from being an elastomer, PDMS has number of useful properties in nanofabrication such as being durable, unreactive towards most materials being patterned or molded, and being chemically resistant to many solvents. Probably, one of the most important features of PDMS is its low cost of fabrication in the form of molds and stamps. In addition, PDMS has a low surface energy (19.8 mJ/m^2), and it allows PDMS to be easily released after molding⁵². The advantage of being a soft elastomer can be a double-edged sword when it comes to replication of nanoscale features. However, it is possible to increase surface energy of PDMS for increasing adhesion to a substrate, by exposing the surface to oxygen plasma temporarily. The hydrophilicity of the surface can be delayed by thermal aging⁵³. Due to its low tensile modulus (1.8 MPa) 184-PDMS (Dow Corning) has limited use in nano-imprinting⁵⁴. Higher resolution masters can be produced by use of harder elastomers such as hard PDMS (h-PDMS), which has a higher tensile modulus (8.2 MPa)^{55,56}. H-PDMS can perform molding and patterning of smooth, sub-100 nm structures, and therefore allow true nano-patterning. In addition, in a classical micro-contact printing scheme, h-PDMS can be used to transfer functional biological molecules⁵⁶. However, h-PDMS has helped to achieve resolutions about 50 nm, albeit only for features that are not densely spaced together and of high aspect ratio. By utilizing a similar

mold hardness of polyurethane acrylate (PUA), which is UV-curable, it is possible to make nanoholes with a low-pressure detachment and nanolithography-based technique ⁵⁷. However, again the resolution of such a mold is limited to 50 nm. Therefore, even harder mold materials are needed to pattern scales smaller than 50 nm. For this reason, rather than using only PDMS, McGehee and coworkers used both PDMS and poly(methyl methacrylate) (PMMA) to pattern below 10 nm resolution ⁵⁸. In their study, they used porous anodic alumina as template and used thermal infiltration to fill the narrow pores with PMMA. Thin layer of PMMA covered with thick layer of PDMS was used as the mold material so that the mold would be permeable, but mechanically stable and flexible. Fabricated molds helped the patterning of dense arrays of deep, narrow, straight pores in TiO₂, a semiconductor that is often used in photovoltaic and photocatalytic applications (see below Figure 1. 6 and Figure 1. 7).

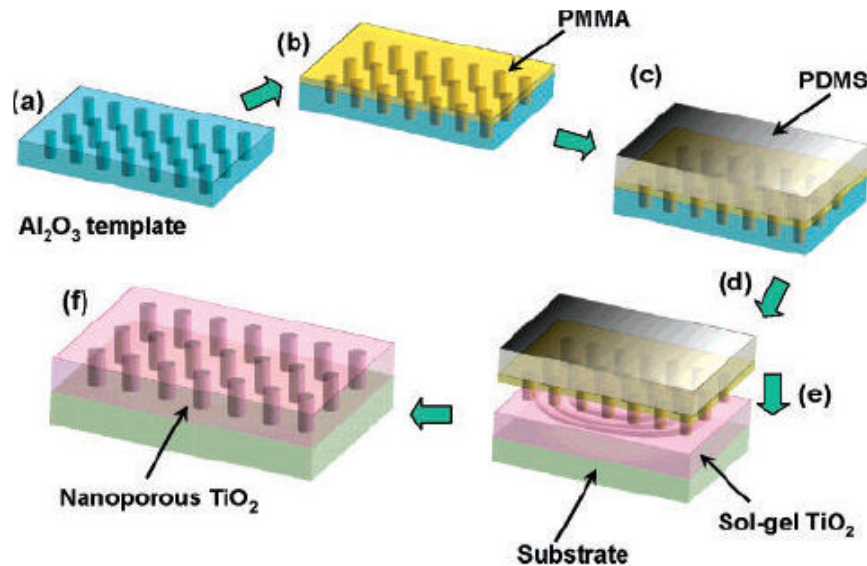


Figure 1. 6: Schematic diagram of the processes involved in embossing titania: (a) preparing AAO template, (b) infiltrating PMMA, (c) coating on PDMS (d) retrieving mold by wet chemical etching, (e) embossing sol-gel TiO₂ and (f) removing the mold (taken from Ref 58 without permission)

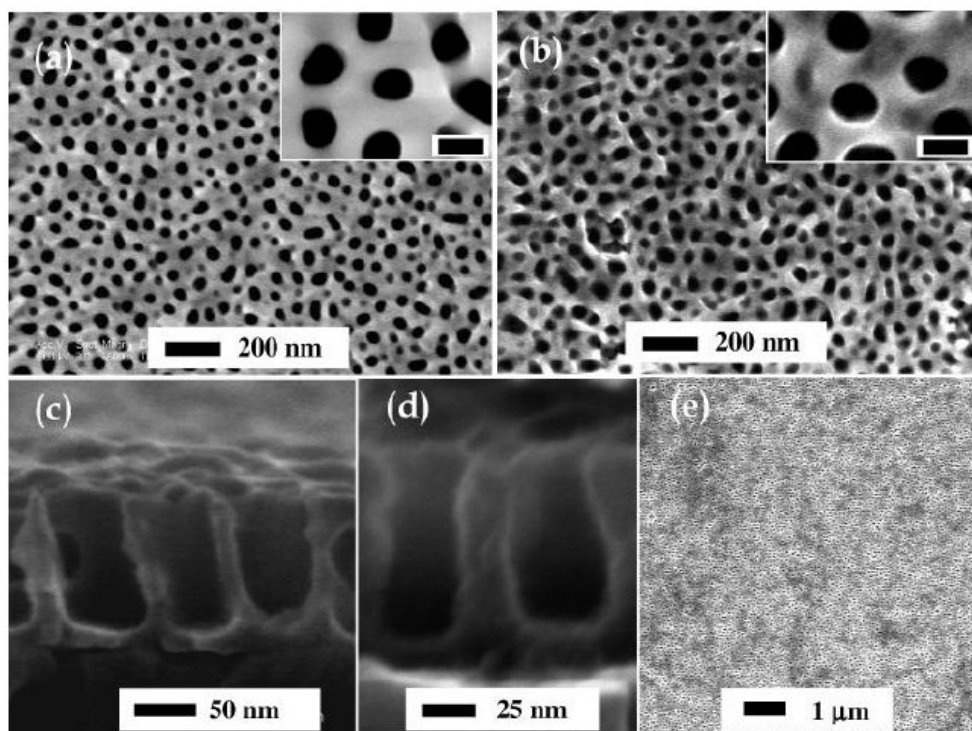


Figure 1. 7: SEM images of (a) typical initial AAO template, (b) typical embossed TiO₂ structures after PMMA removal with acetonitrile (c) embossed TiO₂ structures (d) smaller-diameter pores with one showing 20 nm diameter, and (e) embossed TiO₂ at a larger scale showing uniformity of the replication. (taken from Ref 58 without permission)

PDMS has also been used for transfer printing of nanoscale objects. In this respect, nanotransfer printing (nTP) by the use of PDMS departs from the systems that use specific covalent interactions. The advantage lies again in low surface energy of PDMS, which allows the release of materials on a surface. In addition, because the method is not using specific covalent interactions, PDMS can transfer a considerable range of materials on wide variety of surfaces. Rogers and coworkers successfully employed PDMS in the transfer of Au patterns onto a polyethylene terephthalate (PET) substrate through covalent bonding between the Au and the PET surfaces⁵⁹. Initially, Au was evaporated onto a patterned PDMS. Metal-coated PDMS was brought gently into contact with a PET substrate and no external pressure was applied. Upon heating, the PDMS stamp was removed, and Au patterns were transfer printed onto the PET surface as illustrated in Figure 1. 8. The transfer mechanism here is based on the different adhesion strengths between PDMS-metal and the substrate-metal interfaces. The difference in the work of

adhesion of these two interfaces, substrate-metal ($W_{\text{sub-metal}}$) and PDMS-metal ($W_{\text{PDMS-metal}}$), in intimate contact, can be written as:

$$W_{\text{sub-metal}} - W_{\text{PDMS-metal}} = (\gamma_{\text{sub}} - \gamma_{\text{PDMS}}) - (\gamma_{\text{sub-metal}} - \gamma_{\text{PDMS-metal}}),$$

where γ symbolizes the surface energies of substrate, metal and PDMS with subscripts. By considering that the surface energy of metal is the highest among three, the difference in work of adhesion is roughly equal to the difference in surface energy of the substrate and the PDMS. Although the surface energy of PDMS can be as low as 19.8 mJ/mm², electron beam-evaporated metal films increase the intrinsic surface energy of PDMS. Therefore, the authors used an additional heating step, which might decrease the surface energy of PDMS, by accelerating the surface recovery. With such a method, transfer printing on surfaces such as polythiophene (38.0 mJ/m²), polyimide (KaptonTM; 37.4 mJ/m²), MEH-PPV (28.0 mJ/m²) and pentacene (23.7 mJ/m²) was achieved. Increasing stamping temperature to 80 °C decreased the full transfer time. After analyzing different cases, the authors concluded that *temperature, contact time, surface energy and substrate roughness* are the main parameters that govern the noncovalent transfer process⁵⁹.

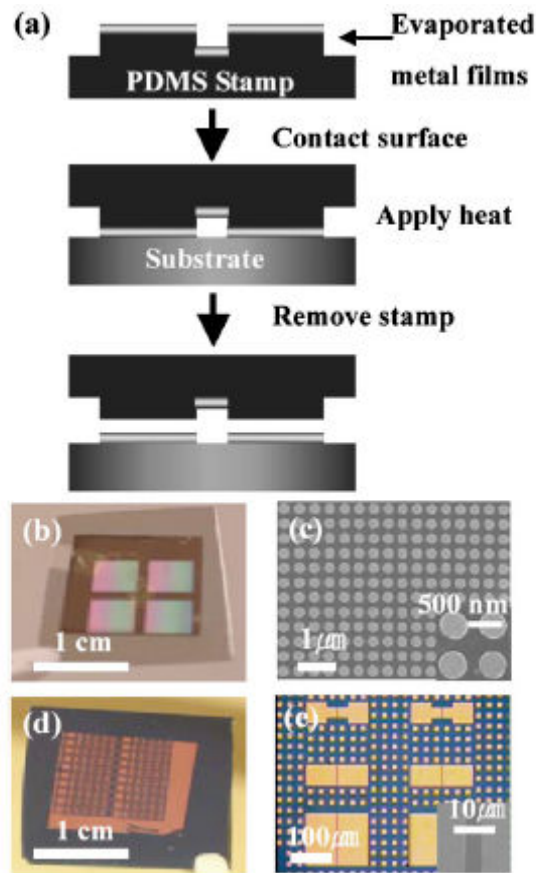


Figure 1. 8: (a) Schematic illustration of steps for noncovalent transfer printing. Contacting a metal coated stamp to a substrate, followed by moderate heating causes the metal to remain on the substrate after removing the stamp. (b) Optical micrograph of arrays of Au (30 nm thick) dots printed over an area of 0.5 cm× 0.5 cm on a plastic substrate. (c) SEM micrograph of a small region of the printed pattern. (d) Optical micrograph of various Ti(2nm)/Au(30 nm) device patterns printed onto a SiO₂/Si substrate. (e) Optical and SEM micrographs of a small region of the printed pattern. (Taken from Ref 59 without permission)

PDMS was also used to grab and release nano objects simultaneously to achieve transfer printing by kinetic control of adhesion. The technique presented by Meitl et al. relies on kinetically controllable adhesion of a viscoelastic stamp of PDMS⁶⁰. The process depicted in Figure 1. 9 begins with the preparation of a donor substrate that supports small solid objects, which can be prepared with top-down or bottom-up fabrication. Upon placing the elastomeric stamp on top of a donor substrate, conformal contact was achieved, and adhesion forces were dominated by van der Waals interactions. This adhesion between solid objects and the stamp was shown to be rate-sensitive. If the stamp was pulled away from the donor substrate with sufficiently high peeling velocities ($\sim 10 \text{ cm s}^{-1}$), the adhesion was then strong enough to adhere solid objects preferentially to the surface of the stamp.

Thus, when the peeling speed is high, the adhesion of rubber is high and as the peeling speed is increased the adhesion of the rubber decreases. In that case, the separation energy of PDMS and microstructure is rate (v) dependent owing to the viscous behavior of PDMS, that is $G_{\text{PDMS}}=G_0[1+\phi(v)]$. In contrast, the separation energy for the microstructure-substrate interface $G_{\text{substrate}}$ is typically independent of rate. To break the microstructure-substrate interface, the rate of delamination should be high enough such that the elastomer-microstructure interface becomes stronger. The inked stamp was brought into contact with the receiving (device) substrate. When the stamp was removed with a low peeling velocity ($\sim 1 \text{ mm s}^{-1}$), objects on the stamp adhered preferentially to the device substrate. Apart from being robust and inexpensive, the technique can enable the printing of objects with a wide range of shapes and sizes onto virtually any smooth substrate (roughness of less than $\sim 3 \text{ nm}$ over $1 \text{ }\mu\text{m}^2$). As illustrated in Figure 1. 10 with the kinetic adhesion control of PDMS, solid objects with different geometries such as sheet like and spheres, mica and graphene sheets, and biological samples such as pollens grains can be transfer printed on a smooth receiver substrate. The rate dependent adhesiveness of elastomeric materials can be explained by looking rate process theory ⁷⁶. Usually what is expected for dry, hard, macroscopic materials is that friction decreases at the onset of sliding, and as velocity increases, friction continues to decrease because of a reduction in the number of interfacial contacts. On the contrary, in the rate process approach for elastomers, friction is expressed as a product of the density of bonded molecular chains and the sum of the bearing (support) forces of stretched bonded molecular chains. Using the rate process approach, the friction attains a peak (maximum) value that is good agreement with the value observed experimentally.

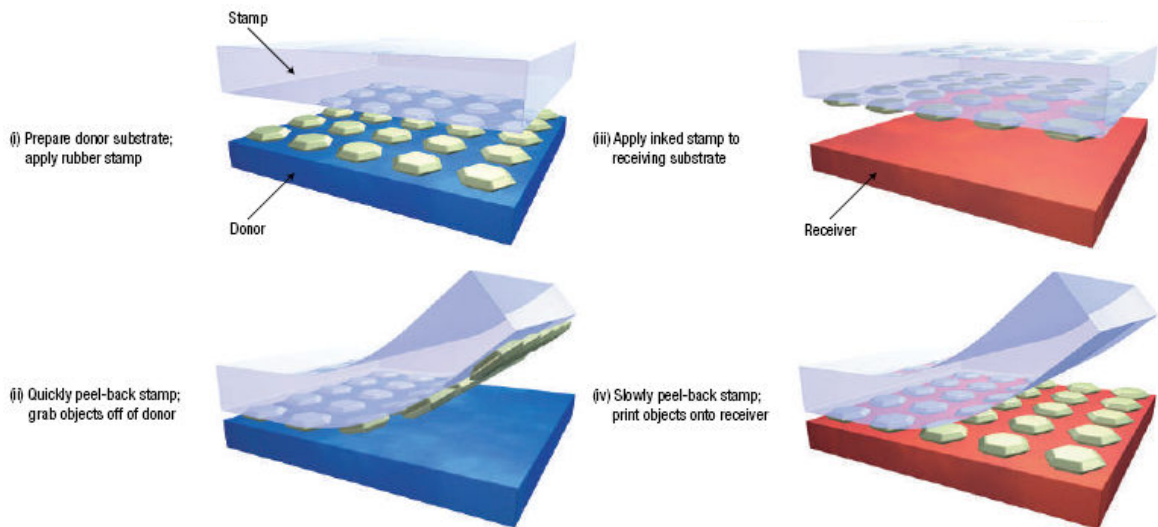


Figure 1. 9: Schematic illustration of the generic process flow for the transfer printing solid objects. The process begins with the preparation of an assemblage of microstructures on a donor substrate by solution casting, micromachining, self-assembly or other suitable means. (i) Laminating a stamp against a donor substrate and then quickly peeling it away (ii) pulls the microstructures from the donor substrate onto the stamp. Contacting the stamp to another substrate (receiving substrate (iii)) and then slowly peeling it away transfers the microstructures from the stamp to the receiver (iv). The peeling rate determines the strength of adhesion and, therefore, the direction of the transfer. (Taken from Ref 60 without permission)

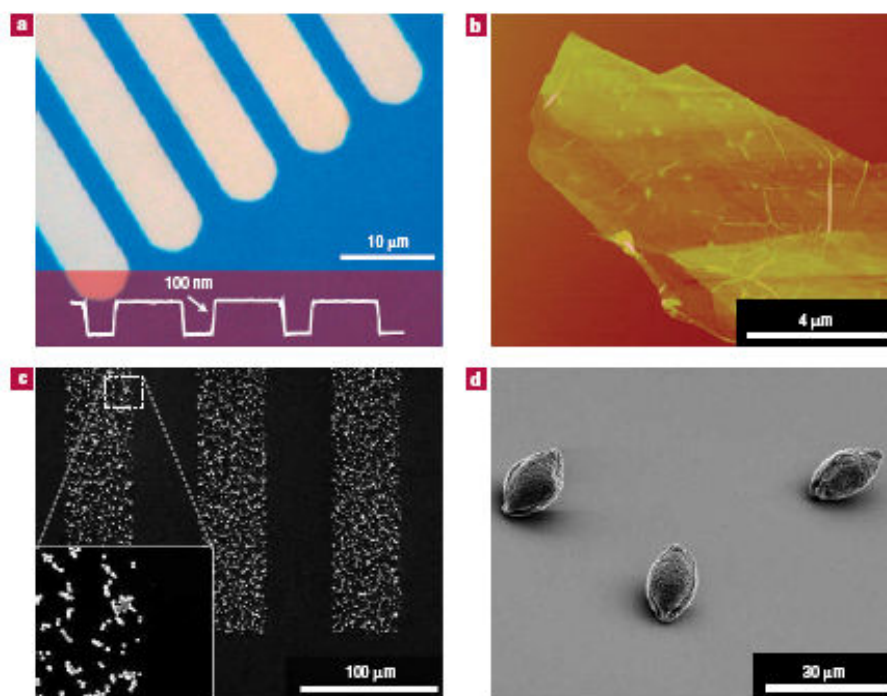


Figure 1. 10: Images of transfer printed objects with sheet-like and globular geometries. a, 100-nm-thick mica ribbons cleaved from a mica substrate with a PDMS stamp, and then transfer-printed onto SiO₂ (blue). b, Graphite sheet, ranging from 3 to 12 nm thick, cleaved from a highly ordered pyrolytic graphite substrate and printed onto SiO₂ with a stamp. c,d, Silica microspheres (c) and African Violet pollen grains (d) picked up from and subsequently printed onto silicon wafers by means of PDMS stamps. Relief features in the stamp define the stripe pattern in c. (Taken from Ref 60 without permission)

Nanoprinting techniques were also enhanced through the use of a self-assembling monolayer (SAM). In such methods, SAM molecules facilitate the transfer of the nano-sized objects from donor substrate to receiver substrate⁶¹. Rogers and coworkers achieved the transfer printing of a 20-nm thick Au film from PDMS to a gallium arsenide (GaAs) surface, by using alkane dithiol monolayers⁶². The transfer printing process is outlined in Figure 1. 11. Initially, the PDMS stamp was prepared with the desired features, and a Au film of 15-20-nm thickness was evaporated on top. At the same time, GaAs was coated with an alkane dithiol SAM, which covalently bonded with the surface through the formation of S-H bonds. Then, the Au-coated stamp was brought into contact with the SAM-coated GaAs surface. A flexible structure of elastomeric PDMS helped the formation of conformal contact, without the need to apply pressure. After removal of the stamp in 15 s, the Au layer remained on the GaAs surface, by forming a covalent bond with the terminal S of alkane dithiol. Thus, with the aid of the SAM, accurate printing of Au can be

achieved. This system can be used for printing different metals that can form a chemical bond with the thiol group. With a similar approach, through utilizing the adhesion of hydrogen silsequioxane (HSQ), Au patterns on Si were transferred to a Si coated with HSQ by Matsui et al ⁶³.

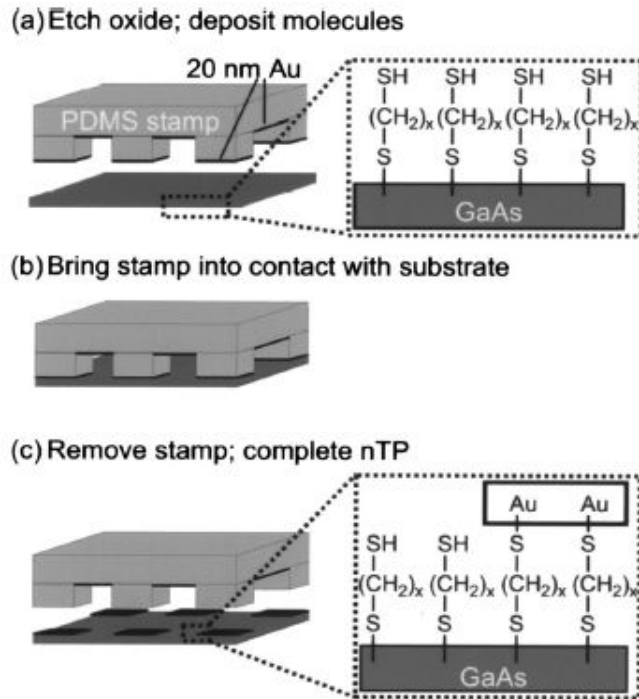


Figure 1. 11: Schematic illustration of nanotransfer printing (nTP) on GaAs: (a) native oxide is removed from the wafer surface before 1,8-octanedithiol molecules are deposited; (b) a gold-coated (20 nm) elastomeric stamp is brought into contact with the treated surface; and (c) the stamp is removed to complete the printing. (Taken from Ref 62 without permission)

SAMs and other material-specific covalent interactions were also used for the transfer printing of nanoparticles ⁶⁴. Huskens and colleagues employed the self-assembly of silanes to pattern negatively charged (by carboxylate functionalization) PS and SiO₂ nanoparticles on a silicon oxide surface via capillary-assisted assembly ⁶⁵. Figure 1. 12 depicts the multistep nanofabrication process used to produce the two kinds of patterned colloidal substrates. Nano imprint lithography was performed on PMMA films spin-coated on silicon oxide substrates. After removing the residual PMMA layer in O₂ plasma, silane SAMs were deposited from the gas phase onto the unprotected areas of the substrate. Deposition of the aminoalkyl SAM resulted in substrates, which were both topographically and chemically patterned. Alternatively, the substrate was initially functionalized with an

alkyl SAM, followed by removal of the PMMA by sonication in acetone and the deposition of aminoalkyl SAM from the gas phase onto areas previously covered by PMMA. This led to topographically flat, solely chemically functionalized templates. The templates were then dip-coated into a colloidal solution, which assisted the assembly of nanoparticles by capillary forces stemming from the meniscus formed at the three-phase contact line. By topographical confinement, a resolution of 60 nm was achieved for single particle-wide lines of functionalized nanoparticles attached to 60 nm imprinted aminoalkyl SAM lines, while resolutions of 300 nm were achieved on chemically confined substrates. Patterned silica particles are shown in Figure 1. 13.

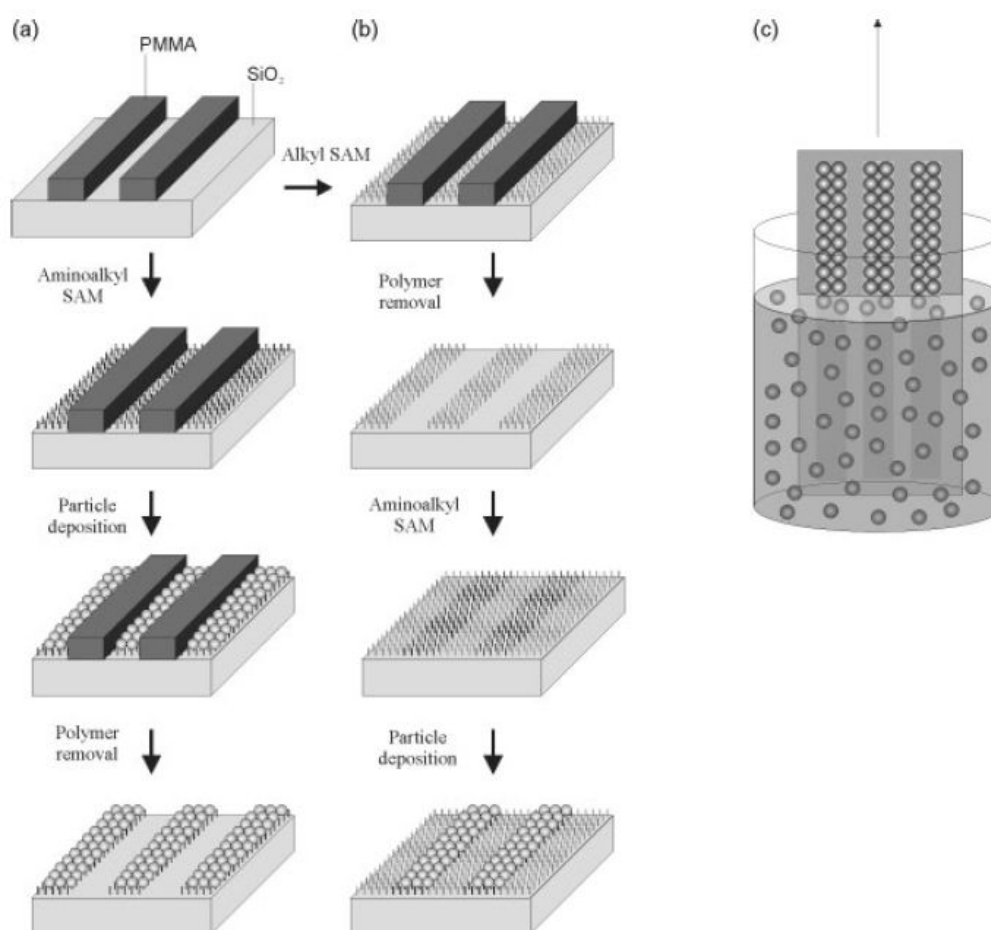


Figure 1. 12: a-c) Schematic representation of the processes to fabricate patterns of nanoparticles using chemical templates in combination with (a) or without physical barriers (b). The polymer templates were prepared by nanoimprint lithography, SAMs were formed by gas phase deposition, and nanoparticles were attached using a vertical deposition set-up (c), in which the samples were withdrawn vertically from the nanoparticle suspension. (Taken from Ref 65 without permission)

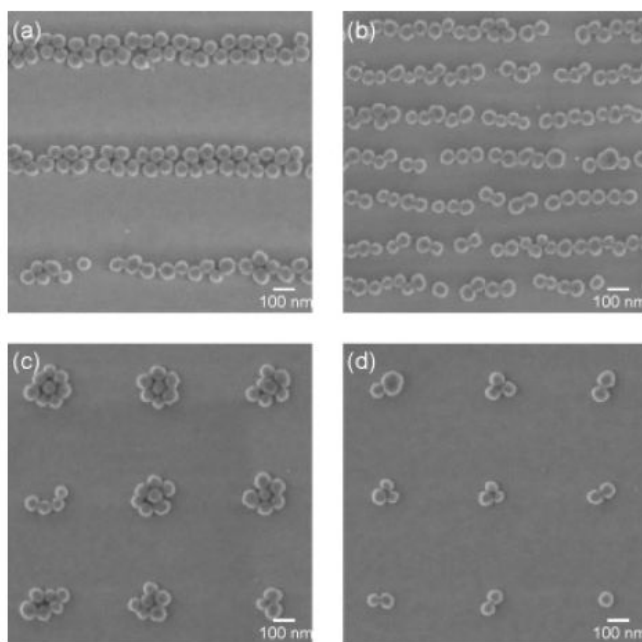


Figure 1. 13: SEM images of 55 nm carboxylate-functionalized SiO₂ nanoparticles assembled on PMMA-imprinted sub-300 nm patterns with aminoalkyl SAMs. The initial polymer height was 100 nm, and the residual layer was removed by exposure to O₂ plasma for 10 s. The withdrawal speed was 1 μm s⁻¹. After particle adsorption, the polymer template was removed by sonication in acetone for 1 min. The effect of confinement on the particle assembly is apparent by using lines with linewidths of a) 100 nm and b) 60 nm, and holes with diameters of c) 180 nm and d) 100 nm. (Taken from Ref 65 without permission)

Buriak and coworkers combined the flexibility of a PDMS mold with a SAM to transfer nanoparticles⁶⁶. They initially formed hexagonally close-packed nanoparticles on a silicon substrate via the use of self-assembled block copolymer (PS-*b*-P2VP) templates. Nanoparticles were then transferred onto a surface of PDMS through a simple peel-off procedure. By modulation of the molecular weight of the PS and/or P2VP blocks, nanopatterns of various metals can be synthesized with center to center spacing of 50-180 nm and nanoparticle diameters of 10-70 nm. The reaction employed in this study was palladium (Pd) nanoparticle catalyzed hydrosilylation of terminal alkenes/alkynes on H-terminated silicon surfaces. Upon Pd patterning of PDMS surface, catalytic stamp was inked with dilute solution of terminal alkenes for 1 min and then applied to freshly prepared flat H-terminated silicon (illustrated in Figure 1. 14). Stamping was normally carried out for 20 min under light continuous pressure. The subsequent release of the

catalytic stamp resulted in a duplication of the original pattern of Pd nanoparticles on the silicon surface with arrays of alkyl/alkenyl groups covalently attached to silicon surface; the released stamp was reusable for subsequent inking/stamping. Figure 1. 15 summarizes the results of catalytic stamp lithography and its subsequent use as an etch stop using 1,4-dioxane solution of 1-octadecyne as an ink. The study is valuable in terms of replacing expensive top-down techniques with a bottom-up approach for nanofabrication. On the other hand, although the group claimed that the process is simple, the peel-off step involves series of complicated chemical modifications and their approach is limited to metal nanoparticles such as palladium (Pd) and Au.

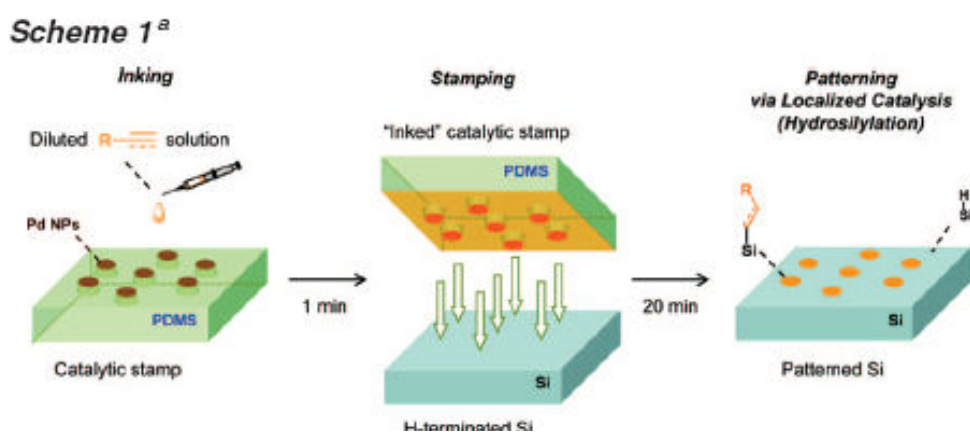


Figure 1. 14: Typical reaction conditions for catalytic stamp lithography (1 min inking and 20 min stamping) and the concept of localized catalysis. Catalytic hydrosilylation takes place only underneath Pd nanoparticles. (Taken from Ref 66 without permission)

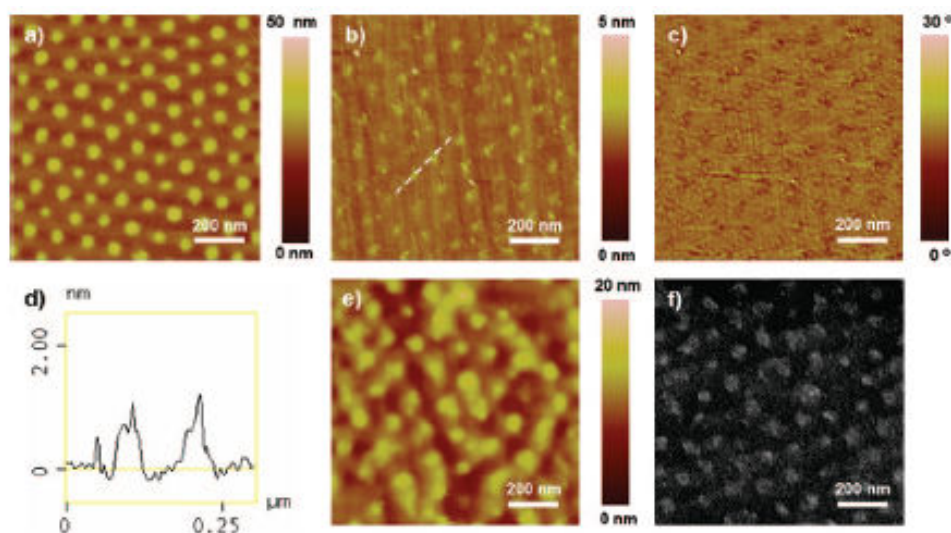


Figure 1. 15: (a) AFM height image of a parent Pd catalytic stamp with nanoparticle diameters of 40 nm and a center-to-center spacing of 110 nm. (b) 1-Octadecyne-stamped Si(111)-H surface and corresponding phase image (c). (d) Section analysis along the dashed line in (b). (e) AFM height image of a 1-octadecyne-stamped Si(111)-H surface, followed by wet chemical etching with 40% NH_4F (aq). (f) SEM image of the sample from (e). (Taken from Ref 66 without permission)

Hexagonal arrangement of nanoparticles via diblock copolymer templating was also used for replication of DNA nanoarrays by Akbulut et al.⁶⁷. In their work they demonstrated supramolecular nanostamping for the stamping of DNA arrays with features as small as 14 ± 2 nm spaced 77 ± 10 nm. Moreover, they demonstrated that hybridization of these nanoarrays can be detected using atomic force microscope in a simple and scalable way that additionally does not require labeling of the DNA strands. The process flow as well as AFM results is given in Figure 1. 16 and it involves three steps: (1) hybridization, (2) contact, and (3) dehybridization. Initially a master was prepared by Au nanoparticle synthesis with the aid of PS-*b*-P2VP diblock copolymer micelles and hexagonal arrangement of nanoparticles on chromium layer with spin coating. To achieve arrays of DNA features on flat surfaces, thiolated DNA was attached onto an array of evenly spaced Au nanoparticles. Then the master made of single stranded DNA features is immersed in a solution containing complementary DNA molecules terminated with chemical groups that can bind to a target surface (hybridization). Once hybridization has occurred, a secondary substrate is placed onto the master (contact) to allow for bond formation between this surface and the end groups of the complementary DNA strands. Afterward the master and the secondary substrate are separated (dehybridization) by gentle heating. Although the supramolecular nanostamping procedure outlined here has a significant resolution

advantage over other soft-material stamping methods, chemical specificity limits the application of the replication technique to wider variety of materials.

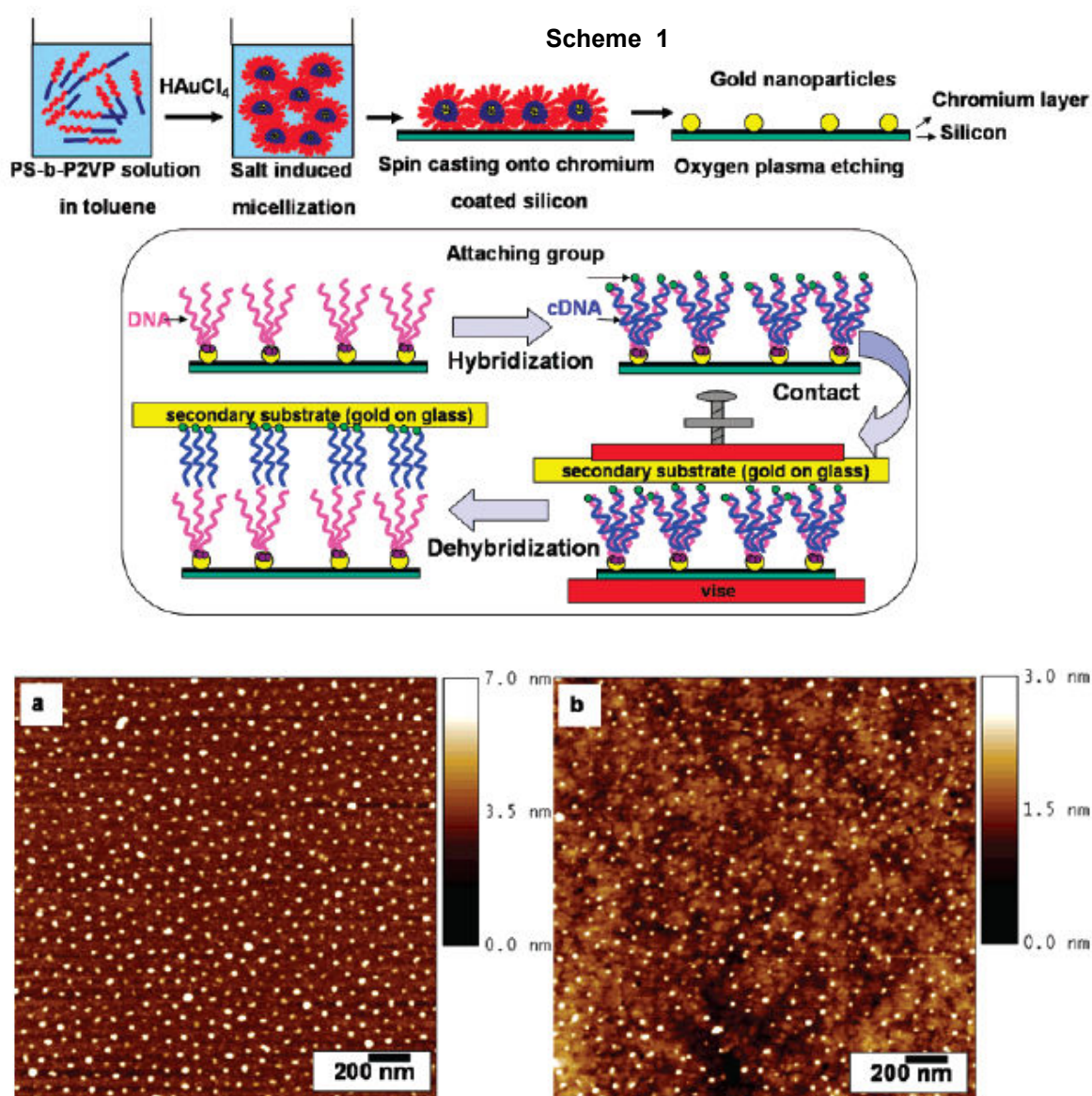


Figure 1. 16: Scheme 1) gold nanoparticle preparation and supramolecular nanostamping cycle, (a) AFM height image of Au nanoparticle master (b) AFM height image of printed pattern (Taken from Ref 67 without permission)

Apart from generic covalent and noncovalent (van der Waals) forces, direct electrostatic forces were also employed for nanotransfer printing^{68,69,70,71,72}. Jacobs et al. demonstrated electrostatic patterning on PMMA surface with nanometer resolution in several studies. In general, patterned PDMS was coated with 100 nm thick Au film and the stamp was overall supported either by glass or copper (depicted in Figure 1. 17 LEFT). Patterned stamp was brought in contact with thin (80 nm) PMMA film coated on silicon substrate (for which the

native oxide layer was removed for electrical conductivity). PDMS here, as a soft elastomer, provide conformal contact between substrate and PMMA and ensuring high area (1 cm²) patterning. After forming the contact, an external bias was applied to pattern charges on PMMA. This process is resulted from the electret nature of PMMA that allows generation of trapped charges which are stable in different media. Patterned charges of PMMA can be characterized with Kelvin probe force microscopy. Among different applications of the charged patterns, xerography of small particles is the outstanding one. Either by immersing the stamp into a colloidal nanoparticle solution or exposing the stamp to gas phase nanoparticles, directed assembly of different polarizable nanoparticles can be achieved with the electrostatic printing technique (shown in Figure 1. 17 RIGHT). Moreover, these particles on PMMA can be transferred to PDMS or a adhesive tape by just peeling as illustrated in the small sections of Figure 1. 17 RIGHT.

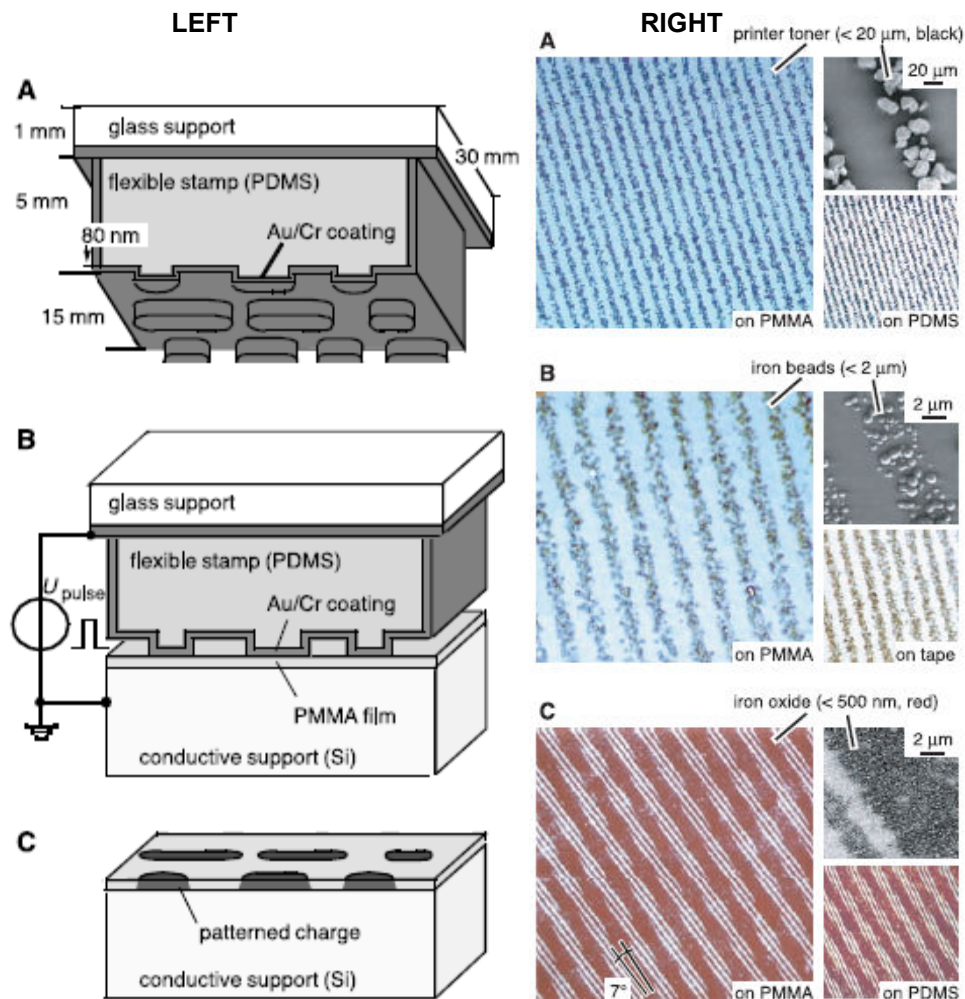


Figure 1. 17: (LEFT) Principle of electrical micro contact printing. (A) The flexible, metal-coated stamp is placed on top of a thin film of PMMA supported on a doped, electrically conducting silicon wafer. (B) An external voltage was applied between the Au and the silicon to write pattern of the stamp into the electret. (C) The stamp was removed; the PMMA was left with a patterned electrostatic potential. (RIGHT) Optical microscope and SEM images of different types of particles trapped at patterned charge and transferred onto second substrates. (A) 50- μm -wide parallel lines of toner particles, $<20\ \mu\text{m}$ in size; (B) 5- μm -wide parallel lines of iron beads, $<2\ \mu\text{m}$ in size; (C) 2.5 and 10- μm -wide lines of red iron oxide particles, $<500\ \text{nm}$ in size. (Taken from Ref 68 without permission)

There are number of factors which determine the resolution achievable in printing^{49,73}:

- (i) size and stability (mechanical, etc) of the smallest features on the stamp;
- (ii) larger scale deformations of the stamp;
- (iii) lateral dimension and uniformity of the ink materials;
- (iv) control over the differential adhesion of the printed material to the stamp and substrate.

The resolution and dimensions of nanoscale features transferred from the stamps primarily depends on the interaction of the ink with the printed surface. In addition, it depends on the integrity of the transferred material. Moreover, preferential adhesion of the material to be printed depends on the easy removal of materials from the stamp. This can be achieved by decreasing the surface energy of the stamp and increasing the surface energy of printed surface. The formation of covalent bonds between the transferred material and the printed surface can also improve the release from the stamp. These parameters should be optimized for different systems for effective transfer printing in nanoscale.

1.4 Aim of the Thesis

The overall objective in this thesis was investigating of the mechanism by which LiF enhances electron and hole extraction in the electrode bilayer in organic photovoltaics (OPVs). This required the synthesis of LiF nanoparticles in micelle reactors, which would enable the controlled monolayer deposition of LiF particles at the electrode and organic interface. The work function of the engendered electrode bilayer is characterized, as well as the I-V characteristics of a model device integrating such a solution-processed LiF layer. Finally, to realize the integration of a highly ordered, solution-processed LiF particle layer into an actual OPV, nanoscale transfer printing was explored.

Chapter 1 References

1. Li, X.-M., Parasciv, V., Huskens, J., Reinhoudt, D. N., Sulfonic Acid-functionalized gold nanoparticles: a colloidal bound catalyst for soft lithographic application on self assembled monolayers. *J. Am. Chem. Soc.* **125**, 4279-4284 (2003).
2. Shipway, A. N., Katz, E., Willner, I., Nanoparticle Arrays on Surfaces for Electronic, Optical, and Sensor Applications. *CHEMPHYSICHEM* **1**, 18-50 (2000).
3. Sant, P. A., Kamat, P. V., Interparticle electron transfer between size-quantized CdS and TiO₂ semiconductor nanoclusters. *Pyhs. Chem. Chem. Phys.* **4**, 198-203 (2002).
4. Bishop, K. J., Christopher, E. W., Soh, S., Grybowski, B. A., Nanoscale Forces and Their Uses in Self Assembly. *Small* **5**, 1600-1630 (2009).
5. Foerster, S., Antonietti, M., Amphiphilic Block Copolymers in Structure-Controlled Nanomaterial Hybrids. *Advanced Materials* **10**, 195-217 (1998).
6. Anonietti, M., Wenz, E., Bronstein, L., Seregina, M., Synthesis and Characterization of Noble Metal Colloids in Block Copolymer Micelles. *Advanced Materials* **7**, 1000-1005 (1995).
7. Spatz, J. P., Roechester, A., Sheiko, S., Kraush, G., Möller, M., Noble Metal Loaded Block Ionomers: Micelle Organization, Adsorption of Free Chains and Formation of Thin Films. *Advanced Materials* **7**, 731-735 (1995).
8. Spatz, J. P., Sheiko, S., Möller, M. Ion-Stabilized Block Copolymer Micelles: Film Formation and Intermicellar Interaction. *Macromolecules* **29**, 3220-3226 (1996).
9. Borisov, O, Zhulina, E. B., Effect of Salt on Self-assembly in Charged Block Copolymer Micelles. *Macromolecules* **35**, 4472-4480 (2002).
10. Zhulina, E.B., Birshtein, T. M, Scaling Theory of Supermolecular Structures in Block Copolymer-Solvent Systems: 1. Model of Micellar Structures. *Polymer* **30**, 170-177 (1989).
11. Aizawa, M., Buriak., J. M., Block Copolymer Templated Chemistry for the Formation of Metallic Nanoparticle Arrays on Semiconductor Surfaces. *Chemistry of Materials* **19**, 5090-5101 (2007).
12. Xu, W., Atkins, D. L., Reverse micellar synthesis of CdS nanoparticles and self-assembly into superlattice. *Materials Letters* **58**, 2623-2626 (2004).
13. Chandrasekharan, N., Kamat, P. V., Tuning the properties of CdSe nanoparticles in reverse micelles. *Res. Chem. Intermed.* **28**, 847-856 (2002).

14. El-Atwani, O., Aytun, T., Mutaf, O. F., Srot, V., van Aken, P. A., Ow-Yang, C. W., Determining the Morphology of Polystyrene-block-poly(2-vinylpyridine) Micellar Reactors for ZnO Nanoparticle Synthesis. *Langmuir* **26**, 7431-7436 (2010).
15. Fendler, J. H. (Ed.), *Nanoparticles and Nanostructured Films*. Bronstein, L., Antonietti, M., Valetsky, P., Chapter 7, Metal Colloids in Block Copolymer Micelles: Formation and Material Properties. WILEY-VCH Verlag GmbH, 1998.
16. Lu, J. Q., Yi, S. S., Uniformly Sized Gold Nanoparticles Derived from PS-b-P2VP Block Copolymer Templates for the Controllable Synthesis of Si Nanowires. *Langmuir* **22**, 3951-3954 (2006).
17. Aizawa, M., Buriak, J. M., Nanoscale Patterning of Two Metals on Silicon Surfaces Using an ABC Triblock Copolymer. *J. Am. Chem. Soc.* **128**, 5877-5886 (2006).
18. Haupt, M., Miller, S., Ladenburger, A., Sauer, R., Thonke, K., Riethmueller S., Moeller, M., Banhart, F., Semiconductor Nanostructures Defined by Self-Organizing Polymers. *Mat. Res. Soc. Symp. Proc.* **728**, 1-6 (2002).
19. Lee, C., Kwon, J.-H., Lee, J.-S., Kim, Y.-M., Shin, H., Lee, J., Sohn, B.-H., Nonvolatile Nanocrystal Charge Trap Flash Memory Devices Using a Micellar Route to Ordered Arrays of Cobalt Nanocrystals. *Appl. Phys. Lett.* **91**, 153506-15308 (2007).
20. Yoo, S. I., Sohn, B. H., Zin, W. C., An, S. J., Yi, G. C., Self-assembled arrays of zinc oxide nanoparticles from monolayer films of diblock copolymer micelles. *Chem. Commun.* **24**, 2850-2851 (2004).
21. Moffitt, M., McMahon, L., Pessel, V., Eisenberg, A., Size Control of Nanoparticles in Semiconductor-Polymer Composites. 2. Control via Sizes of Spherical Ionic Microdomains in Styrene-Based Diblock Ionomers. *Chem. Mater.* **7**, 1185-1192 (1995).
22. Chen, H. -Y., Hou, J., Zhang, S., Liang, Y., Yang, G., Yang, Y., Yu, L., Wu, Y., Li, G., Polymer solar cells with enhanced open circuit voltage and efficiency. *Nat. Photonics* **3**, 649-653 (2009).
23. Sariciftci, N. S., Plastic photovoltaic devices. *Materials Today* **7**, 36-40 (2004).
24. Brabec, C. J., Sariciftci, N. S., Polymeric photovoltaic devices. *Materials Today* **3**, 3-6 (2000).
25. Ishii, H., Sugiyama, K., Ito, E., Seki, K., Energy Level Alignment and Interfacial Electronic Structures at Organic/Metal and Organic/Organic Interfaces. *Adv. Mater.* **11**, 605-625 (1999).

26. Hung, L. S., Tang, C. W., Mason, M. G., Enhanced electron injection in organic electroluminescence devices using an Al/LiF electrode. *Appl. Phys. Lett.* **70**, 152-154 (1997).
27. Kim, Y. E., Park, H., Kim, J. J., Enhanced quantum efficiency in polymer electroluminescence devices by inserting a tunneling barrier formed by Langmuir-Blodgett films. *Appl. Phys. Lett.* **69**, 599-601 (1996).
28. Jabbour, G. E., Kippelen, B., Armstrong, N. R., Peyghambarian, N., Aluminum based cathode structure for enhanced electron injection in electroluminescent organic devices. *Appl. Phys. Lett.* **73**, 1185-1187 (1999).
29. Du, N. Y., Tian, R. Y., Peng, J. B., Mei, Q. B., Lu, M. G., Enhanced Performance in Organic Light-Emitting Diodes with Copolymers Containing Both Tris(8-hydroxyquinoline) Aluminum and 8-Hydroxyquinoline Lithium Groups. *J. Appl. Polym. Sci.* **102**, 4404-4410 (2005).
30. Yang, X., Mo, Yang, W., Yu, G., Cao, Y., Efficient polymer light emitting diodes with metal fluoride/Al cathodes. *Appl. Phys. Lett.* **79**, 563-565 (2001).
31. Shaheen, S. E., Jabbour, G. E., Morrell, M. M., Kawabe, Y., Kippelen, B., Peyghambarian, N., Nabor, M. F., Shlaf, R., Mash, A., Armstrong, N. R., Bright blue organic light emitting diode with improved color purity using a LiF/Al cathode. *J Appl. Phys.* **84**, 2324 (1998).
32. Greczynski, G., Fahlman, M., Salaneck, W. R., An experimental study of poly(9,9-dioctyl-fluorene) and its interfaces with Li, Al, and LiF. *J. Chem. Phys.* **113**, 2407-2412 (2000).
33. Piromreun, P., Oh, H., Shen, Y., Malliaras, G. G., Scott, J. C., Brock, P. J., Role of CsF on electron injection into a conjugated polymer. *Appl. Phys. Lett.* **77**, 2403-2405 (2000).
34. Jin, Y. D., Ding, X. B., Renaert, J., Arkhipov, V. I., Borghs, G., Heremans, P. L., Auweraer, M. V., Role of LiF in polymer light-emitting diodes with LiF-modified cathodes. *Organic Electronics* **5**, 271-281 (2004).
35. Brabec, C. J., Shaheen, S. E., Winder, C., Sariciftci, N. S., Denk, P., Effect of LiF/metal electrodes on the performance of plastic solar cells. *Appl. Phys. Lett.* **80**, 1288-1290 (2002)
36. Kim, Y., Cook, S., Choulis, S. A., Nelson, J., Durrant, J. R., Bradley, D. D. C., Organic Photovoltaic Devices Based on Blends of Regioregular Poly(3-hexylthiophene) and Poly(9,9-dioctylfluorene-co-benzothiadiazole). *Chem. Mater.* **16**, 4812-4818 (2004).

37. Jin, S.-H., Naidu, B. V., Jeon, H.-S., Park, S.-M., Park, J.-S., Kim, S. C., Lee, J. W., Gal, Y.-S., Optimization of process parameters for high-efficiency polymer photovoltaic devices based on P3HT:PCBM system. *Solar Energy Materials & Solar Cells* **91**, 1187-1193 (2007).
38. Huang, C. J., Grozea, D., Turak, A., Lu, Z. H., Passivation effect of Al/LiF electrode on C₆₀ diodes. *Appl. Phys. Lett.* **86**, 033107 (2005).
39. Lee, C. H., Yu, G., Moses, D., Heeger, A. J., Srdanov, V. I., Nonlinear transient photovoltaic response in Al/C₆₀/Au devices: Control of polarity with optical bias. *Appl. Phys. Lett.* **65**, 664-666 (1994).
40. Hamed, A., Sun, Y. Y., Tao, Y. K., Meng, R. L., Hor, P. H., Effects of oxygen and illumination on the in situ conductivity of C₆₀ thin films. *Phys. Rev. B* **47**, 10873-10880 (1993).
41. Grozea, D., Turak, A., Feng, X. D., Lu, Z. H., Johnson, D., Wood, R., Chemical structure of Al/LiF/Alq interfaces in organic light-emitting diodes. *Appl. Phys. Lett.* **81**, 3173-3175 (2002).
42. Krebs, F. C., Fabrication and processing of polymer solar cells: A review of printing and coating techniques. *Solar Energy Materials and Solar Cells* **93**, 394-412 (2009).
43. Li, G., Shrotriya, V., Huang, J., Yao, Y., Moriarty, T., Emery, K., Yang, Y., High-efficiency solution processable polymer photovoltaic cells by self-organization of polymer blends. *Nature Mater.* **4**, 864-868 (2005).
44. Whitesides, G. M., The 'right' size in nanobiotechnology. *Nat. Biotechnology* **21**, 1161-1165 (2003).
45. Maier, S. A., Brongersma, M. L., Kik, P. G., Meltzer, S., Requciha, A. A. G., Atwater, H. A., Plasmonics – A Route to Nanoscale Optical Devices. *Adv. Mater.* **13**, 1501-1505 (2001).
46. Kim, E., Xia, Y. N., Whitesides, G. M., Micromolding in Capillaries: Applications in Materials Science. *J. Am. Chem. Soc.* **118**, 5722-5731 (1996).
47. Xia, Y., Whitesides, G. M., Soft Lithography. *Angew. Chem., Int. Ed.* **37**, 550-575 (1998).
48. Chou, S. Y., Krauss, P. R., Renstrom, P. J., Imprint of sub-25 nm vias and trenches in polymers. *Appl. Phys. Lett.* **67**, 3114-3116 (1995).
49. Gates, B. D., Xu, Q., Stewart, M., Ryan, D., Willson, C. G., Whitesides, G. M., New Approaches to Nanofabrication: Molding, Printing, and Other Techniques. *Chem. Rev.* **105**, 1171-1196 (2005).

50. Austin, M. D., Ge, H., Li, W. W. M., Yu, Z., Wasserman, D., Lyon, S. A., Chou, S. Y., Fabrication of 5 nm linewidth and 14 nm pitch features by nanoimprint lithography. *Appl. Phys. Lett.* **84**, 5299-5301 (2004).
51. Geissler, M., Xia, Y., Patterning: Principles and Some New Developments. *Adv. Mater.* **16**, 1249-1269 (2004).
52. D. W. V. Krevelen, *Properties of Polymers*, Elsevier, Amsterdam, 1997.
53. Eddington, D. T., Puccinelli, J. P., Beebe, D. J., Thermal aging and reduced hydrophobic recovery of polydimethylsiloxane. *Sensors and Actuators B* **114**, 170-172 (2006).
54. Rogers, J. A., Paul, K. E., Whitesides, G. M., Quantifying distortions in soft lithography. *J. Vac. Sci. Technol. B.* **16**, 88-97 (1998).
55. Odom, T. W., Love, Wolfe, D. B., Paul, K. E., Whitesides, G. M., Improved Pattern Transfer in Soft Lithography Using Composite Stamps. *Langmuir* **18**, 5314-5320 (2002).
56. Schmid, H., Michel, B., Siloxane Polymers for High-Resolution, High-Accuracy Soft Lithography. *Macromolecules* **33**, 3042-3049 (2000).
57. Kim, J. K., Park, J. W., Yang, H., Choi, M., Choi, J. H., Suh, K. Y., Low-pressure detachment nanolithography. *Nanotechnology* **17**, 940-946 (2006).
58. Goh, C., Coakley, K. M., McGehee, M. D., Nanostructuring Titania by Embossing with Polymer Molds Made from Anodic Alumina Templates. *Nano Lett.* **5**, 1545-1549 (2005).
59. Hur, S.-H., Khang, D.-Y., Kocabas, C., Rogers, J. A., Nanotransfer printing by use of noncovalent surface forces: Applications to thin-film transistors that use single-walled carbon nanotube networks and semiconducting polymers. *Appl. Phys. Lett.* **85**, 5730-5732 (2004).
60. Meitl, M. A., Zhu, Z.-T., Kumar, V., Lee, K. J., Feng, X., Huang, Y. Y., Adesida, I., Nuzzo, R. G., Rogers, J. A., Transfer printing by kinetic control of adhesion to an elastomeric stamp. *Nature Mater.* **5**, 33-38 (2006).
61. Loo, Y.-L., Willett, R. L., Baldwin, K. W., Rogers, J. A., Interfacial Chemistries for Nanoscale Transfer Printing. *J. Am. Chem. Soc.* **124**, 7654-7655 (2002).
62. Loo, Y.-L., Hsu, J. W. P., Willet, R. L., Baldwin, K. W., West, K. W., Rogers, J. A., High-resolution transfer printing on GaAs surfaces using alkane dithiol monolayers. *J. Vac. Sci. Technol. B* **20**, 2853-2856 (2002).

63. Matsui, S., Igaku, Y., Ishigaki, H., Fujita, J., Ishida, M., Ochiai, Y., Namatsu, H., Komuro, M., Room-temperature nanoimprint and nanotransfer printing using hydrogen silsequioxane. *J. Vac. Sci. Technol. B* **21**, 688-692 (2003).
64. Guo, Q., Teng, X., Yang, H., Overpressure Contact Printing. *Nano Lett.* **4**, 1657-1662 (2004).
65. Maury, P. A., Escalante, M., Reinhoudt, D. N., Huskens, J., Directed Assembly of Nanoparticles onto Polymer-Imprinted or Chemically Patterned Templates Fabricated by Nanoimprint Lithography. *Adv. Mater* **17**, 2718-2723 (2005).
66. Mizuno, H., Buriak, J. M., Catalytic Stamp Lithography for Sub-100 nm Patterning of Organic Monolayers. *J. Am. Chem. Soc.* **130**, 17656-17657 (2008).
67. Akbulut, O., Jung, J.-M., Bennett, R. D., Hu, Y., Jung, H.-T., Cohen, R. E., Mayes, A. M., Stellacci, F., Application of Supramolecular Nanostamping to the Replication of DNA Nanoarrays. *Nano Lett.* **7**, 3493-3498 (2007).
68. Jacobs, H. O., Whitesides, G. M., Submicrometer Patterning of Charge in Thin-Film Electrets. *Science* **291**, 1763-1766 (2001).
69. Jacobs, H. O. Champell, S. A., Steward, M. G., Approaching Nanoxerography: The Use of Electrostatic Forces to Position Nanoparticles with 100 nm Scale Resolution. *Adv. Mater.* **14**, 1553-1557 (2002).
70. Barry, C. R., Steward, M. G., Lwin, N. Z., Jacobs, H. O., Printing nanoparticles from the liquid and gas phases using nanoxerography. *Nanotechnology* **14**, 1057-1063 (2003).
71. Barry, C. R., Gu, J., Jacobs, H. O., Charging Process and Coulomb-Force –Directed Printing of Nanoparticles with Sub-100 nm Lateral Resolution. *Nano Lett.* **5**, 2078-2084 (2005).
72. Kim, H., Kim, J., Yang, H., Suh, J., Kim, T., Han, B., Kim, S., Kim, D. S., Pikhitsa, P. V., Choi, M., Parallel patterning of nanoparticles via electrodynamic focusing of charged aerosols. *Nat. Nanotech.* **1**, 117-121 (2006).
73. Stewart, M. E., Motala, M. J., Yao, J., Thompson, L. B., Nuzzo, R. G., Unconventional methods for forming nanopatterns. *Proc. IMechE* **220**, 81-138 (2007).
74. Mbenkum, B. N., Schneider, A. S., Schütz, G., Xu, C., Richter, G., van Aken, P. A., Majer, G., Spatz, J. P., Low-Temperature Growth of Silicon Nanotubes and Nanowires on Amorphous Substrates. *ACS Nano* **4**, 1805-1812 (2010).

75. Mbenkum, B. N., Diaz-Ortiz, A., Gu, L., van Aken, P. A., Schütz, G., Expanding Micelle Nanolithography to the Self-Assembly of Multicomponent Core-Shell Nanoparticles. *J. Am. Chem. Soc.* **132**, 10671-10673 (2010).
76. Momozono, S., Nakamura, K., Kyogoku, K., Theoretical model for adhesive friction between elastomers and rough solid surfaces. *J. Chem. Phys.*, **132**, 114105 (2010)

CHAPTER 2. EXPERIMENTAL

2.1 Materials

Polystyrene block poly(2-vinylpyridine) (PS-*b*-P2VP) polymers were purchased from Polymer Source Inc. Chemical structure of the diblock copolymer is given in Figure 2. 1. Polymers with two different molecular weights were used: (i) PS(48,500)-*b*-P2VP(70,000) (PDI:1.08) (ii) PS(75,000)-*b*-P2VP(66,500) (PDI: 1.09). Poly (methyl methacrylate) (PMMA) was purchased in chlorobenzene with 950 K molecular weight and 2% concentration from MicroChem, Newton, Massachusetts. Lithium hydroxide (non hydrate) (Merck), hydrogen fluoride (40%) (Merck), toluene (99.9 %) (Merck) were used as received. Lithium acetate (LiAc) and ammonium fluoride (NH₄F) was purchased from Merck and used as received. Sylgard-184 PDMS curing kit was purchased from Dow Corning. Indium tin oxide (ITO) substrates (1.5 cm × 1.5 cm, 30 □/square) coated on glass support was purchased from TFD Inc.

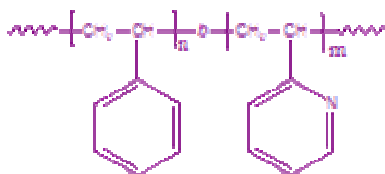


Figure 2. 1: Chemical structure of PS-*b*-P2VP copolymers

2.2 Lithium Fluoride Formation

2.2.1 Lithium Fluoride Synthesis in Toluene

- 0.132 g LiOH was poured in 20 ml toluene and kept stirring.
- To obtain 1:1 molar ratio, 0.237 mL HF (40%) was added to start reaction.
- After 2 hours of stirring, the bulk salt obtained in the bottom of the plastic beaker was filtered with a filter paper and dried in the ambient environment before SEM and XPS characterization.

2.2.2 Lithium Fluoride Nanoparticle Synthesis in Polystyrene block poly(2-vinyl pyridine) copolymers (Plan A and Plan B reactions)

The following reaction amounts are most frequently used values in the experiments. For some experiments less or more amount were synthesized by keeping stoichiometric ratio. To prepare the polystyrene-*block*-poly 2-vinylpyridine (PS-*b*-P2VP) reverse micelle reactor vessels:

- 15 mg of PS(48,500)-*b*-P2VP(70,000) was dissolved in 5 ml of toluene under vigorous stirring for 24 hours.
- 1.2 mg of LiOH was added to the micelle solution under vigorous stirring for at least 2 days. In order to obtain bigger particles LiOH loading step was extended to 4 – 5 days.
- To remove the undissolved LiOH, the solution was centrifuged at 4500 rpm for 40 minutes.
- Upon centrifugation, undissolved salt was precipitated to bottom of the falcon tube. The transparent solution remained on top (supernatant) was taken with a micropipette for further reaction
- To obtain the nominal 1:1 molar stoichiometry for LiF formation, 2.8 μ l of hydrofluoric acid (technical grade 40%) was added to the LiOH loaded micellar solution under continuous stirring.
- Following the HF addition, solution was kept stirring for 24 hours at least. Without any further processes solutions were used.

Due to the complications and difficulties of characterization of LiF nanoparticles, at certain point, an additional reaction scheme was planned. This ‘Plan B’ synthesis of LiF was from the reaction of lithium acetate (LiAc) + ammonium fluoride (NH₄F):

- 15 mg of PS(48,500)-*b*-P2VP(70,000) was dissolved in 5 ml of toluene under vigorous stirring for 24 hours.
- 1 mg of LiAc was added to solution. LiAc was a big salt. However, it was observed that big particles were completely dissolved and solution became blurry.

- After 36 hours of mixing super saturation was observed. Prior to NH_4F addition, solution was centrifuged for 40 minutes at 4500 rpm. After centrifuge, the flake-like particles were precipitated and supernatant was taken for further reaction.
- For 1-1 molar ratio, the calculated amount of NH_4F is ~ 0.5 mg. So, 0.6 mg NH_4F was added to M+LiAc solution and solution was stirred for 1 day.
- After 24 hours, some precipitates were observed which was probably as the result of super saturation and products other than LiF. Therefore, prior to substrate coating step, solution was centrifuged at 4500 rpm for 40 minutes.

2.2.3 Understanding aging effect

Two different particle morphologies observed and the reason appeared to be reaction time after HF addition. For this purpose effect of HF on PS was observed. 30 mg PS homopolymer (M_w : 48,000) was dissolved in 10 ml toluene. Solution was divided in 2 ml parts. For these, HF(%1), HF (%5) and HF(%40) was added and solutions were kept stirred. Molar amounts of HF were adjusted to the amount used for LiF synthesis inside micelle. For FTIR analysis, thick films on glass were prepared by drop casting.

2.3 Post Processing After Synthesis

2.3.1 Coating on substrates

The substrates used in this project are glass, silicon, silicon nitride (Si_3N_4), ITO and magnesium oxide (MgO). Prior to usage, all substrates were cleaned in an ultrasonic bath of 15 minutes each of acetone, followed by ethanol, and then rinsed with de-ionized water. After cleaning with solvents, all substrates were dried with a pure N_2 stream. In the absence of N_2 stream overnight furnace heating was applied to substrates at 60°C .

MgO (single crystal) substrates were annealed before coating with the micelle solution. The substrates were brought to 1000°C with $20^\circ\text{C}/\text{min}$ heating rate and kept there for 1 hour. Then they were cooled again with rate of $\sim 20^\circ\text{C}/\text{min}$. The coating procedure was completed as the substrates were taken from the furnace.

In most of the cases spin coating was used. The solution of loaded micelles (12-13 μL) was spin coated on substrates by spin-parameters of 2000 rpm for 40 seconds, for 3 mg/ml of micelle solution. However, it was observed that better hexagonal coating can be achieved for lower concentrations (between 2 – 2.5 mg/ml). In order to create more coverage on the surface, lower spin rates with higher concentration were used. Or, spin coating with conventional parameters were repeated following with O_2 plasma.

2.3.2 Plasma Etching

To remove the polymeric micelles and to reveal the LiF particles plasma etching was performed. In the initial experiments both O_2 plasma and H_2 plasma was performed with PVA Tepla America Inc. Etching conditions for O_2 plasma is 150W power, 0.1 mbar O_2 gas pressure for 45 min. For H_2 plasma 150W power, 0.4 mbar H_2 gas pressure for 45 min. For the latest experiments performed in SU, Harrick Plasma equipment was used for O_2 plasma with the parameters of Hi-power (29.6W), 1 Torr O_2 gas pressure for 30 min.

2.4 Device Formation in Inverted Structure With Direct Coating of Nanoparticles

The experimental procedure for LiF coating of Al:

- 1) Getting Al samples from big chamber to transfer chamber. Close the connection between two chambers and unplug the transfer chamber.
- 2) Carry the transfer chamber to glove box and open the N_2 gas flow. Wait ~1 hour, the humidity inside the glove box was measured as % 0.4
- 3) Open the transfer chamber in glove box and take samples to desiccator. Start pumping. After 30 minutes take the transfer chamber and place solution, samples inside the glove box. Wait 1 hour to obtain humidity below % 0.4.
- 4) Organize everything in glove box, position everything for easy coating

- 5) Coat samples with M+LiOH+HF solution that is 1.66 mg/ml (diluted from 3 mg/ml) (See **Hata! Başvuru kaynağı bulunamadı.** During coating use 30 V that corresponds to 30 mm/min speed of dipping and pulling.
 - 6) After coating the samples, place them into petri dish
 - 7) Place samples that are in petri dish to desiccator and vacuum the desiccator.
 - 8) After 45 minutes bring samples to plasma with desiccator.
 - 9) Place petri dish in plasma while flushing the environment with argon (Ar).
Because the bottom petri dish was too big for metal protector in chamber, we had to spend more time than anticipated (possible air exposure)
 - 10) After doing each move, we evacuated the chamber and apply vacuum.
 - 11) Then vent with Ar that is heavier than O₂
 - 12) Open petri dish, transfer them to smaller
 - 13) Etch the samples with H₂ plasma 0.4 mbar, 150 W, 45 min.
 - 14) Vent the chamber with argon
 - 15) Place the top petri dish in the chamber and vacuum, then vent with argon. Then open the chamber (while flushing with argon) and close the petri dish.
 - 16) Place the petri dish into the desiccator that is just near to plasma system.
 - 17) Apply vacuum to desiccator, wait 10-15 min.
 - 18) Bring the desiccator to glove box and start N₂ flow. Wait ~1 hour until humidity decreases to % 0.2.
 - 19) Transfer samples from desiccator to Transfer chamber.
 - 20) Bring transfer chamber out carefully and mount it to big chamber.
- (Everything took ~11 hours and growth of films in vacuum was performed by Ayşe Turak, MPI)

2.5 Effect of Direct Coating of Particles on Organic Surfaces

In order to understand the effect of direct coating of nanoparticles on organic layers used in the photovoltaics, initially organic films were exposed to toluene, by dropping 15 µl toluene, and spin coating at 2000 rpm for 40 seconds. Afterwards O₂ plasma with 0.1 mbar

gas pressure, 150 W power, for 45 min was applied. Before and after each process, samples were characterized with AFM.

2.6 Nanotransfer printing Experiments

2.6.1 PDMS Curing

The outline of the PDMS curing can be found in literature. However, the details and tricks can not be found in the literature. Therefore, a detailed process flow of PDMS curing was retrieved from a webpage ¹.

Weighing

- Sylgard 184 is a two-component heat-curing system, i.e. it consist of a base part and a curing agent part.
- A common plastic cup was taken and filled with one part curing agent and ten parts of base (by weight) 10:1 (m/m) ratio
- It is better to start with the curing agent, since it is harder to pour the right amount of it. 7-10 g material will be sufficient for covering one template, e.g. 0.7 g curing agent and 7 g base.

Mixing

- A plastic spoon was used to mix the base and the curing agent for at least a few minutes, depending on the amount of material. Upon mixing, a lot of air trapped in the solution

Degassing

- After the mixing the silicone mixture will be full of air bubbles and needs degassing. This was done in a desiccator using vacuum. During the degassing the silicone expands and bubbles disappear by small explosion. When the silicone is completely clear and transparent it is finished. (20-30 min)

Dispensing

- Dispensing the silicone on to the template can be a bit tricky, because it is important to avoid trapping air in the process. Sylgard 184 has relatively low viscosity, so the flow is no problem. Dispensing the material at the center of the template from a low altitude minimizes the risk of trapped air. Template should be kept horizontal during dispensing.

Spreading

- The spreading on a flat substrate can be achieved by tilting it at a low angle. By tilting it in different directions it is possible to cover the whole template by silicone.

Curing

- Sylgard 184 is heat curing. It is curable from less than room temperature to over 150°C. Sylgard 184 also has temperature dependent shrinkage as seen in Figure 2. 2. Curing in 140°C (~15 min) will make the stamp shrink almost exactly 3 %.

Peel-off

- The final step is to peel off the stamp from the template. It is possible to use a sharp and curved pair of tweezers to do this. Start by releasing all borders and then continue at a low speed in a direction parallel to most structures and peel off the remaining parts. Store the stamp in a flat plastic container with the pattern facing upwards, i.e. away from the container.

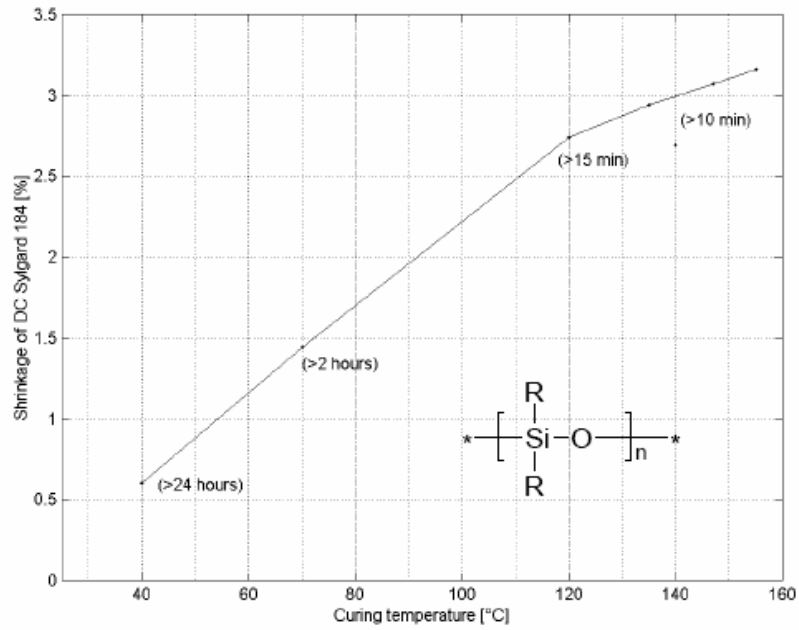


Figure 2. 2: Shrinkage graph of Sylgard 184 PDMS depending on the curing temperature (Taken from Ref 1 without permission)

2.6.2 PDMS Pressing

PDMS pressing experiments were performed with different loads. In certain cases a gentle force was applied by putting 50-100 mg weight over the PDMS and the substrate. However, most pressing experiments were carried with the set-up shown in Figure 2. 3. The press was manufactured in the workshop of MPI.



Figure 2. 3: Press set-up used for PDMS pressing and other purposes.

2.6.3 PMMA Cooling

Nanotransfer printing experiments by use of PMMA was generally performed as following:

- Clean silicon substrate was spin coated with thin layer of PMMA in chlorobenzene. Spin coating parameters as 5000 rpm for 1 min resulted in 100 nm thick films.
- PMMA coated silicon substrate and LiF nanoparticle coated glass substrate was brought together with press. Due to the fragility of standard optic microscope borosilicate glass slide (thin one), sometimes paper clips were also used.
- Substrates in close contact were heated to higher temperatures (~ 120 °C) than glass transition temperature (T_g) of PMMA which is around ~ 100 °C.

2.6.4 Electrostatic Charging of PMMA

Electrostatic charging of PMMA experiments were done as described in the work of Jacobs et al. which was also discussed in section 1.3². Apart from the same procedure

described in the work, direct transition of particles was tried by coating the gold surface of the stamp with particles and applying O₂ plasma. Afterwards, bias was applied between stamp which has particles on it, and PMMA coated silicon in 20 – 40 V range.

2.6.5 Adhesive Tape Experiments

There are two kinds of adhesive tape experiments. The first one is rather robust and simple: sticking an adhesive tape (scotch tape, REVALPHA tape) on top of a glass substrate, which is coated with LiF nanoparticles beforehand. Pressure was applied with the back-side of Teflon tweezers for 5–10 minutes, and the tape remained in contact with the glass substrate for an additional 15-20 minutes to complete 30 minutes of experiment time.

The second type of adhesive tape experiments rely on REVALPHA tape. REVALPHA is a unique thermal release tape that behaves like normal adhesive tape at room temperature but can be easily peeled off by simply heating when you want to peel the tape off. The details of this experiment are still under study. However, the planned process-flow schematic is given in section 3.5.4.

2.7 Characterization

2.7.1 Dynamic Light Scattering (DLS)

DLS experiments were carried out by Zetasizer Nano, Malvern Instruments Ltd. Because the micellar solutions were prepared in a toluene environment, quartz cells were employed rather than the standard PS cells. The detector was fixed at the scattering angle of 173° (the Noninvasive Backscattered optical detection technology maximizes the sample volume analyzed, enabling study of a broader range of particle sizes and concentrations), and a He-Ne laser was used as a light source with $\lambda = 632$ nm. Characterization was performed at 23 °C (room temperature) waiting for 3 minutes for temperature equilibration. For optical parameters, PS was taken account as being the corona of micelle. For viscosity, rather than the viscosity of toluene (0.54 cP), the viscosity of the micellar solution (0.66 cP) was used because it directly affects the final result.

2.7.2 Scanning electron microscope (SEM)

Scanning electron micrographs were taken by a Zeiss field emission scanning electron microscope (FE-SEM) (Ultra 55) operated at an acceleration voltage of 2-5 kV. For nonconductive surfaces, carbon coating was applied.

2.7.3 Atomic force microscope (AFM)

Atomic force microscopy measurements were done in 2 different AFMs. The one at MPI is in air using a Veeco Digital Instruments CP-II SPM system in tapping mode. The non-contact silicon tips were MPP-11123-10 (Veeco) with a resonance frequency of 285-327 kHz, and a force constant of 20-80 N/m. AFM characterization in SU was performed using a Nanoscope III Atomic Force Microscope (Digital Instruments, Santa Barbara, CA USA) using the tapping mode with single-beam silicon cantilevers (spring constant between 30 – 40 N/m) The AFM images were processed with the free software WSxM (NanoTec)³.

2.7.4 Transmission electron microscope (TEM)

Electron diffraction experiments were performed using a JEOL 2010F transmission electron microscope (TEM) operated at 200 keV, while energy dispersive x-ray spectroscopy (EDX) analysis was carried out on the same instrument in scanning transmission electron microscope (STEM) mode. TEM sample preparation was done in two ways with Cu grids. In the first method, Cu grid was dipped in micelle solution and take back after 2 s waiting time. Then it is placed on top of a filter paper to remove excess solution from the grid. In the second method, a very tiny drop (3-4 μL) of micelle solution was dropped on Cu grid which stands on filter paper. TEM characterization in this study is mostly performed by Clevea Ow-Yang.

2.7.5 X-ray photoelectron spectroscopy (XPS)

X-ray photoelectron spectroscopy was performed on a ThetaProbe (Thermo VG Scientific), equipped with a monochromatic Al K α source, which can be focused down to a spot size of 15 μm . XPS measurements were performed at MPI.

2.7.6 X-ray diffraction (XRD)

X-ray diffraction measurements were performed in a Philips (now Panalytical) X'Pert Pro Diffractometer, parallel beam realized by an X-ray lens in the primary beam and parallel-plate collimator in the diffracted beam, beam size set to 4 mm x 4 mm by crossed slits, Cu-K α radiation from a sealed X-ray tube (45 kV, 40 mA). XRD measurements were performed at MPI.

2.7.7 Kelvin probe work function measurements

Kelvin probe (KP) measurements were performed by Prof. I. D Baikie of KP Technologies, KP Technology Ltd. Analysis type was absolute scan which is a scan of approximate dimensions 6 x 6 cm conducted with a 2 mm diameter Kelvin probe tip. The tip Work Function (WF) has been determined with reference to a pristine gold surface and we assume the gold surface is 5.10 eV.

The scans have been performed at a constant tip to sample spacing, termed tracking, so that the measurements made with the same tip on different samples can be compared correctly. Average work function and standard deviation about the mean was reported. The data set have been nearest-neighbor filtered.

Chapter 2 References

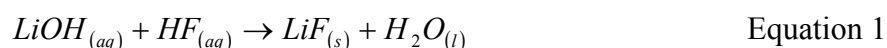
1. Krog, M. (2000). Soft Lithography for Dummies. Retrived from Linköping University website: http://issuu.com/publishgold/docs/soft_lithography_for_dummies
2. Jacobs, H. O., Whitesides, G. M., Submicrometer Patterning of Charge in Thin-Film Electrets. *Science* **291**, 1763-1766 (2001).
3. Horcas, I., Fernandez, R., Gomez-Rodriguez, J. M., Colchero, J., Gomez-Herrero, J., Baro, A. M., WSXM: A software for scanning probe microscopy and a tool for nanotechnology. *Rev. Sci. Instrum.* **78**, 013705-013712 (2007).

CHAPTER 3. RESULTS AND DISCUSSION

3.1 Lithium Fluoride Formation

3.1.1 Lithium Fluoride Synthesis in Toluene

The formation of fine LiF nano-powders in an aqueous environment with a simple reaction of LiOH and HF was previously demonstrated by Sarraf-Mamoory and coworkers¹. The reaction in this scheme is described in Eqn 1:



To confirm that the reaction would occur without the presence of the micelles, LiOH was reacted with HF directly in toluene. The formed salt was analyzed with SEM and XPS (results is given in Figure 3. 1). Observation of cubic particles by SEM is indication of LiF formation because cubic structure is resulted from rocksalt crystal structure of LiF. In addition, XPS validate the formation of LiF crystallites from solution with the 1s Li peak at 55 eV and 1s F peak at 685 eV².

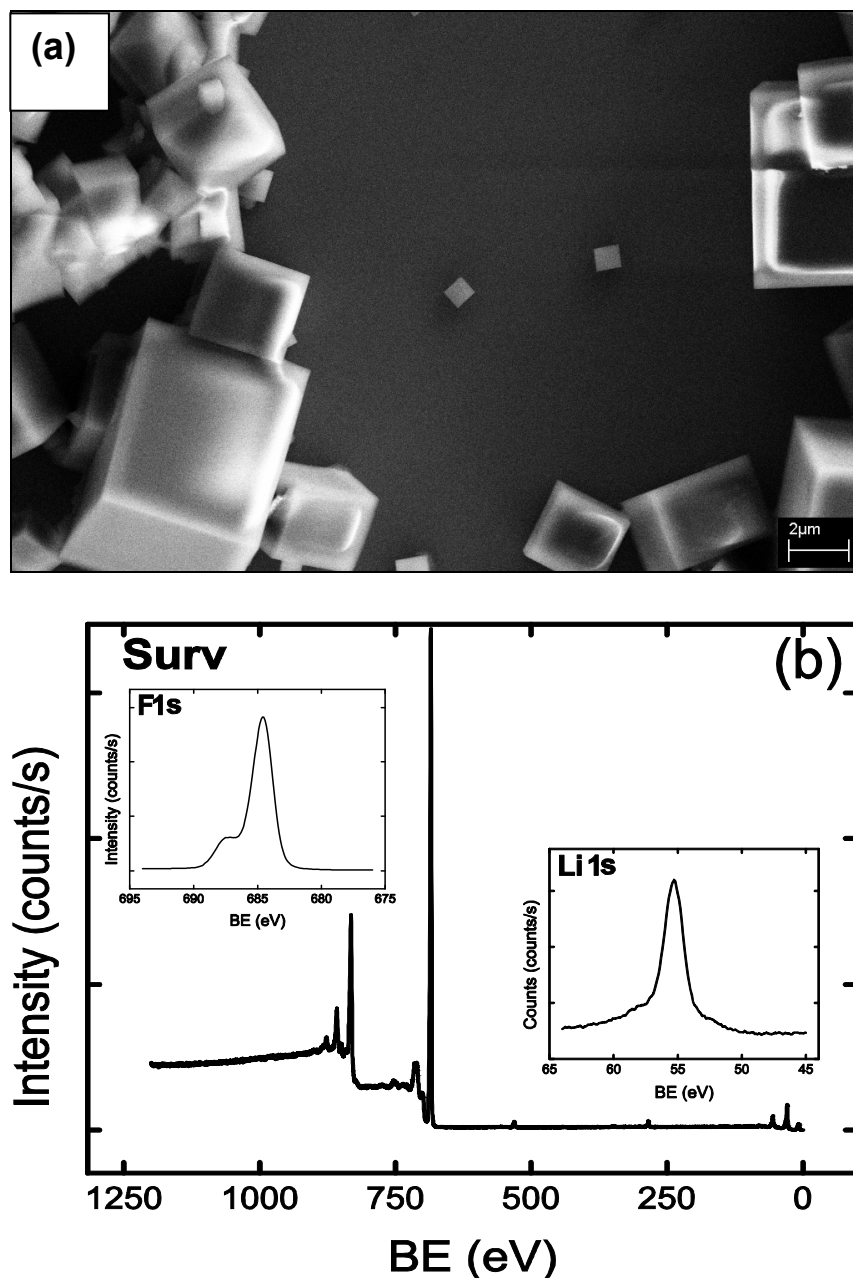


Figure 3. 1: (a) SEM image and (b) XPS spectra of LiF crystals produced from direct reaction of LiOH and HF in toluene.

3.1.2 Lithium Fluoride Nanoparticle Synthesis in Polystyrene block poly(2-vinyl pyridine) copolymers

The conventional nanoparticle formation in diblock copolymer micelles are carried by initial loading of the metal salt and coordination of metal with 2VP group of the micelle. For this purpose, the metal candidate should have acidic or basic property so that it can

leave its bonded groups easily. So our selection of LiOH seems to be proper metal salt that can precipitate inside the micelle core that bears 2VP groups. To prove this concept, initially LiOH was added to PS(75,000)-*b*-P2VP(66,500) micelle solution and kept stirring for 1 week. However, the big salt LiOH at the bottom of vial had not disappeared. In addition, the solution did not become blurry which is a good indication for salt dissolution in micelle solution. To solve the solubility problem, an asymmetric polymer, PS(48,500)-*b*-P2VP(70,000), with longer P2VP (polar) block was tried. The dissolution of salt was observed with the asymmetric polymer and this polymer was used in all the experiments. Upon LiOH loading after 3-4 days, undissolved LiOH was removed by centrifuge and spin coated on a silicon substrate. Polymeric micelles were removed by O₂ plasma. In the given SEM image below (Figure 3. 2) few nanometer sized particles can be observed. Particles were not arranged hexagonally and the size distribution does not seem very uniform. Indeed, this is a predicted result because before reduction, the metal salt is mostly found as incorporated to micelle core as small salt particles that are not unified yet³. Especially very close particles are indicative for several nano-salt formations in a single micelle core. Moreover, in order to reveal LiOH loading to micelle DLS measurement was performed. As shown in Figure 3. 3 average diameter of PS-*b*-P2VP increased from 16.7 nm to 67 nm which is a good indication for salt loading⁴. Thus, presented result is a good proof that LiOH can be used as Li⁺ source for the LiF formation.

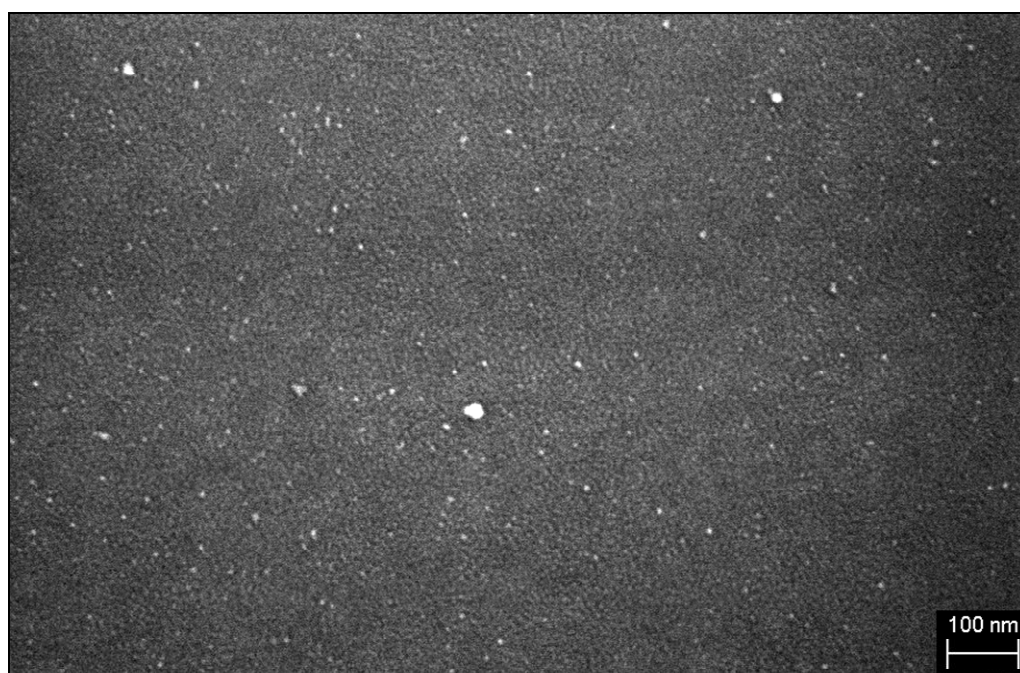


Figure 3. 2: SEM image of PS-P2VP micelles loaded with LiOH and etched with O₂ plasma

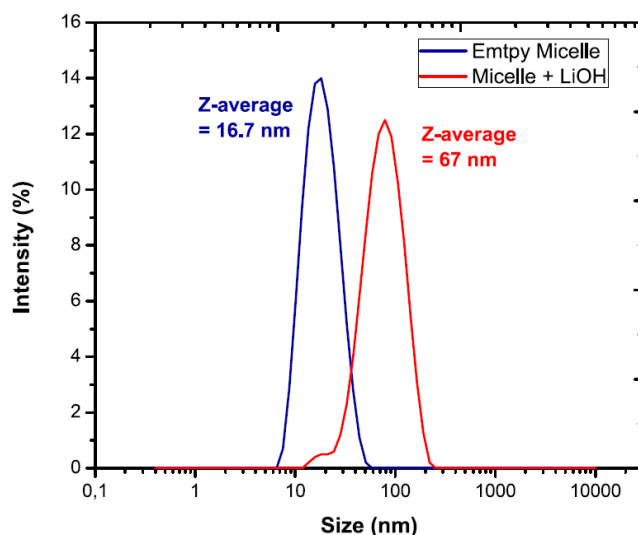


Figure 3. 3: Dynamic light scattering result for empty and LiOH loaded micelles, average size increased from 16.7 nm to 67 nm upon loading of LiOH.

After ensuring the loading of LiOH salt into micelle core, the following reactant, HF, was added to micelles. This reaction was always performed after a centrifuge step. This was important because in micellar solution, there can always be some unloaded salt present outside the micelle and formation of HF particles outside the micelles may not be desired. After HF addition, solutions were left for stirring at least 20 hours and after spin coating on a substrate, samples were etched with either O₂ or H₂ plasma. It was found out that the plasma conditions are critical for the removal of all polymeric part. In the case of less power/time usage, there is always possibility of residual polymers on particles as in Figure 3. 4b. Along with other experiments plasma conditions were optimized as following¹: - for O₂ plasma, 0.1 mbar, 150 W, 45 minutes; for H₂ plasma: 0.4 mbar, 150 W, 75 minutes. In addition to plasma systems, concentration of micelle solution was adjusted after this experiment. In this experiment, concentration of the micelle solution was 5 mg/ml (PS-*b*-P2VP to toluene). For this particular molecular weight polymer, PS(48,500)-*b*-P2VP(70,000), this amount was found high because as seen from the SEM images with this concentration, micelles tend to induce phase transformation. After this experiment, concentration of micellar solution was decreased to 3 mg/ml.

¹ These parameters are for PVA Telpa plasma system, for each system these parameters can be different.

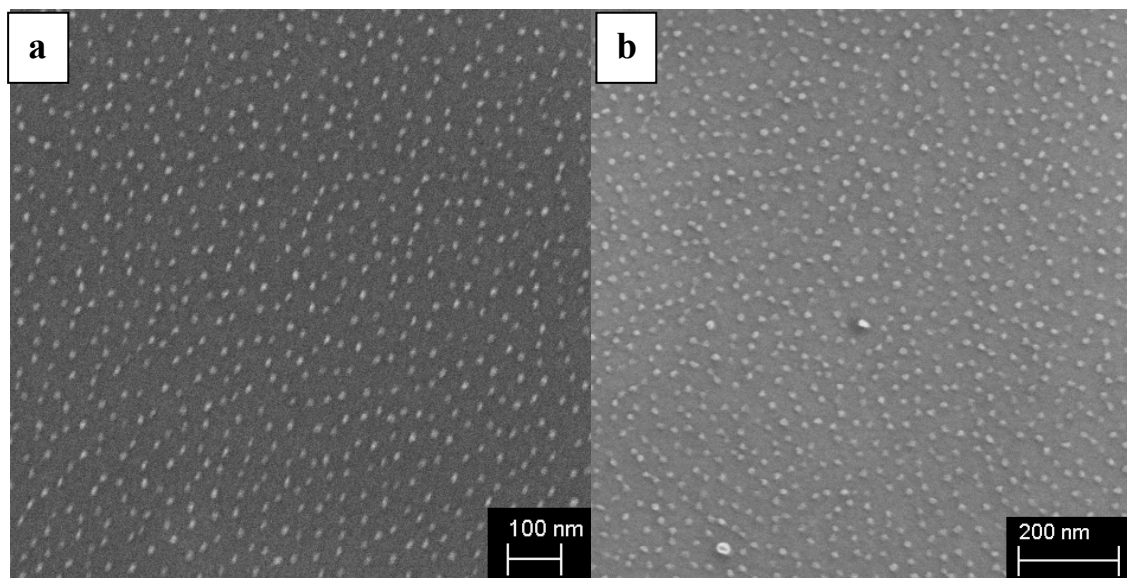


Figure 3. 4: LiOH and HF loaded micelles etched with (a) O₂ plasma and (b)H₂ plasma

In certain cases, some problems were encountered during the synthesis of LiF nanoparticles. First of all there was a stability problem with time, which is seldom observed with other diblock copolymer micelle systems. On the other hand, HF can fluorinate the polystyrene part of micelle, which may give rise to the carbon-fluorine peak in the XPS spectra². This was especially notable, when the solutions were held for longer than 2-3 days, and one could see the appearance of white rings around the micelles in the SEM images. In order to monitor the stability, further stirring was continued for 15 days. The ring pattern around micelles had increased, and this is shown in the Figure 3. 5 below.

² Obtained in early times, however, after realization of contamination in the plasma system, XPS results belong to LiF nanoparticles derived from PS-*b*-P2VP was discarded.

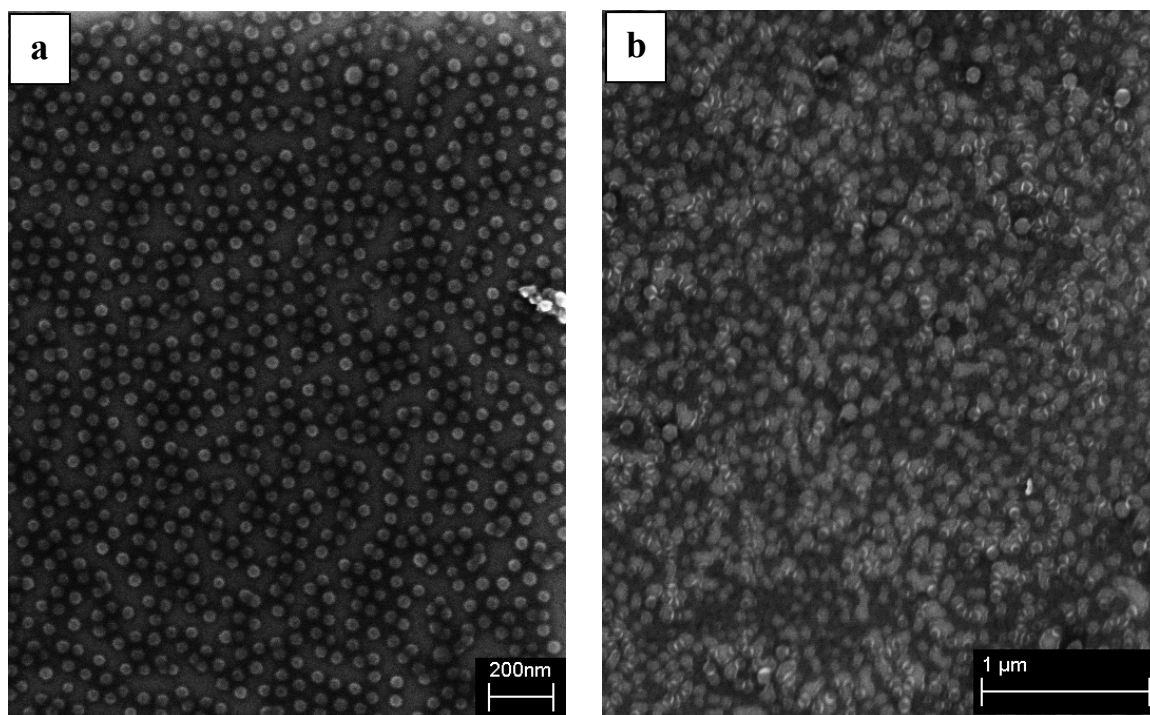


Figure 3. 5: SEM images of LiOH and HF loaded micelles after 3 days of HF addition (a) and after 15 days of HF addition (b)

When extensively stirred micelles were etched with plasma, core-shell like particles was obtained (Figure 3. 6). The particle distribution is not very hexagonal, and the size of particles is around 18 nm. Having core-shell particles could have been attributed to an O₂ plasma, but for the LiF crystals obtained with direct reaction of LiOH and HF in toluene, O₂ plasma treatment was performed, and it was observed from the SEM images that the cubic structure of LiF crystals had not changed with such treatment. Therefore, it is reasonable to attribute this ring formation in micelle and the post-etch core-shell like particles to fluorination of styrene groups and the formation of some variant of fluorinated carbide. When the stirring of solution is limited to 15 hours after the HF addition, single colored particles (not resemble core-shell particles) were obtained and this is illustrated in Hata! Başvuru kaynağı bulunamadı.. From the SEM image, a hexagonal ordering between particles can be seen, and the distance between each particle is around 60 nm, while the particle size is around 10 nm. Hence, it is clear that for this system, uniform particles are formed in the core of each micelle. Therefore, even if there is a reaction of HF with styrene part, the formation of some fluorinated compound would occur, given sufficient time.

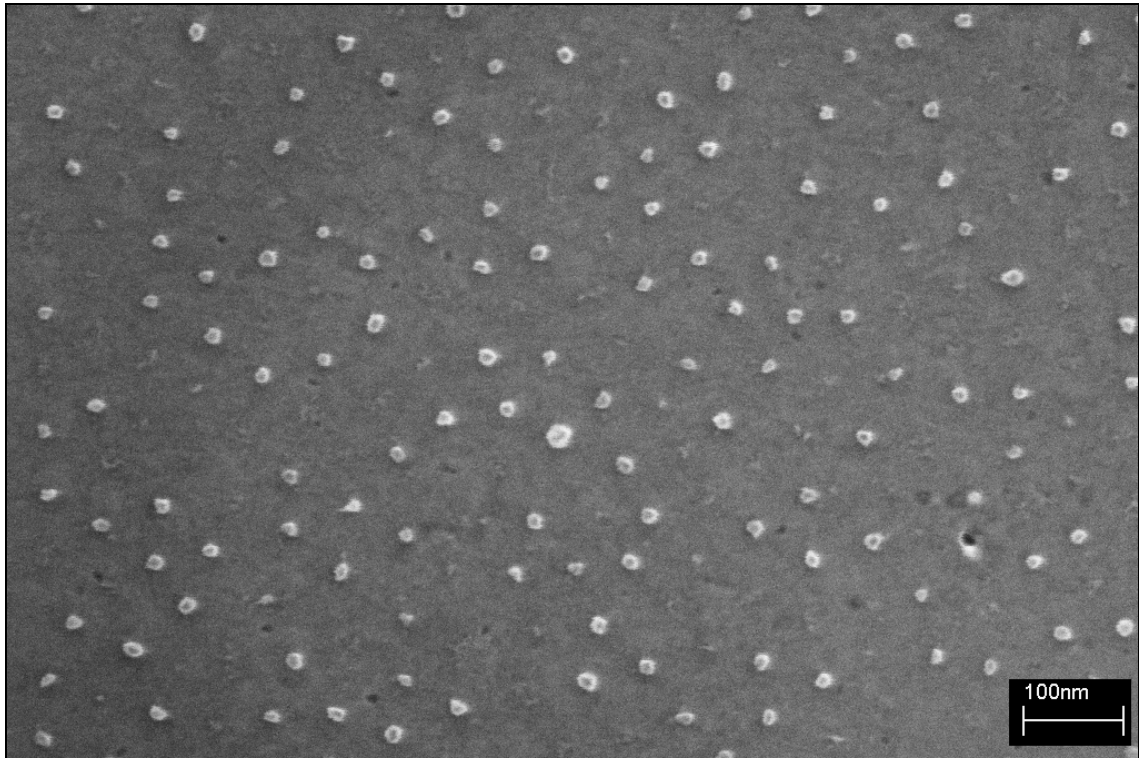


Figure 3. 6: SEM image of LiOH and HF loaded micelles etched with O₂ plasma after 3 days of HF addition



Figure 3. 7: SEM image of LiOH and HF loaded micelles, spin coated on Si₃N₄ substrate and etched with O₂ plasma after 15 hours of HF addition. FFT is given on the upper right corner

To understand the direct effect of HF to PS-*b*-P2VP reverse micelles, only the HF loading of micelles were performed. Two experiments with different HF loading (stirring) time were performed, and the SEM results can be seen below. In **Hata! Başvuru kaynağı bulunamadı.**a, HF-loaded micelles etched after 3 days of stirring are shown, and here the formation of small particles with non-uniform distribution can be observed. The distance between particles vary and is not limited with center-to-center distance of micelles (60 nm), which was previously shown in Figure 3. 7. This evidence can be indicative of a reaction between HF and PS-*b*-P2VP, and probably this reaction was on the surface (or any non-core place) of the micelles. On the other hand, when the stirring time of HF is decreased to 15 hours, only very small particles are observed, as illustrated in Figure 3. 8b. However, these small particles are very limited in numbers. Thus, reaction of HF with micelles may occur over extended periods of time, and this was also observed with the micelle system in which LiOH and HF reacted.

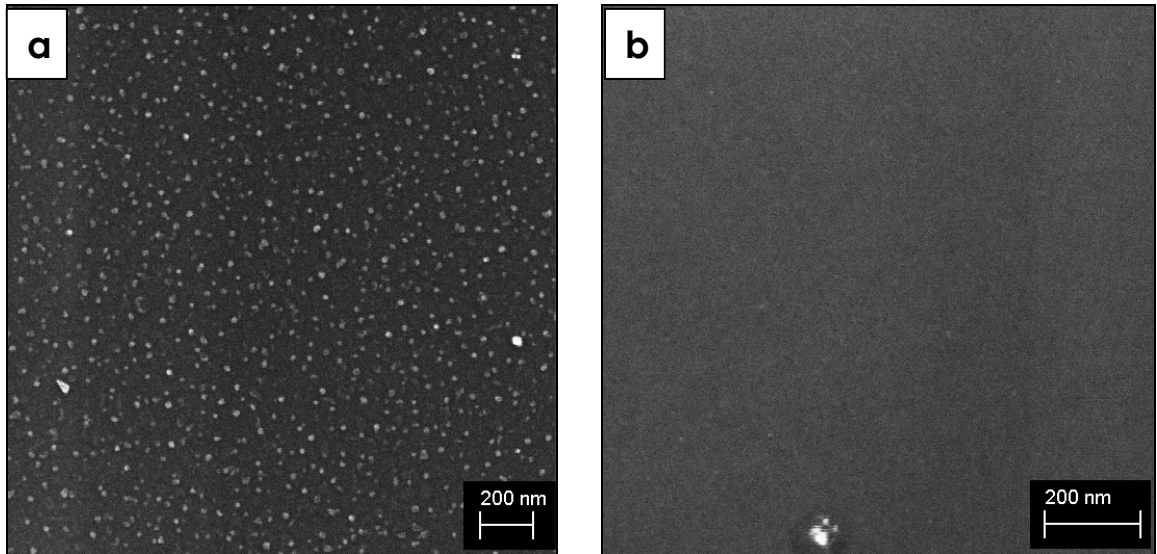


Figure 3. 8: SEM images of only HF loaded micelles coated and etched after 3 days (a) and 15 hours stirring (b)

In order to further understand the effect of HF, PS homopolymer was tried to react with HF(%1), HF (%5) and HF(%40). As the reference, some part of the PS solution was not reacted with HF. These 4 samples were characterized with FTIR. HF(40%) was expected to react with the (fluorinated) benzene ring of PS. However, FTIR characterization showed that all spectral peaks were consistent, without the appearance of additional peaks in all 3 samples. Some portion of the FTIR spectra is illustrated in Figure 3. 9. Therefore, the core

shell particle produced could not be attributed to fluorination of PS block of micelle. This problem was not solved effectively in the project because core-shell nanoparticles were almost never observed in other experiments.

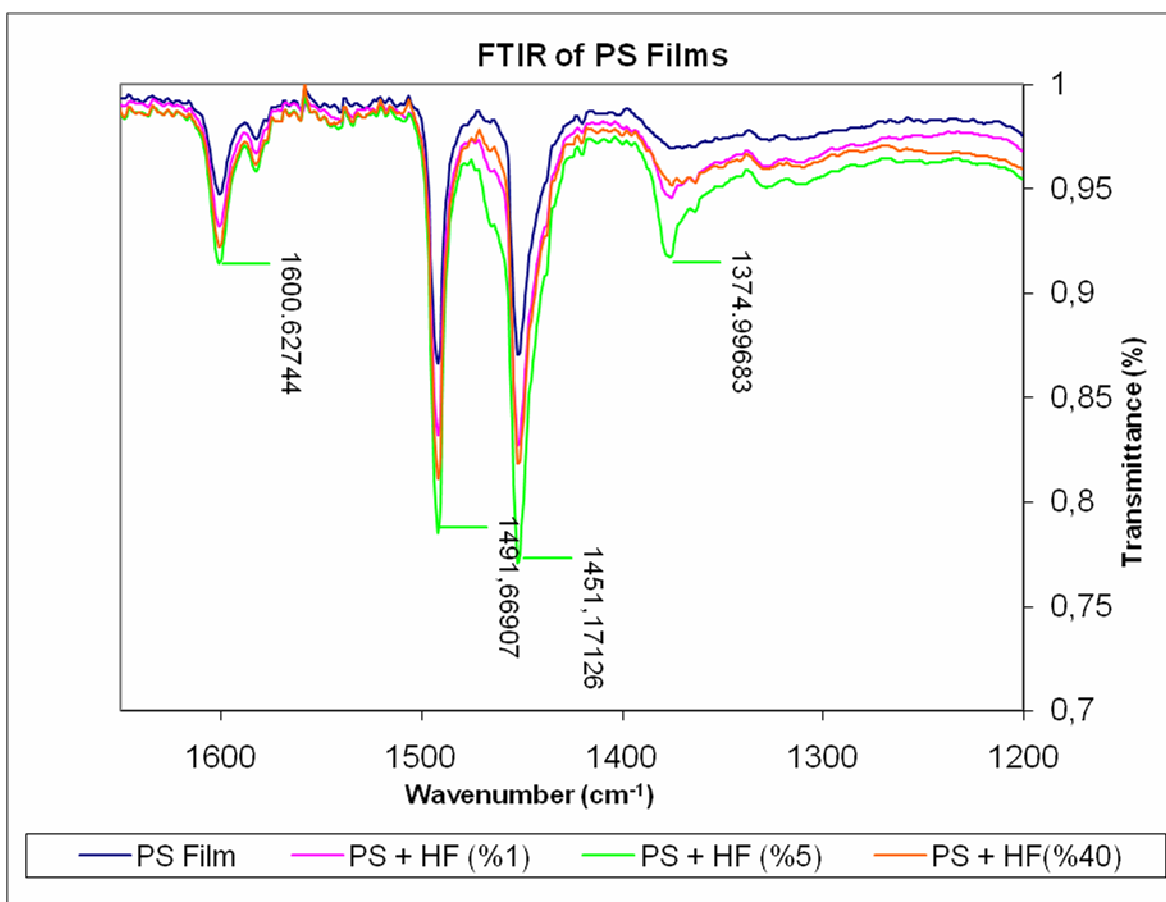
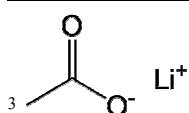


Figure 3. 9: FTIR spectra of 4 samples, PS film, PS+HF(1%), PS+HF(5%) and PS+HF(40%)

There were several problems with the characterization of LiF nanoparticles produced by micelles. The quantities were too low, below the detectability limits of XPS and XRD characterization at the initial trials. For those experiments multiply coated samples and drop cast samples were used respectively to improve the signal-to-noise ratio. Moreover, as the highest band gap materials, LiF cannot be characterized with techniques such as UV-absorption spectroscopy, which can be employed for the characterization of metallic and semiconducting nanoparticles. A ‘plan B’ reaction for LiF formation was also explored. In that reaction, as lithium source, lithium acetate³ (Mw=65.99 g/mol) and as fluorine source



ammonium fluoride⁴ (Mw=37.4 g/mol) was used. The possible reaction should be as following:



Since the LiAc molecule is bulkier than that of LiOH, lower quantities of LiAc was used, such as 1 mg (where we put 1.5 mg of LiOH for 5 ml, 3mg/ml micelle solution), because when the salt amount (volume) is high, super saturation occurs, as observed upon excess loading of LiOH. Indeed, during the reaction, both after LiAc loading and NH₄F addition, super-saturation in the micelle solution occurred. Super-saturation resulted from the micelle instability, when it is loaded. In the case of the polymer that is used in this study, the PS block is shorter than P2VP, and this induces stability problems upon loading an excess of salt inside the micelle.

The SEM image of plan B reaction is shown in Figure 3. 10. Here smaller particles were obtained due to limitations of the vessel for the bulky salt molecules and the solid fluorine compound. In LiOH + HF reaction, LiOH is relatively small, which may enable more LiOH ions to coordinate with pyridine group inside the micelle. In addition, in that reaction, the fluorine source is HF, which is in aqueous environment, whereas NH₄F is solid. Apart from smaller size of particles, there are some extensions observed near the particles. This might have resulted from other products such as carboxymethyl. For comparison a usual nanoparticle formation with the reaction of LiOH and HF is presented in Figure 3. 11. The nanoparticle pattern with this reaction is very clear, without the residual material between the particles, observed in plan B reaction products. At this point, the plan B reaction was discarded.



4



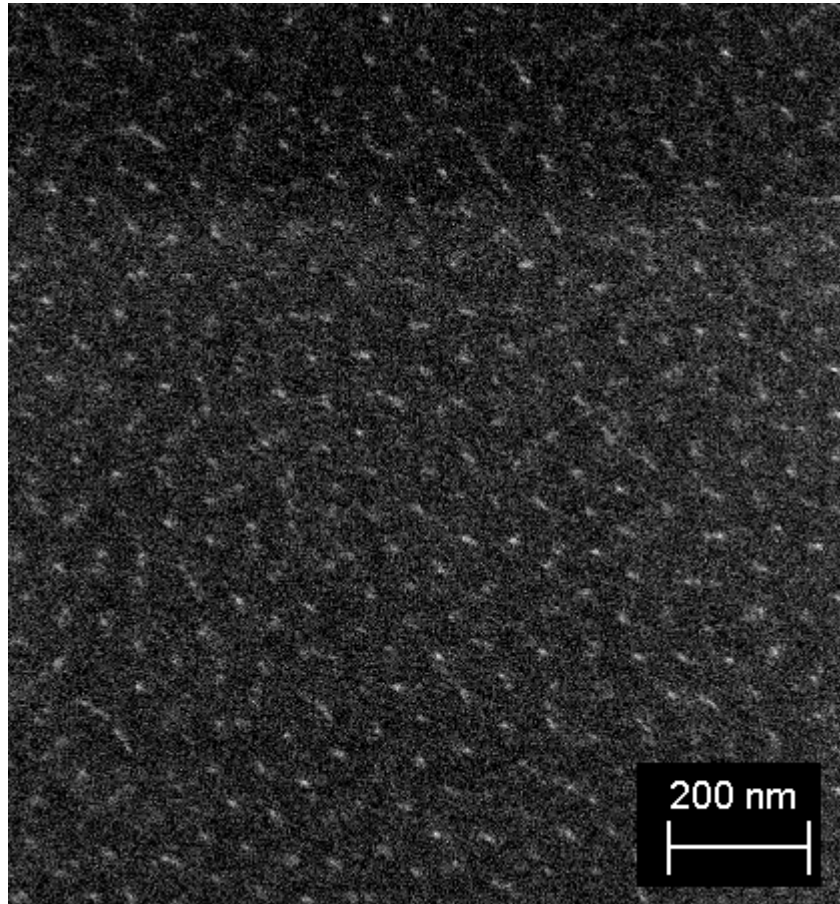


Figure 3. 10: SEM image of M+LiAc+NH₄F on silicon substrate after O₂ plasma etching

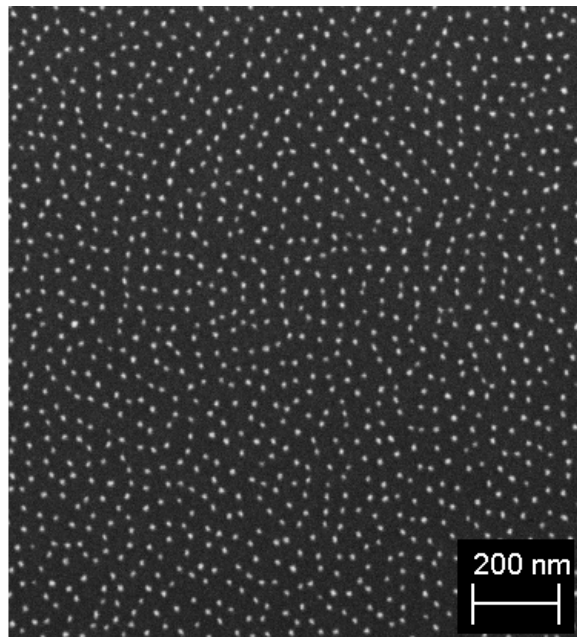


Figure 3. 11: SEM image of M+LiOH+HF prepared in glass vial and spin coated on silicon substrate, after etched with O₂ plasma

After some difficulties, the chemical verification of LiF was achieved by electron and x-ray diffraction. Electron diffraction was performed on LiF loaded micelles, which were drop cast on a lacey formvar-coated Cu grid. XRD was performed on drop cast LiF loaded micelles layer coated on amorphous glass. Both X-ray and electron diffraction spectra can be indexed to LiF, with (111) and (200) peaks at $q_z \approx 2.7$ and 3.1 \AA^{-1} , proving LiF particles had indeed formed inside the polymeric micelle core. STEM-EDX (not shown here) also revealed the characteristic fluorine peak for LiF. Note that similar measurements of unloaded micelles, or ones loaded only with LiOH, showed none of these characteristic signatures of LiF formation. Imaging of the particles were also performed with TEM to determine if the nanoparticles after etching were crystalline and textured on the surface, as suggested by XRD measurements of the micelles before etching. For this purpose samples were coated on a Si_3N_4 membrane and O_2 plasma etching performed after coating. TEM micrograph is given in Figure 3. 13 displays some highlighted particles which are slightly smaller than those produced again on Si_3N_4 substrate (see Figure 3. 7) ($\sim 4\text{-}6 \text{ nm}$ vs. $8\text{-}10 \text{ nm}$); however, they are neither uniformly dispersed on the surface nor uniform in size. This suggests that the coating of the nanoparticles on the TEM grid is not representative of the nanoparticle formation that is typically observable by SEM. By analyzing the particles in Figure 3. 12, we can clearly see that some of the nanoparticles are crystalline. Some particles also show some high angle grain boundaries, suggesting that either nanoparticles have coalesced or that some are made up of multiple crystalline domains. The small size of the particles, similar to or smaller than what was observed in the SEM, suggests that the latter is more likely, especially as some particles may also have amorphous regions (see particle 3 in Figure 3. 12, where both crystalline and amorphous domains are visible). However, it is possible that the amorphous regions correspond to residual polymer. Highlighted in orange (Figure 3. 12) are these amorphous regions with contrast darker than that of the substrate; in some places they are in contact with the particles, while in others they are isolated.. These may also result from the deposition process on the surface, and the non-spherical shapes may correspond to the coalescence of amorphous LiF particles, or the polymer micelle residue from incomplete plasma etching.

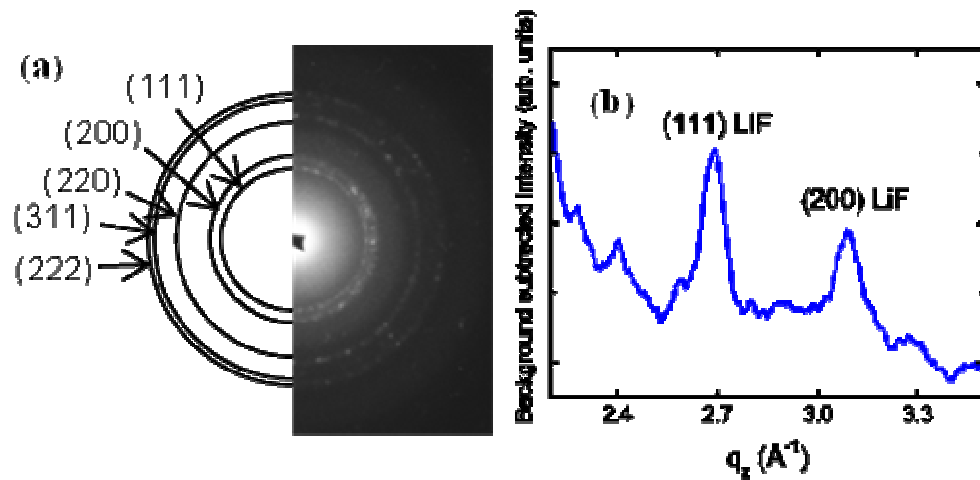


Figure 3. 12: (a) Electron diffraction (Cleva Ow-Yang) and (b) background subtracted x-ray diffraction pattern formed from LiF-loaded polymeric micelles (Ayse Turak and Udo Welzel)

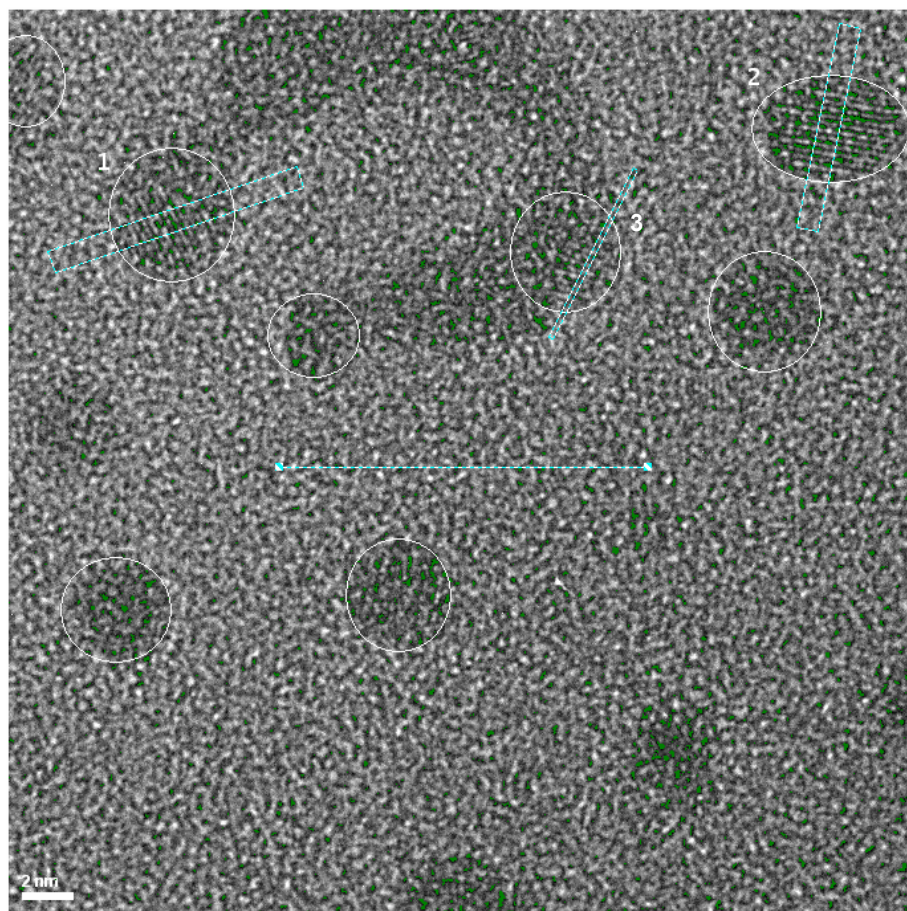


Figure 3. 13: TEM micrograph of LiF nanoparticles on Si_3N_4 grid. Likely particles are highlighted, showing both crystalline and amorphous particles. Line profiles through the background and some particles are highlighted by the blue lines

Electron and x-ray diffraction spectra given above belong to LiF nanoparticles, while they are inside the polymeric micelle. In order to validate the nanoparticle formation after O_2 plasma etching step, grazing incidence XRD was performed in the synchrotron facility at

ANKA (Forschungszentrum Karlsruhe). Grazing incidence diffraction technique allows the characterization of the surface features. Because the technique uses small incident angles surface sensitive (in the order of nanometers) Bragg reflections can be collected from the detector. The synchrotron source produced x-rays with the $\lambda=1.23\text{\AA}$. With the given wavelength the (200) plane of LiF should give rise to a peak at 35.9° , and the resulting peak from the experiment is consistent with the expected value as shown in Figure 3. 14. Thus, XRD directly on nanoparticles proved that the LiF nanoparticles on MgO substrate upon O_2 plasma etching.

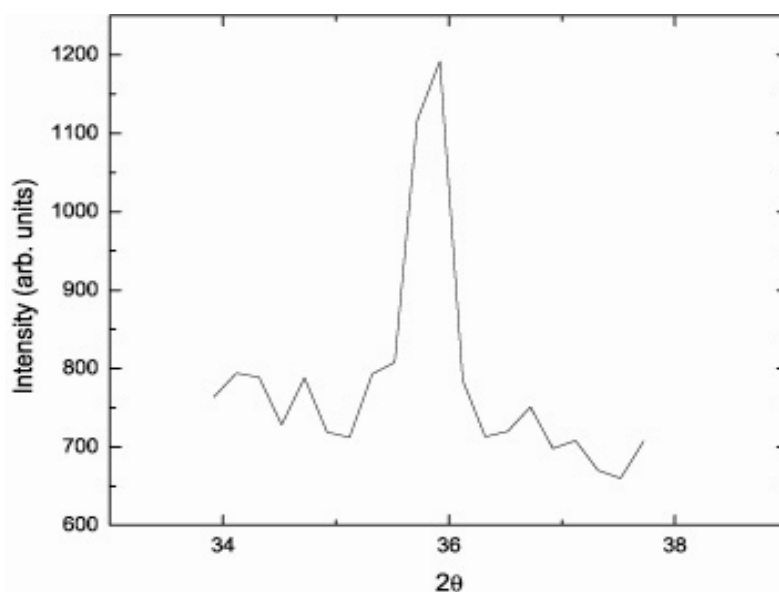


Figure 3. 14: Grazing incidence x-ray diffraction spectra of LiF nanoparticles coated on MgO substrate (Ayşe Turak)

3.2 Work Function Measurements⁵

Work function measurements were performed by special care because the characterization was conducted at KP Technologies, Scotland. In total, 7 samples were sent to be characterized. A bare ITO and O_2 plasma etched ITO was characterized as references (The AFM surface characterization is depicted in Figure 3. 15).

Two different substrates were prepared from solution based LiF, i.e. LiF synthesized by PS-*b*-P2VP copolymer reverse micelles. One of the samples was prepared by one layer coating. The second one was prepared by 3 subsequent coatings, each spin coating step by

followed by O₂ plasma etching step. The schematic illustration of LiF formation and SEM results of 1 and 3 layers of LiF nanoparticle on ITO surface is given in Figure 3. 16. After spin-coating (2000 rpm for 40 seconds) onto ITO-coated glass substrates, oxygen plasma etching was used to remove the polymeric micelles. The nanoparticle size was ~22 nm. The LiF particles were revealed to have covered ~16.6% of the substrate surface, as shown in the secondary electron image in Figure 3. 16(c). Successive coating and etching steps led to sequential coverage of the substrate surface by disconnected LiF islands. The thickness range where an evaporated LiF interlayer is effective in improving device performance is limited to ~1nm in both OLEDs and OPVs^{6,7}. At such thicknesses, LiF forms a discontinuous layer of nanoparticles on the organic surface, similar to that observed in Figure 3. 16 (d)⁸.

Moreover, for comparison, LiF was vacuum evaporated on ITO with 5 Å, 5 Å (O₂ plasma etched) and 10 Å thicknesses; (Ayşe Turak) (thickness monitored by a quartz crystal microbalance (QCM). thermal evaporation of LiF onto ITO substrates also led to the formation of nanoparticle islands with a characteristic island size of ~40 nm. Prior to thermal evaporation, the ITO substrates were annealed at 130°C in vacuum for 30 mins to remove absorbed water and contaminants. During thermal evaporation of LiF, the ITO substrate was masked, to produce regions of LiF covered ITO, and bare ITO for direct comparison with the Kelvin probe, as shown in Figure 3. 17. Thermally evaporated LiF on ITO is polycrystalline, with nearly the <522> texture expected for LiF thin films on amorphous substrates⁹.

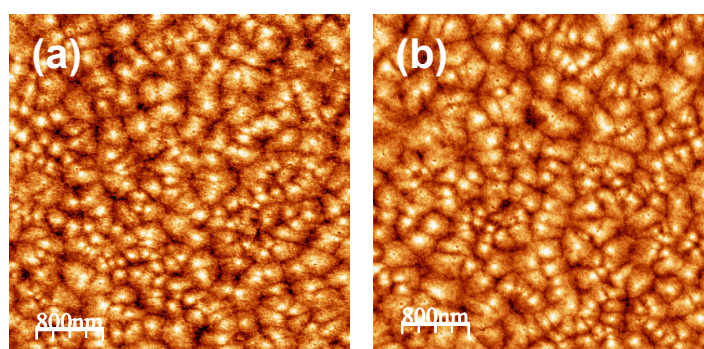


Figure 3. 15: ITO surface – (a) as received ITO (b) ITO surface after O₂ plasma (MPI6) (non-contact AFM). RMS roughness = 0.6nm and 0.94nm respectively (Ayşe Turak)

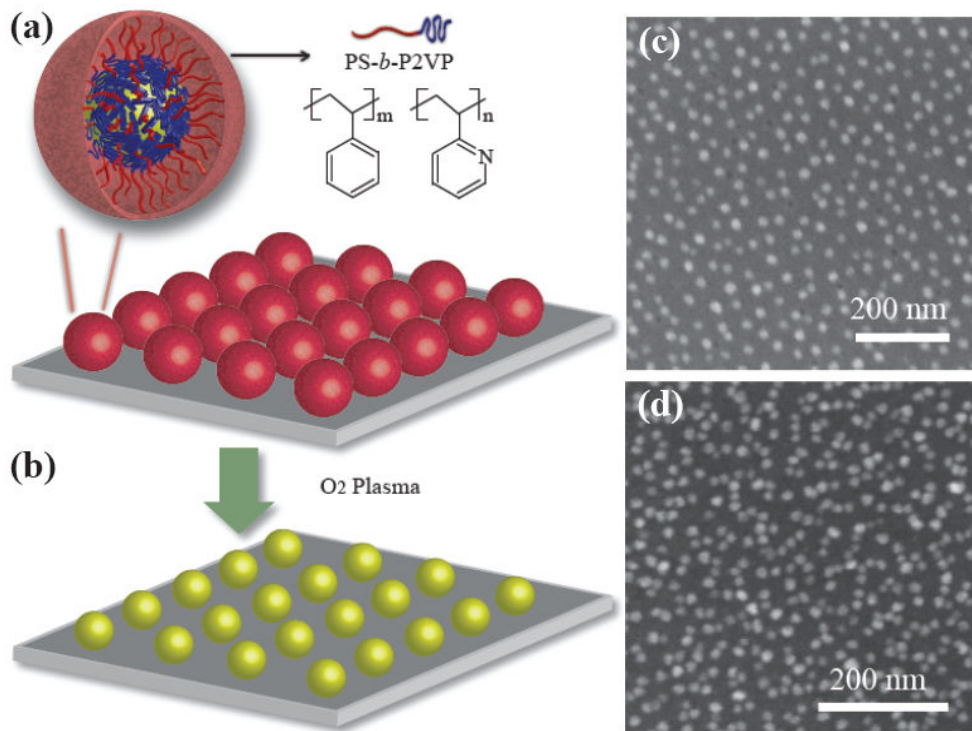


Figure 3.16: Schematic illustration of monolayer of micelle spin coated on ITO before (a) and after (b) O₂ plasma etching. SEM images of (c) a single layer of solution-processed LiF, after etching with O₂ plasma; and (d) three layers of solution-processed LiF, formed by successive spin coating and O₂ plasma etching.

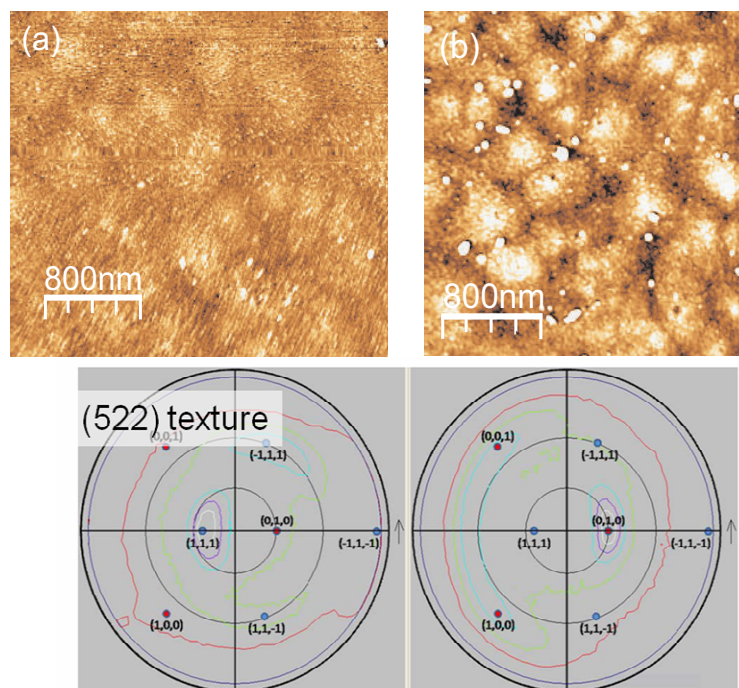


Figure 3.17: (a) MPI3: 10Å LiF thermally evaporated on ITO (b) masked region of MPI3 showing the ITO surface. (non-contact AFM) (c) Overlay of stereographic projection for LiF with indication of the 100 and 111 poles and the measured pole figures for the 111 (left) and 200 (right) reflections of thermally evaporated LiF (Ayşe Turak)

For comparison, LiF was also thermally evaporated onto Diindenoperylene (DIP) organic thin film surface as shown in Figure 3. 18 (Felix Maye, MPI).

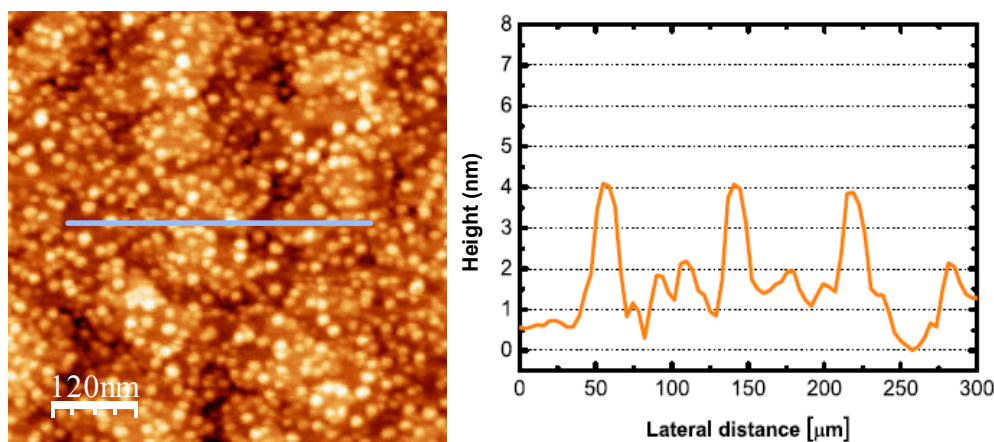


Figure 3. 18: Thermally evaporated LiF (5Å by QCM) on diindenoperylene (5ML) (non-contact AFM) (b) corresponding height profile (Felix Maye)

The work function of the surfaces was measured in an effort to compare the interlayer performance of the solution-processed LiF, forming an electrode bilayer with ITO (sol-LiF/ITO), with that of the thermal evaporated LiF on ITO (thermo-LiF/ITO). As solution processing necessitated the use of an oxygen plasma etch, the effect of plasma treatment was also evaluated on bare ITO and thermo-LiF/ITO.

The work function is extremely sensitive to the surface state, as gases and adsorbates may induce substantial variations in the energy required to remove an electron from the Fermi level. KP yields the average work function of the entire analyzed surface¹⁰. Since device performance is a global value, made up of averaging in parallel all of the local “cells” that arise from microscopic differences on the electrode surface, KP analysis is ideally suited for probing the impact of interlayers in devices¹⁰.

A typical 2D work function map is shown in Figure 3. 19. The average work function, summarized for various samples in Table 3. 1 is the mean work function across a complete scan area. The relative change in the electrode work function, referenced to that of the plasma-etched, bare ITO is also given. The data sets have been nearest-neighbor fitted.

Since the uniform macroscopic work function is of interest, the 2-mm diameter probe head used was sufficiently insensitive to the micro- and nanoscale variations inherently present

in the surface topography of the ITO surface^{10,11} and of the ultra-thin LiF films, which consists of nanoparticle islands (see Figure 3. 19). The standard deviation about the average work function ranged 20-60 meV, which is consistent with the macroscopic work function measurements on real surfaces, *i.e.* surfaces that contain modest inhomogeneity, such as scratches.

Evaporation of LiF onto ITO (see Table 3. 1) leads to a reduction in the ITO work function, as has also been observed on metal surfaces^{12,13}. However, unlike the case for the low work function electrode metal, this should increase the barrier to hole injection at the ITO surface. This confirms that the role of LiF at ITO in OLEDs is to prevent the injection of holes, leading to higher performance from the balance of electron and hole injection in devices^{14,15,16}.

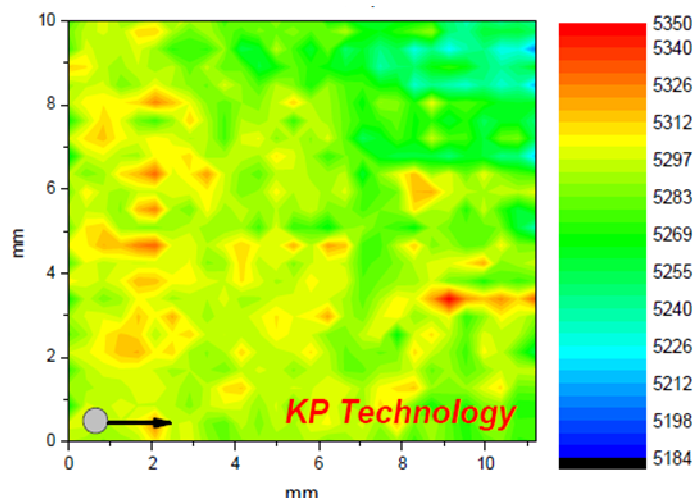


Figure 3. 19: Surface work function map (scanning Kelvin probe) of the electrode bilayer consisting of solution-processed LiF on ITO. The scan area was over 11.2 x 10 mm² with tip radius 2mm. The scans were performed, while maintaining a constant tip-to-sample spacing, in order to facilitate comparison of different samples to the tip.

Table 3. 1: Summary of extracted work function (Φ) from KP using a 2mm calibrated polycrystalline Au tip (calibrated to Au surface with $\Phi = 5.1\text{eV}$).

Sample	Avg. Φ [eV]	$\Delta \Phi$
5-Å, thermo-LiF (S1)	5.06 ± 0.01	-0.045^a
5-Å, thermo-LiF, plasma etched (S2)	5.20 ± 0.02	-0.034^a
10-Å, thermo-LiF (S3)	4.89 ± 0.06	-0.167^a
sol-LiF, etched, 16.6% coverage	5.29 ± 0.02	0.032^b
sol-LiF, etched 24.8% coverage	5.44 ± 0.03	0.189^b
Bare ITO, etch-treated	5.25 ± 0.03	0.130^c
Bare ITO	5.12 ± 0.06	0

^a relative to ITO surface, masked during thermal evaporation

^b relative to etched ITO surface

^c relative to as-received ITO surface

As expected, O_2 plasma etching increases the work function of both the bare ITO and the masked portion of the ITO partially covered with thermo-LiF. Typically, this improvement in work function is associated with the oxidation of OH sites on the surface¹⁷. A similar improvement for both coated and uncoated areas, while maintaining the reduction in work function due to the presence of LiF, suggests that this mechanism still holds, with etching having little impact on the surface state of the LiF particles themselves.

For the sol-LiF monolayer that has been subjected to O_2 plasma etching, the work function is larger than both that of the thermo-LiF/ITO, *as well as that of the etched (bare) ITO*. The resulting *lower* barrier for hole carrier extraction suggests that sol-LiF/ITO would be well suited for an organic solar cell electrode¹⁸. In OLEDs, where charge balance is essential to achieve high performance, it is advantageous to increase the barrier to charge injection by decreasing the work function, as observed for thermo-LiF/ITO. However, in organic solar cells, which do not suffer from this disadvantage, a work function at the electrode surface closer to an Ohmic contact with typical polymer layers is highly

desirable. Energy level diagram is illustrated in the figure below. The sub-monolayer (16% coverage) of sol-LiF/ITO revealed a measured work function of 5.29 ± 0.02 eV. Compared to the 5.1 eV of PEDOT:PSS, the upper valence band edge of LiF is much closer to that of commonly used organic hole transport layers.

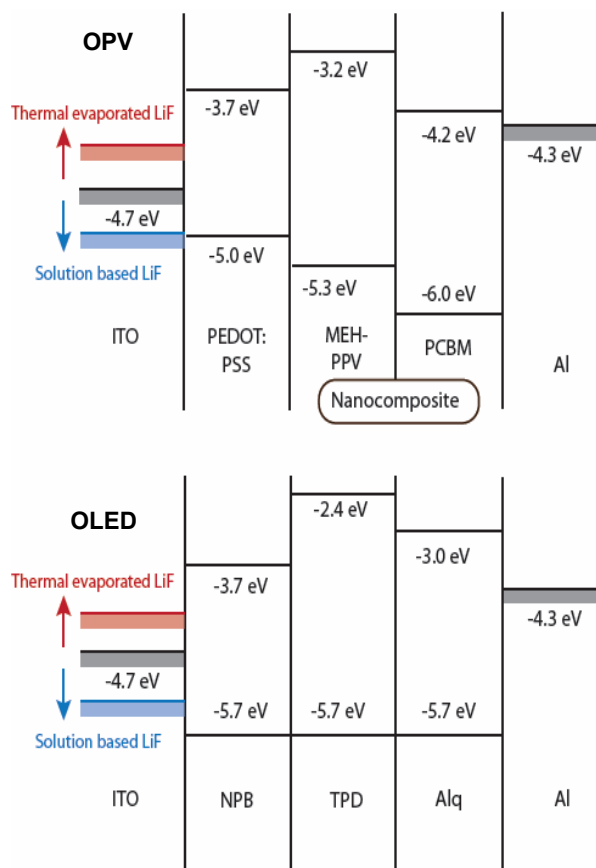


Illustration of energy level changes in OLEDs and OPVs

This unexpected advantage to the sol-LiF/ITO is particularly noteworthy, because this is the first bilayer system in which a dielectric film of nominally the same chemistry could induce a change in work function in the opposite direction on the same electrode. The potential cause may be elucidated from investigating the work of Pacchioni and co-workers, who have reported extensively on work function modification by ultra-thin dielectric films on metal substrates¹³. Although such studies have been carried out on systems assumed to have an epitaxially formed interface, *i.e.* continuous films fully wetting the metal surface, two primary mechanisms have been proposed to explain the modification of the metal work function in opposite directions, determined in large part by the ionicity of the dielectric film. In the case of a positive change in Φ ($\Delta\Phi = \Phi_{m/d} - \Phi_m >$

0), an ultra-thin dielectric film would receive transferred charge from the metal. However, in the case of a dielectric film with highly ionic character, such as LiF, the effective work function would be lowered, due to the electrostatic compression of the overspill electron density by the dielectric ($\Delta\Phi = \Phi_m/d - \Phi_m < 0$). Although an oxide, ITO does have a sufficiently high free charge carrier density, such that one could expect the formation of a surface dipole that would define the work function of the bare ITO. When this overspill charge encounters LiF “islands”, compression back into the ITO would lead to a negative change in the work function, which is typically observed in thermal evaporated LiF on ITO. When solution processed LiF is deposited onto ITO, on the other hand, charge transfer may occur from metal to dielectric, inducing a positive $\Delta\Phi$. The reason behind this charge transfer can be understood by analyzing the study of Mckenna et al ²⁶. In this study, electron trapping behavior of ionic materials such as LiF was analyzed, and it was found that grain boundaries in the structure of such ionic molecules can trap electrons due to their low energy relative to the bulk material. Therefore, the reason for charge transfer to sol-LiF might be due to its polycrystalline structure as observed in electron diffraction ring pattern (Figure 3. 12a), Polycrystalline nature of sol-LiF might bear grain boundaries as electron trapping sites which can cause the electron transfer from metal to dielectric and so that inducing positive $\Delta\Phi$. On the contrary, in the previous studies it was observed that thermo-LiF is more likely to be single crystalline. For this reason, rather than charge transfer, the effective mechanism for thermo-LiF is electrostatic compression of electron density, which results in the decrease of Φ of ITO.

Moreover, the work function could easily be tuned (*i.e.*, the barrier lowered further), by successive deposition of multiple layers of solution-cast LiF with interlayer plasma etch removal of the polymer, as shown by the 0.323 eV increase for 24.8% coverage sol-LiF/ITO. As the quest for higher efficiency also includes modifying the molecular orbital levels of the donor molecules to increase the open circuit voltage and wavelength absorption maxima, a tunable surface work function would give a considerable advantage in the production of advanced solar cells¹⁹.

In sum, it is shown by the work function measurements that LiF produced from solution can be used to tune the surface work function of commonly used electrodes in organic electronics. While the use of an ambient solution-based approach is itself attractive for the

production of low cost organic devices, the ability to tune the surface work function using a controlled bottom-up approach is also of considerable interest in tailoring device performance.

3.3 Fabrication of Inverted Device

Work function measurements proved that LiF nanoparticles obtained from solution processing are well-suited for the electrode bilayer in organic photovoltaics. Although the original plan for the integration of LiF nanoparticles in an organic device was by transfer printing onto the organic layer. Since the cathode is typically Al, it should be vacuum deposited and should not be exposed to air, in order to prevent oxidation. However, because the transfer printing experiments took much longer to develop than anticipated, we fabricated an inverted device to see if LiF nanoparticles obtained from solution to evaluate its performance in organic photovoltaics. In an inverted device, LiF nanoparticles were placed on the Al cathode rather than directly on the organic layer (see Figure 3. 20). Everything was carried out in vacuum and in a glove box, to the maximum extent possible. Even though we took many precautions, exposing the sample to air for short period of time (~5-10 s) was inevitable, due to the necessity for plasma etching to remove the polymeric micelles around the LiF nanoparticles. Instead of O₂, H₂ plasma etching was used here to avoid oxidation of the Al cathode. A control sample was also prepared on a glass substrate from the same solution to characterize with SEM. The resulting SEM image is shown in Figure 3. 21. Similar conditions were attempted by spin coating, which resulted in a quasi-hexagonal packing of ~10-12 nm sized LiF nanoparticles with ~70 nm spacing.

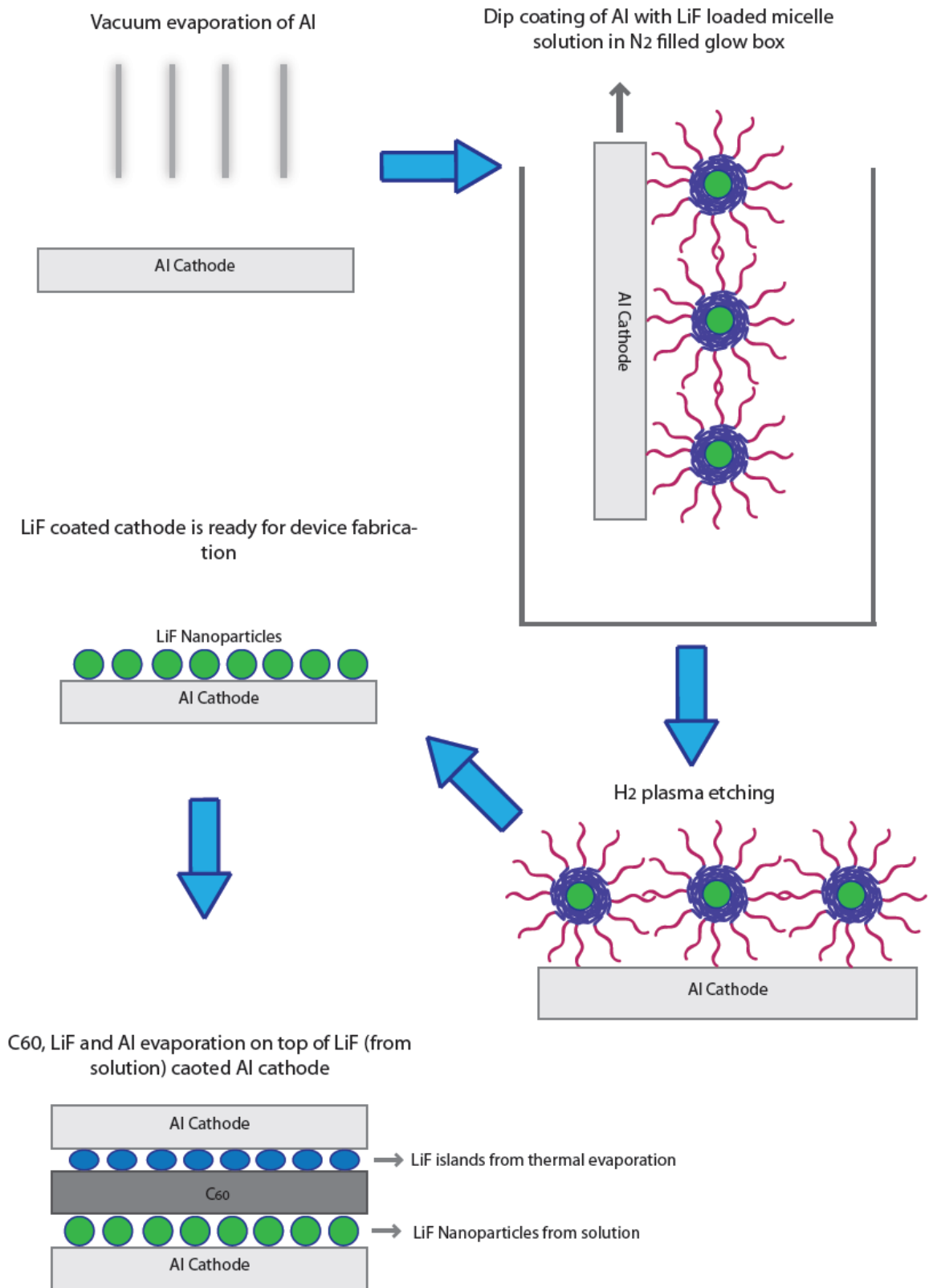


Figure 3. 20: Schematic illustration of experimental procedure for fabrication of inverted device with LiF nanoparticles produced with PS-b-P2VP copolymer reverse micelles

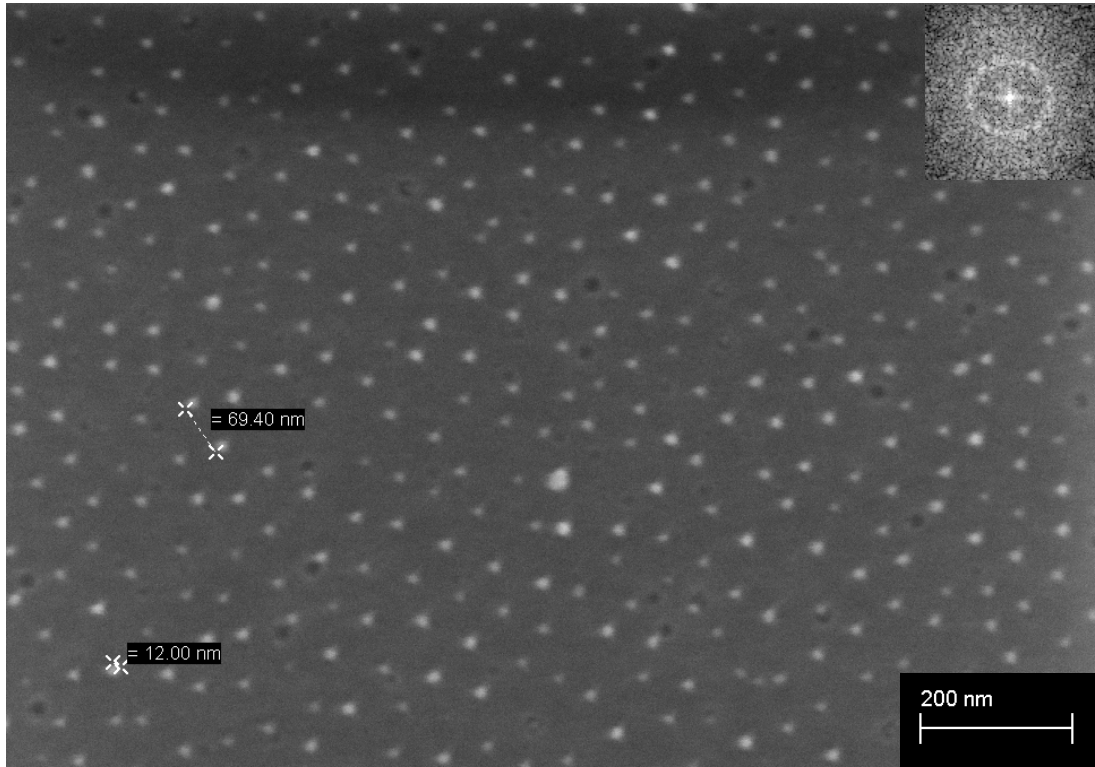


Figure 3. 21: M+LiOH+HF solution that is used on Al substrate, spin coated on glass at 2000 rpm and etched with O₂ plasma with 150 W, 0.1 mbar for 45 minutes. FFT of the image is given in the right corner.

For comparison, a device containing fully vacuum-evaporated LiF layers was also prepared. The device structure for fully evaporated films is Al/LiF/C₆₀/LiF/Al/ITO, while it is Al/LiF/C₆₀/LiF_{NANO}/Al/ITO. Here LiF_{NANO} is denoted for LiF nanoparticles synthesized with micelles. Due to the difficulties of device manufacturing in a vacuum environment, two sets of samples were prepared. Among these, the Al part of one for each device was masked, and the device was divided in 4 individual sub-devices. I-V characteristics of the devices produced were measured under vacuum. The results for the fully vacuum evaporated device Al/LiF/C₆₀/LiF/Al/ITO are presented Figure 3. 22. The devices displayed Ohmic contact, which is desirable for organic devices, and are consistent with the literature for LiF insertion between Al cathode and organic layer⁸. I-V curves for the solution-based LiF device, Al/LiF/C₆₀/LiF_{NANO}/Al/ITO, is shown in Figure 3. 23. Both devices are insulating, which may be attributed to different experimental errors. However, the general trend in the two sub-devices is that they all display ohmic contact behavior. In comparison, the sol-LiF based device the resistivity is higher. This might be due to the brief air exposure of the device containing sol-LiF. Although there were imperfections in the experimental procedure (air exposure of cathode), most devices (and sub-devices)

displayed Ohmic behavior. This was particularly important to prove that LiF synthesized by micelle reactors can actually be used in OPVs. Further numerical analysis was not carried out on these proof-of-concept devices, because complications in production render the inverted structure devices impractical for implementation.

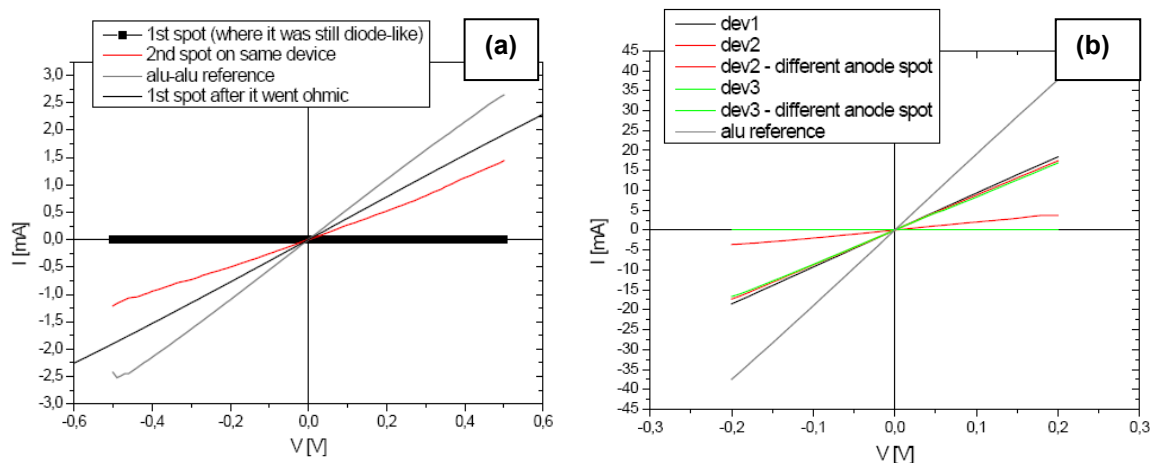


Figure 3. 22: I-V curves for the devices produced from only thermal evaporated LiF films. Unmasked (O776) (a) and masked (O779) devices (b).

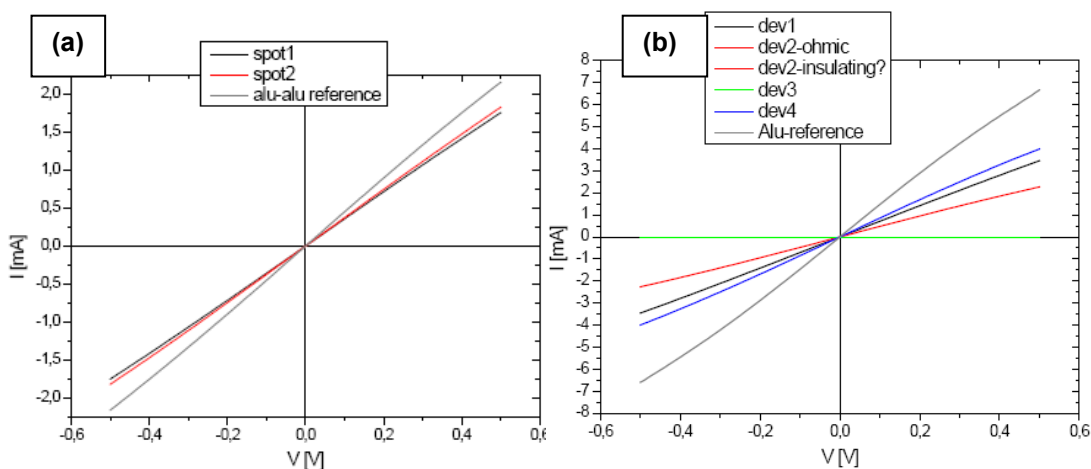


Figure 3. 23: I-V curves for the devices produced from solution based LiF nanoparticles. Unmasked (O777) (a) and masked (O778) devices (b)

3.4 Effect of Direct Coating Conditions on Organic Surfaces

Before starting the any transfer printing process, we sought to try the direct coating of particles on organic layers. However, because this process involves more than a single

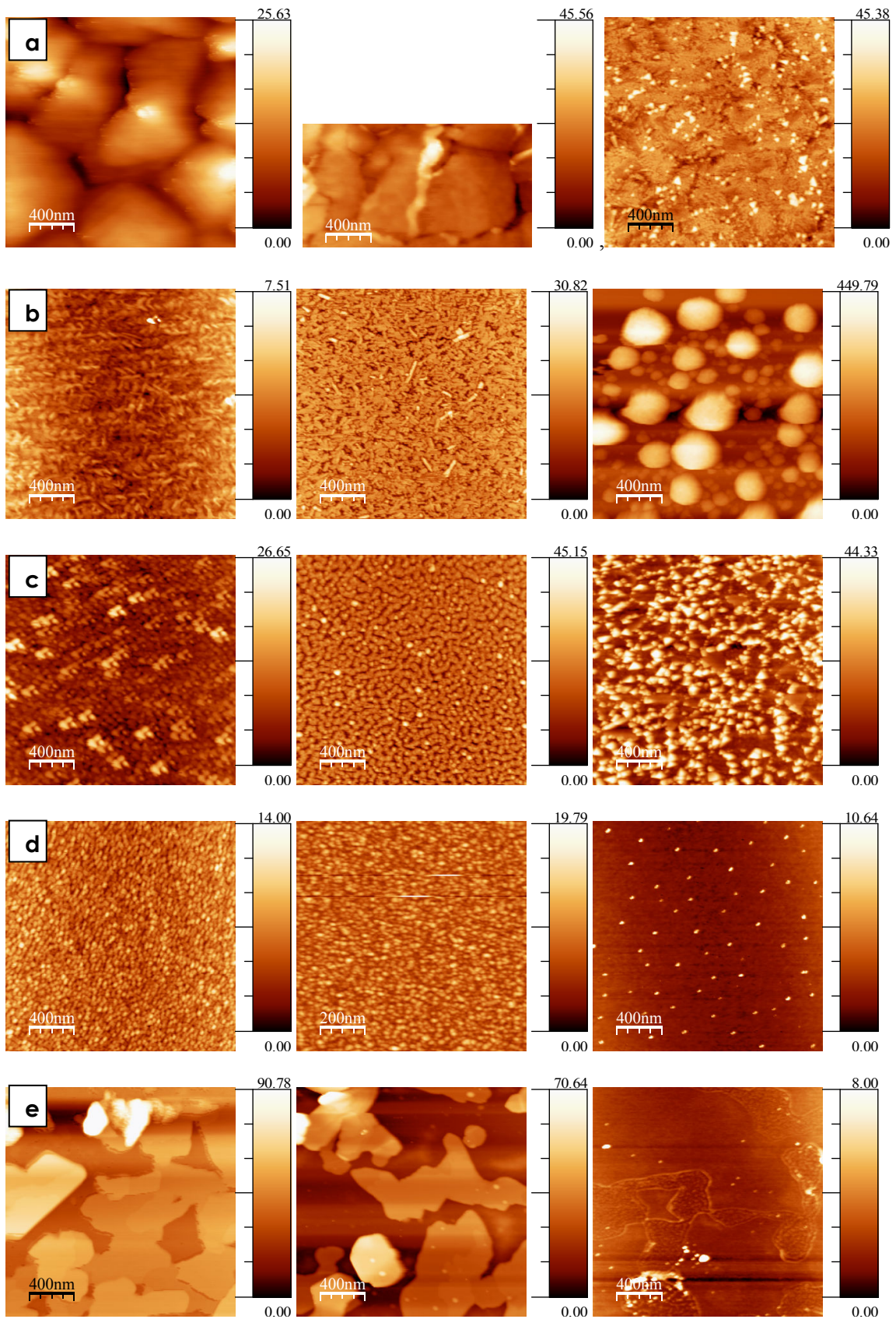
step, we initially investigated the effect of each step on organic layers independently. The list of organic layers that were studied is given in Table 3. 2.

Organic Layer	Short Name
C ₆₀ (On ITO)	CHB 202B
HCuPc (On ITO)	CHB 203B
Pentacene (On ITO)	CHB 204B
PTCDI (On Si)	O559
DIP (On ITO)	O571
DIP (On Si)	O643
C ₆₀ (On Si)	O665

Table 3. 2: List of organic layers that were analyzed

In the direct coating process the first step involves spin coating of particles. In this step, the effect of toluene on organic layers is an issue that should be considered. Secondly, spin coated particles require plasma etch removal of the micelles, but this may also etch the underlying organic layers, mandating a separate analysis. Hence, initially atomic force microscopy (AFM) characterization of non-processed organic layers was performed, followed by toluene exposure, and finally by H₂ plasma-etching. The results are presented in Figure 3. 24. For all the experiments, at least two images were captured for comparing reproducibility, but only representative images are shown. Short toluene exposure does not seem to affect the organic layer surface, as seen from the images below. On the other hand, H₂ plasma exposure modified all of the surfaces. Interestingly, organic layers on silicon substrate seem to be affected more than the ones on ITO. This difference can be better observed on DIP, which was both on silicon (O643) and ITO (O571) substrates.

Initial Surface After toluene exposure After H₂ plasma etching



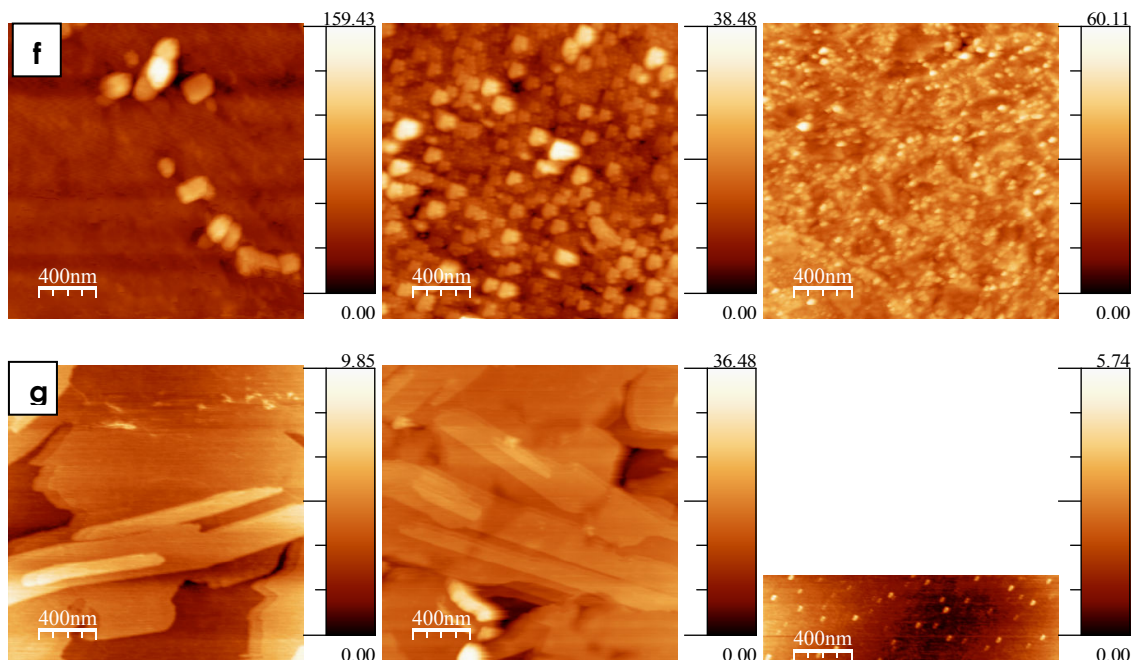


Figure 3. 24: AFM images of (from left to right) initial surface- after toluene exposure- after H₂ etching of CHB 204B (a), CHB 203B (b), CHB 202B (c), O665 (d), O643 (e), O571 (f), O 559 (g).

These plasma results clearly indicated that direct printing was not possible on a DIP surface that was evaporated on the ITO substrate. After coating with a monolayer of LiF-loaded micelles, the substrate was introduced to the H₂ plasma. It was observed by eyes that the pink color on the ITO substrate had decreased, and when the sample was analyzed with SEM, formation of small islands on the surface were seen (Figure 3. 25). This kind of alteration on the surface is excessive and undesirable for the final device. Therefore, we did not continue this study further.

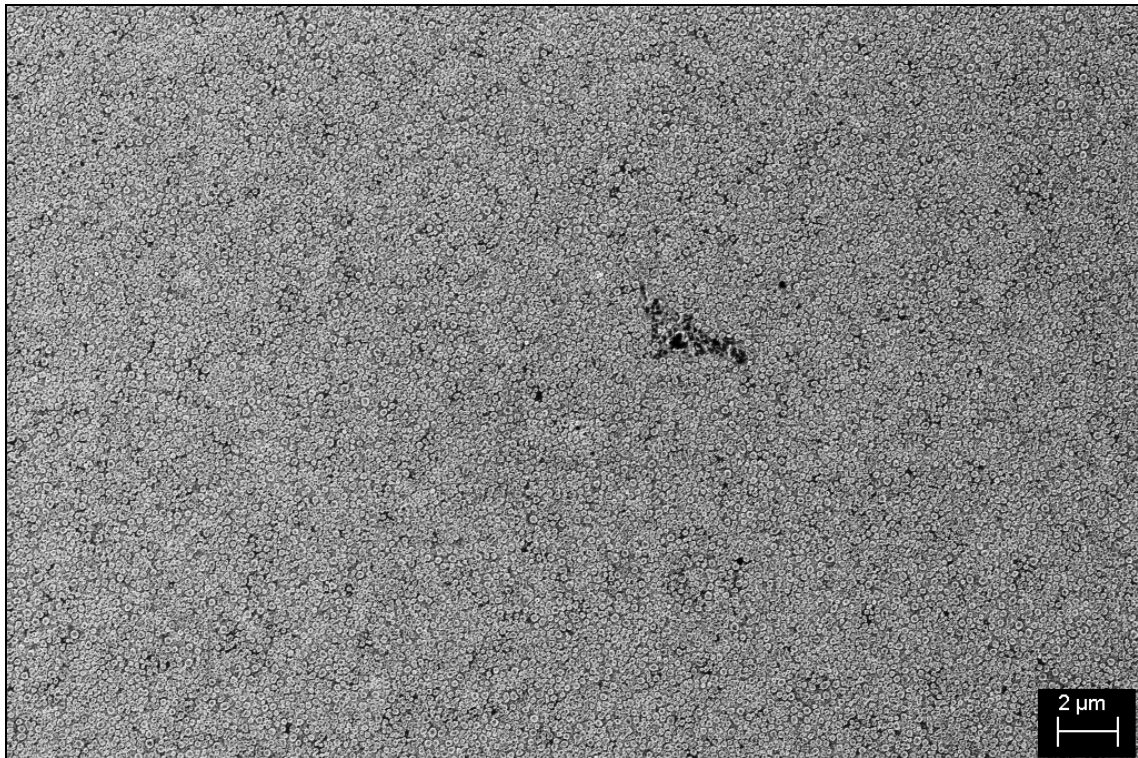


Figure 3. 25: SEM of DIP surface initially coated with LiOH and HF loaded micelles and etched with H₂ plasma

Direct printing studies involve just two substrates: donor and receiver substrates. This study was not applied to small organic molecules; instead it was applied to P3HT-PCBM, which is a commonly used polymer blend for the acceptor layer in organic photovoltaics. This was one of the easiest and promising methods to explore before trying the PDMS pressing. Two experiments (NTP 15, NTP 21⁵) were performed, and in both nanoparticle transfer was not achieved. This study did not proceed mainly because of phase segregation of the polymer blend, when it is heated and held for a long time at ~100 °C. The phase segregation of P3HT and PCBM can be clearly seen in Figure 3. 26.

⁵ NTP is the abbreviation of nano transfer printing studies carried out with PDMS, and for the ease of experiment following, numbers are given for nano transfer printing experiments.

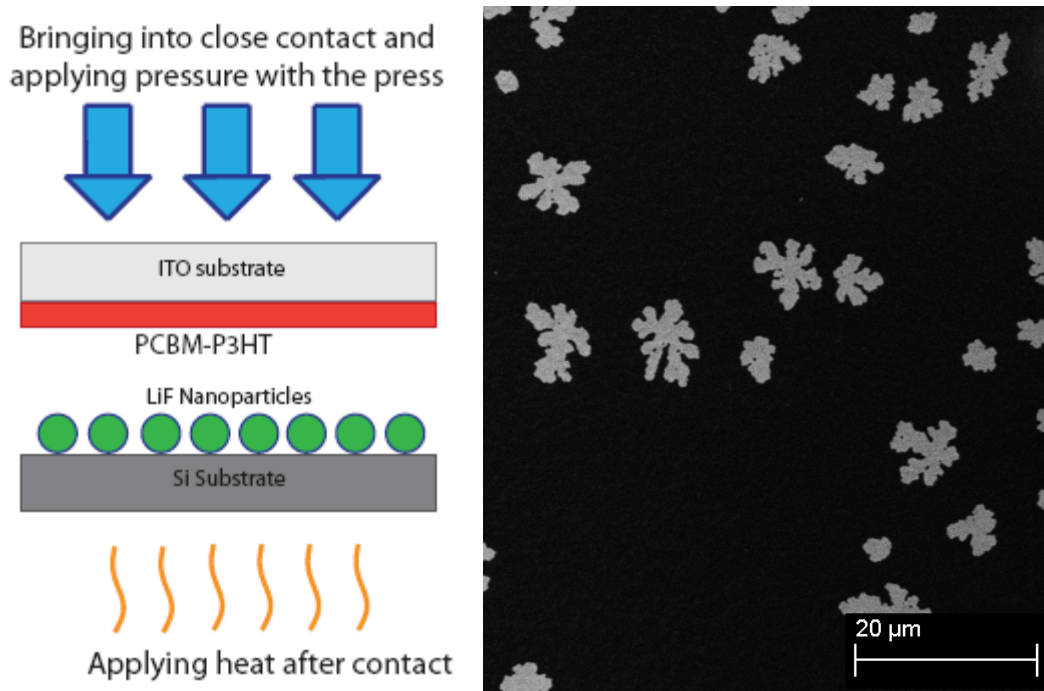


Figure 3. 26: Schematic illustration for direct printing and SEM result for P3HT-PCBM film upon heating

3.5 Nanotransfer Printing Experiments

3.5.1 PDMS Results

PDMS Curing Studies

PDMS curing on nanoparticles had initially appeared to be a good way of removing nanoparticles from the donor substrate, given reports in the literature on this method for forming microscale and nanoscale features on a PDMS surface. In order to achieve this, curing on several substrates was performed (see Table 3. 3)

. Among all the substrates only the O₂ plasma-processed ITO was successful. On the other surfaces, after curing, PDMS could not be peeled off, and bonding was observed between PDMS and the other surfaces.

SUBSTRATE	PLASMA	PDMS CURING
Silicon	O ₂	-
	H ₂	-
Glass	O ₂	-
	H ₂	-
Silicon Nitride	O ₂	-
	H ₂	-
H terminated Silicon	O ₂	-
	H ₂	-
Indium tin oxide	O ₂	+
	H ₂	-

Table 3. 3: List of substrates on which PDMS curing was tried

Several experiments were conducted for PDMS curing on ITO with a nanoparticle layer, by varying the curing temperature of curing. In none of the experiments nanoparticles were able to be removed from the donor substrate. The details of these experiments can be checked from **Hata! Başyuru kaynağı bulunamadı.**

PDMS Pressing Studies

With its adhesive property and low surface energy PDMS is an attractive material for transfer printing. The challenge is to remove nanoparticles from donor substrate to PDMS layer. If the particles sit on the PDMS surface, transferring them to another substrate is not very difficult. For such process two important interface forms, particle-PDMS and particle-substrate (receiver). The difference between the work function of adhesion of these two interfaces substrate-particle ($W_{sub-par}$) and PDMS-particle ($W_{PDMS-par}$) can be written in the intimate contact²⁰

$$W_{\text{sub-par}} - W_{\text{PDMS-par}} = (\gamma_{\text{sub}} - \gamma_{\text{PDMS}}) - (\gamma_{\text{sub-par}} - \gamma_{\text{PDMS-par}})$$

where γ_{sub} and γ_{PDMS} are the surface energies of the substrate and the PDMS. The $\gamma_{\text{sub-par}}$ and $\gamma_{\text{PDMS-par}}$ are the interfacial energies between substrate and particle and between PDMS and particle respectively. The second term $(\gamma_{\text{sub-par}} - \gamma_{\text{PDMS-par}})$ can be much smaller than the first $(\gamma_{\text{sub}} - \gamma_{\text{PDMS}})$, because it is often the case that $\gamma_{\text{par}} \gg \gamma_{\text{sub}}$ or γ_{PDMS} where γ_{par} is the surface energy of the particle. The particles in this study are LiF nanoparticles and substrates are glass or silicon in most cases. The surface energies of most common substrates and LiF is given in the Table 3. 4²⁰. The difference in work of adhesion is then roughly equal to the difference in surface energies of the substrate and the PDMS. For most materials, the PDMS interface is weaker than the substrate interface because of the low surface energy (19.8 mJ/m²) of PDMS. Therefore, if the proximal contact is established between LiF particle-coated PDMS stamp and the receiver substrate long enough, LiF particles will transfer to the receiver substrate. It was reported that, the contact time should be kept longer for lower surface energy substrates and additional thermal energy should be applied to decrease the time of transfer such as contact times of several days from PDMS to PET but only 2 h at 45 °C²⁰. Heating can facilitate diffusion of low molecular weight component of PDMS to the surface, accelerating the surface hydrophobic recovery and decreasing the surface energy. Therefore, once the LiF particles can be transferred from donor substrate to PDMS, the transfer from PDMS to organic layers, such as pentacene, MEH-PPV can be relatively easy and straightforward.

Material	Surface Energy (mJ/m ²)
PDMS	19.8
PET	44.6
Polythiophene	38.0
Polyimide	37.4
Polypropylene	29.6
MEH-PPV	28.0
Pentacene	23.7
Gold (Au)	1500.0
Titanium (Ti)	2100.0
ITO	45.0
Teflon	18.5 (20)
LiF	480.0
Glass	72.0
Silicon	60-90

Table 3. 4: Surface energies of common substrates and surfaces.

Before performing the PDMS pressing experiments, the effect of PDMS pressing on organic surfaces (*i.e.*, the receiver substrate) were studied. The AFM results are shown in Figure 3. 27, and any significant change on organic surfaces was not observed after PDMS pressing. Therefore, PDMS pressing is not sufficiently harsh to alter the surface of small organic molecules. In addition to our studies, it has been reported that small features were transferred from a PDMS surface to pentacene, which is one of our organic molecules²⁰. Here, it was discussed that because the surface energy of PDMS (19.8mJ/m²) is lower than pentacene (23.7 mJ/m²), it is easy to transfer features from PDMS to pentacene. However, due to the low difference between two, it was suggested that contact time should be increased and slight heating should be done to full transfer of features. Thus, if the particle adhesion on the PDMS surface could be achieved, then the transfer of particles from the PDMS surface to organic molecules will not be difficult.

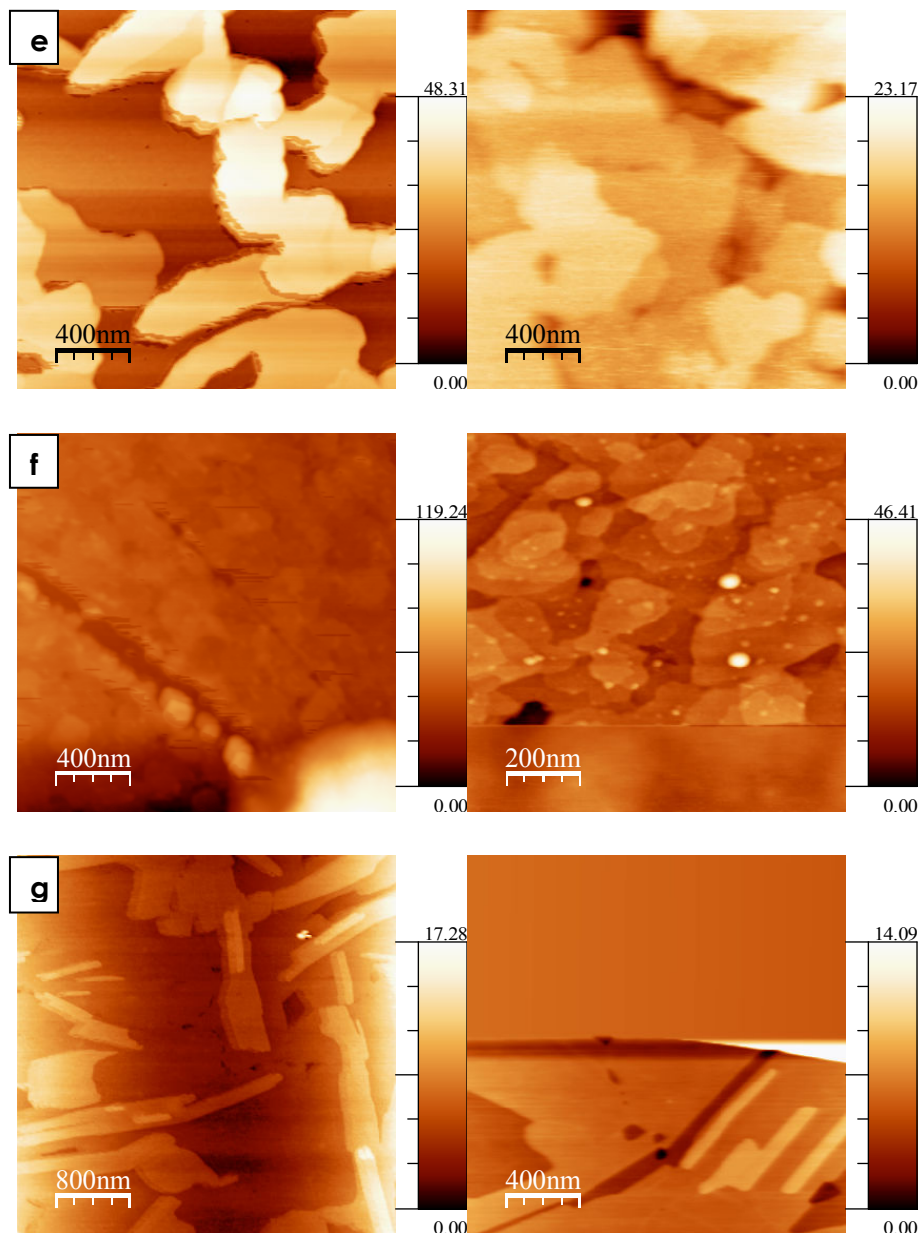


Figure 3. 27: AFM images of (from left to right) initial surface- after PDMS pressing of CHB204B (a), CHB 203B (b), CHB 202B (c), O665 (d), O643 (e), O571 (f), O 559 (g).

After ascertaining the effect of PDMS pressing on organic molecules, pressing experiments were started on nanoparticles deposited on the organic layers. Apart from NTP 1 and NTP 2 that were performed using LiF powder, particle removal from the surface could not be achieved. This could be attributed to the very small size of the particles (around 10 nm) and the strong interaction between the particles and the substrate. Particularly in the case of silicon substrate, the growth of an additional oxide layer during the plasma etching yielded particles embedded in this oxide layer. This kind of interaction required a very strong

adhesion (*i.e.*, primary bonds) to remove the particles from the substrate surface. In order to increase the particle-PDMS interaction, PDMS was briefly (5 min) exposed to O₂ plasma and immersed in ethanol to passivate the surface. Hence the surface became more rigid and more hydrophilic yet, this was not enough to remove the particles from the surface (NTP 18).

NTP 10-11-12 yielded perhaps the most interesting results among the PDMS pressing experiments. The initial characterization of these experiments was performed with AFM, and the results are presented in Figure 3. 28 - Figure 3. 29 (NTP 10) - Figure 3. 30 (NTP 11) - Figure 3. 31 - Figure 3. 32 (NTP 12). These results seemed very promising in the first glance and suggested that the nanoparticles were successfully removed. However, for validation, the silicon surface of NTP 11 experiment was inspected with SEM, and almost all the particles remained on the sample surface, as illustrated in **Hata! Başyuru kaynağı bulunamadı.** Thus for the NTP experiments, AFM should not be the only characterization technique used to interpret the results. However, even in these images, AFM shows some decrease in height where nanoparticles are located. These experiments should be considered in future work.

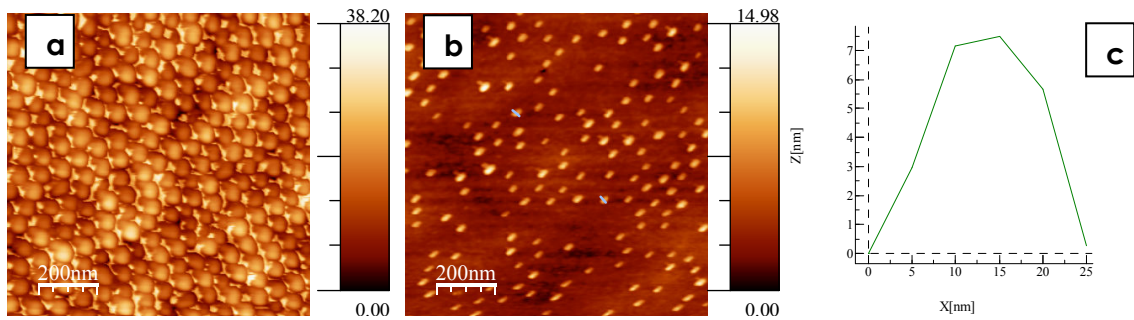


Figure 3. 28: AFM image of micelles (3mg/ml) loaded with LiOH, and after HF addition, spin coated (2000 rpm) on normal (100) silicon substrate, before etching (a), on ITO after etching with O₂ plasma (b) and corresponding height profile (c)

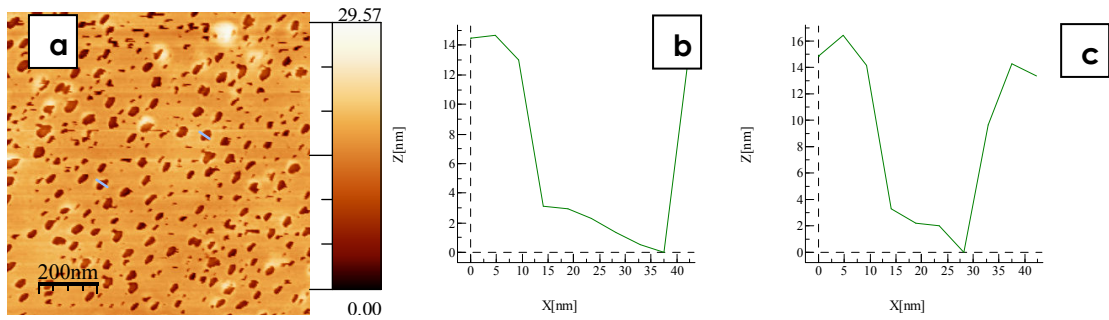


Figure 3. 29: AFM image of micelles (3mg/ml) loaded with LiOH, and after HF addition, spin coated (2000 rpm) on ITO substrate (a), afterwards etched with O₂ plasma (150 W, 0.1 mbar, 1 hour), after PDMS pressing; and corresponding profiles (b)-(c)

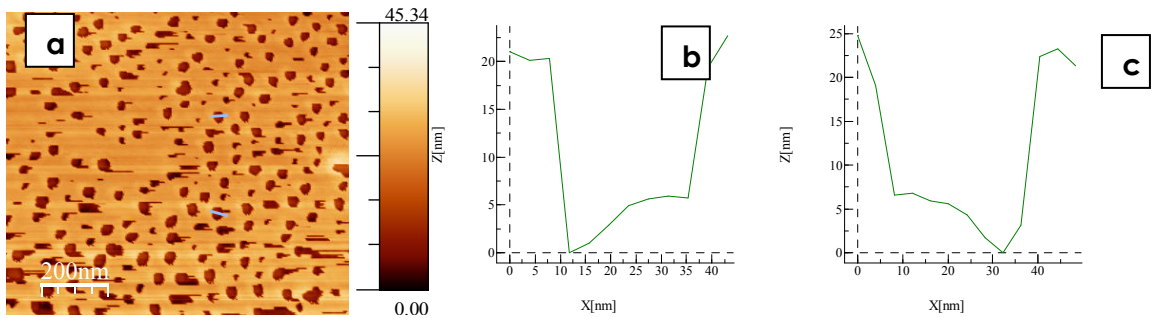


Figure 3. 30: AFM image of micelles (3mg/ml) loaded with LiOH, and after HF addition, spin coated (2000 rpm) on H-terminated silicon substrate (a), afterwards etched with O₂ plasma (150 W, 0.1 mbar, 1 hour), after PDMS pressing; and corresponding profiles (b)-(c)

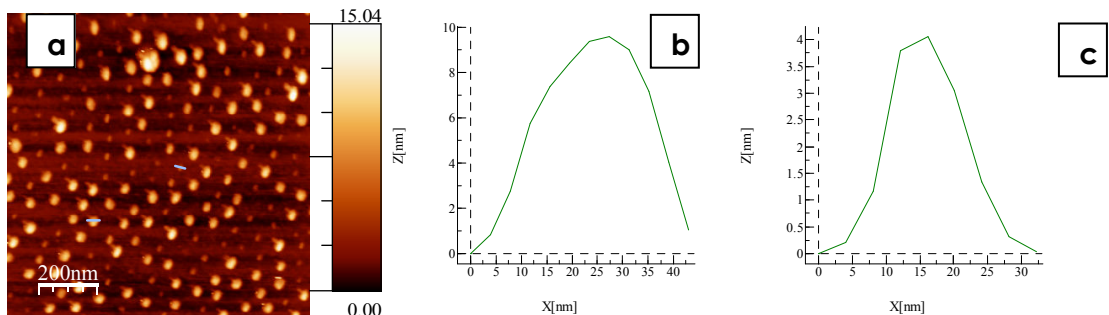


Figure 3. 31: AFM image of micelles (3mg/ml) loaded with LiOH, and after HF addition, spin coated (2000 rpm) on normal (100) silicon substrate (a), afterwards etched with O₂ plasma (150 W, 0.1 mbar, 1 hour), BEFORE PDMS pressing; and corresponding profiles (b)-(c)

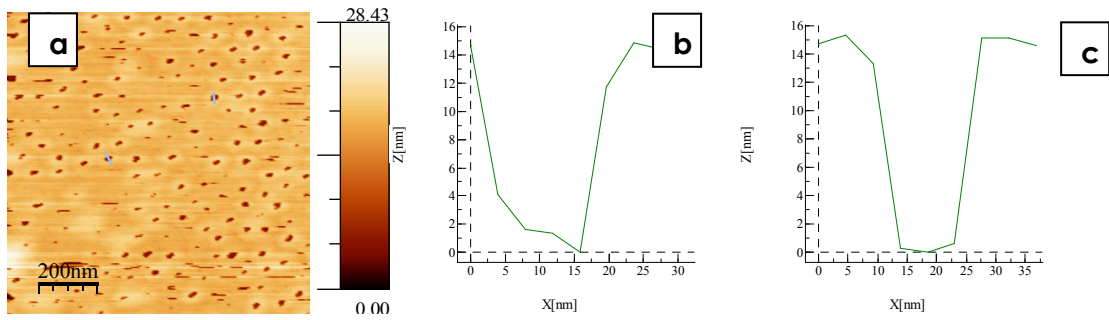


Figure 3.32: AFM image of micelles (3mg/ml) loaded with LiOH, and after HF addition, spin coated (2000 rpm) on normal (100) silicon substrate (a), afterwards etched with O₂ plasma (150 W, 0.1 mbar, 1 hour), AFTER PDMS pressing; and corresponding profiles (b)-(c)

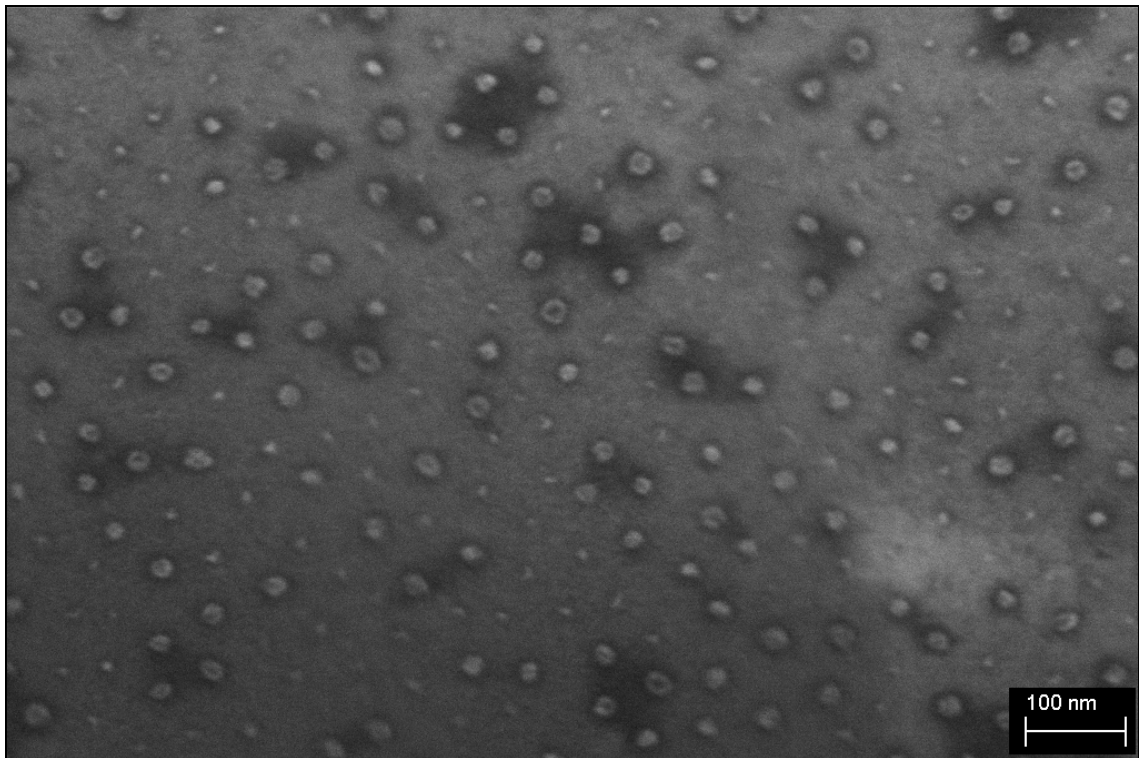


Figure 3.33: SEM image of silicon surface of NTP11 experiment

The summary of NTP experiments are given in Table 3.5. This can be used to refer and remember any NTP studies.

	Type	Substrate	Temp.	Time(min)	Explanation
NTP 1	PDMS Pressing	LiF powders on glass	23 °C	210	PDMS grabbed all the powder
NTP 2	PDMS Pressing	LiF powders on glass	23 °C	15 (s.)	PDMS grabbed all the powder
NTP 3	PDMS Releasing	Glass	23 °C	10	Slow peeling, almost nothing was released
NTP 4	PDMS Releasing	Glass	75 °C	45	Slow peeling, almost nothing was released
NTP 5	PDMS Curing	O ₂ etched nanoparticles on Si	85 °C	125	Cross-linking between substrate and PDMS
NTP 6	PDMS Curing	H ₂ etched nanoparticles on Si	85 °C	125	Cross-linking between substrate and PDMS
NTP 7	PDMS Curing	H ₂ etched nanoparticles on ITO	85 °C	125	Cross-linking between substrate and PDMS
NTP 8	PU-PDMS cast	Nanoparticles on silicon	23 °C	180	Nanoparticles remained almost the same
NTP 9	PU-PDMS cast	O ₂ etched nanoparticles on Si	23 °C	150	Particles were affected by THF but largely remained on surface
NTP 10	PDMS Curing	O ₂ etched nanoparticles on ITO	90 °C	120	Peeling-off was successful, nanoparticle removal was not
NTP 11	PDMS Pressing	O ₂ etched nanoparticles on H term. Si	23 °C	210	Nanoparticles remained almost same
NTP 12	PDMS Pressing	O ₂ etched nanoparticles on Si	23 °C	210	Nanoparticles remained almost same
NTP 13	PDMS Pressing	O ₂ etched nanoparticles on Si	23 °C	120	Silicon substrate was pressed on PDMS, no change
NTP 14	PDMS Pressing	O ₂ etched nanoparticles on Si	75 °C	150	Nanoparticles remained almost the same
NTP 15	Direct Printing	ITO to P3HT-PCBM on ITO	140 °C	120	Polymer was stuck to the other surface
NTP 16	PDMS Curing	O ₂ etched nanoparticles on ITO	23 °C	40 (h.)	Nanoparticles remained almost the same
NTP 17	PDMS Curing	O ₂ etched nanoparticles on ITO	45 °C	15 (h.)	Nanoparticles remained almost the same
NTP	PDMS Pressing	H ₂ etched nanoparticles on H	23 °C	120	O ₂ plasma-PDMS used, nothing

18		term. Si			removed
NTP 18 R	PDMS Pressing	H ₂ etched nanoparticles on H term. Si	23 °C	120	O ₂ plasma-PDMS used, nothing removed
NTP 19	PDMS Curing	O ₂ etched nanoparticles on ITO(heat 270°C)	23 °C	15	6 hour room temp-9 hour at 60 °C
NTP 20	PDMS Pressing	O ₂ etched nanoparticles on Si ₃ N ₄ (heat 270°C)	110 °C	120	Nanoparticles remained almost the same
NTP 21	Direct Printing	ITO to P3HT-PCBM on ITO	100 °C	115	Nanoparticles remained almost the same
NTP 22	PDMS Pressing	O ₂ etched nanoparticles on Si ₃ N ₄	24 °C	225	Nanoparticles remained almost the same

Table 3. 5: Summary of most nanotransfer printing experiments

Weakening the Particle-Substrate Interaction Studies

As mentioned in the previous section, the interaction between nanoparticles and substrate is very strong, and experiments were conducted to decrease this interaction. First, the substrates on which nanoparticles present were heated to 270 °C, in order to remove the polymeric part (if any existed) between the substrate and the particles. This temperature is high enough to bring polymers above their T_g or decompose them. This organic part was thought to be the remaining micelles, as in the case of core-shell nanoparticle observation. From the SEM images, there were no changes detected, and these substrates were used in NTP experiments (NTP 19 and NTP 20). However, the result was similar to the non-heated substrates, from which none of the particles could be removed from the surface.

Apart from heating experiments, water bath immersion experiments were performed. Samples were held in water for lengths of time exceeding 12 hours, and no change was observed for the dimensions of particles. This was notable, because if the particles were dissolved in water, then removal of smaller particles from the surface cavities (if they existed) would have been easier. Even 15 minutes of water bath sonication changed neither the position nor the size of particles. In addition, sonication in acetone was tried. However

again, there was not any change in the position of the particles. To achieve this, the sonication time may be extended for the future experiments.

Up to this point, single crystal silicon wafer was the substrate of choice. However, glass substrates were considered after reports²¹, comparing the O₂ plasma etching performance of the two as supports for a Au nanoparticle (see Figure 3. 34). When plasma reduction was applied during the nanoparticle synthesis in block copolymer micelle reactors on a silicon substrate, oxide growth occurs. At the end of plasma cleaning, the nanoparticles had become partially buried in an SiO_x layer. On the other hand, only cavities formed when the particles were on glass, which might be a result of the high energy and temperature involved the plasma process.

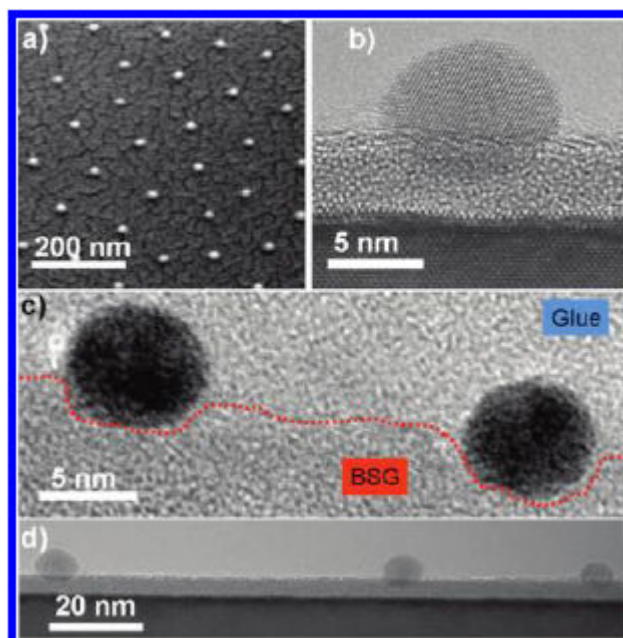


Figure 3. 34: Electron micrographs of Au nanoparticles on borosilicate glass and SiO_x/Si substrates: (a) SEM image showing a tilted view (45°) of Au nanoparticles on a borosilicate glass. HRTEM images of Au nanoparticles on SiO_x/Si (b,d) and glass (c) substrates after a H₂ plasma burning process. (b) Zoom-in image of a Au nanoparticle with a diameter of about 9 nm. The particle is partly embedded in an amorphous SiO_x layer. (c) Au nanoparticles partially embedded in a topographically rough glass substrate as compared to the relatively flat SiO_x/Si substrate shown in panel d. (Taken from Ref 21 without permission)

After learning the effect of plasma on silicon substrates, weakening of the particle/substrate interaction by controlled chemical etching of oxide layer was tried. The controlled chemical etching of oxide layer was achieved by use of HF as etchant and NH₄F

as buffer. However, transfer printing studies on these samples did not yield any noticeable result. Besides, ultrasonication was applied to glass substrates coated with nanoparticles but most of the time particles were not removed. The summary of particle-substrate interaction weakening experiments is given in Table 3. 6.

Name	Substrate	Explanation
Heating	Silicon	Heated to 275 C
Water immersion	Silicon	Waited 15 hours
Ultrasonic bath	Silicon	Both with water and acetone for 2 hours
Ultrasonic bath	Glass	Both in water and in empty bottle for 90 seconds. For empty bottle particles were removed only 1 time
Chemical Etching	Silicon	HF(40 μ l):NH ₄ F(0.148 mg) solution (50 ml water was used, Si substrates immersed 10-15 seonds

Table 3. 6: Summary of experiment for weakening particle-substrate interaction

3.5.2 PMMA Results

In the literature, PDMS was cited as soft elastomer and lacking resolution in sub – 100 nm region. As an alternative, the harder PMMA was considered^{22,23} for detaching the nanoparticles from the glass substrate. Since a mechanical adhesive force (by PMMA encapsulation upon heating over T_g) was expected, to facilitate the transfer, in addition to heating, cooling with liquid N₂ step was explored. The reason for the cooling step is twofold: (1) after heating PMMA above its T_g , silicon and glass substrates stick to each other very strongly and upon cooling, easy removal was achieved; (2) iduring the harsh milling conditions of TEM cross-section sample preparation, nanoparticles on glass were observed to have been removed, when they were brought to liquid N₂ temperatures. The schematic illustration of the experimental procedure is given in Figure 3. 35.

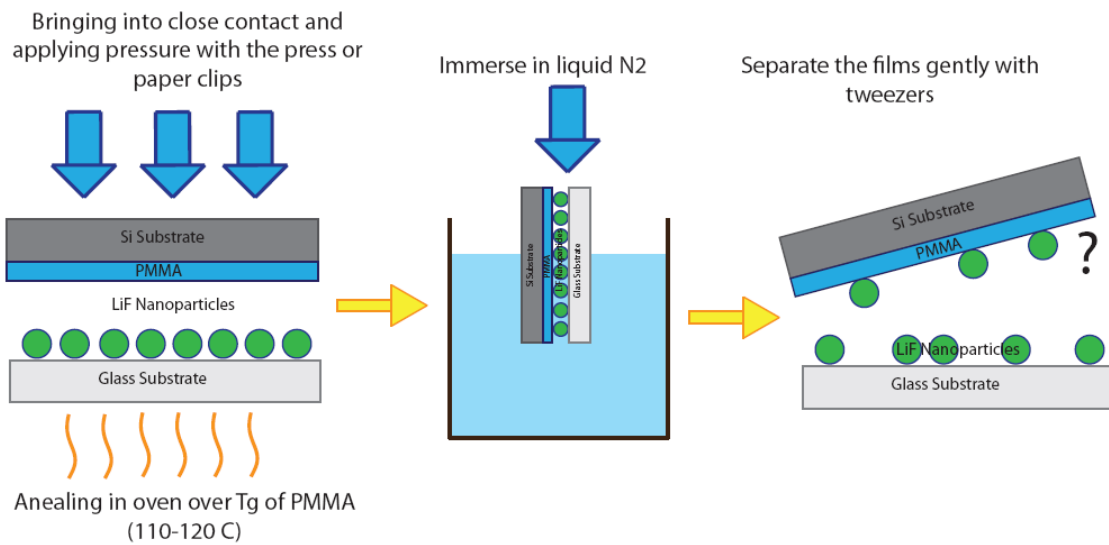


Figure 3. 35: Schematic illustration of heating/cooling experiments with PMMA

The annealing and cooling steps were performed for at least 60 minutes and 15 minutes, respectively. However, because a good transfer was not achieved, these times were altered sometimes. One of the most promising results for a PMMA heating-cooling experiment is given in Figure 3. 36. The image belongs to the PMMA surface, after the experiment. The sizes and separation of the nano sized objects matches with the donor substrate used and hence these particles can be thought as LiF nanoparticles. Although this result was promising, the transferred nanoparticle pattern was observed only in a very small region of PMMA. Moreover, this quality of transfer was not ever achieved again in these experiments. Even it could have been achieved; the difficulty of searching for a small nanoparticle transferred region did not allow imaging, such a region with SEM. Therefore, the further experiments were not done with this experimental procedure.

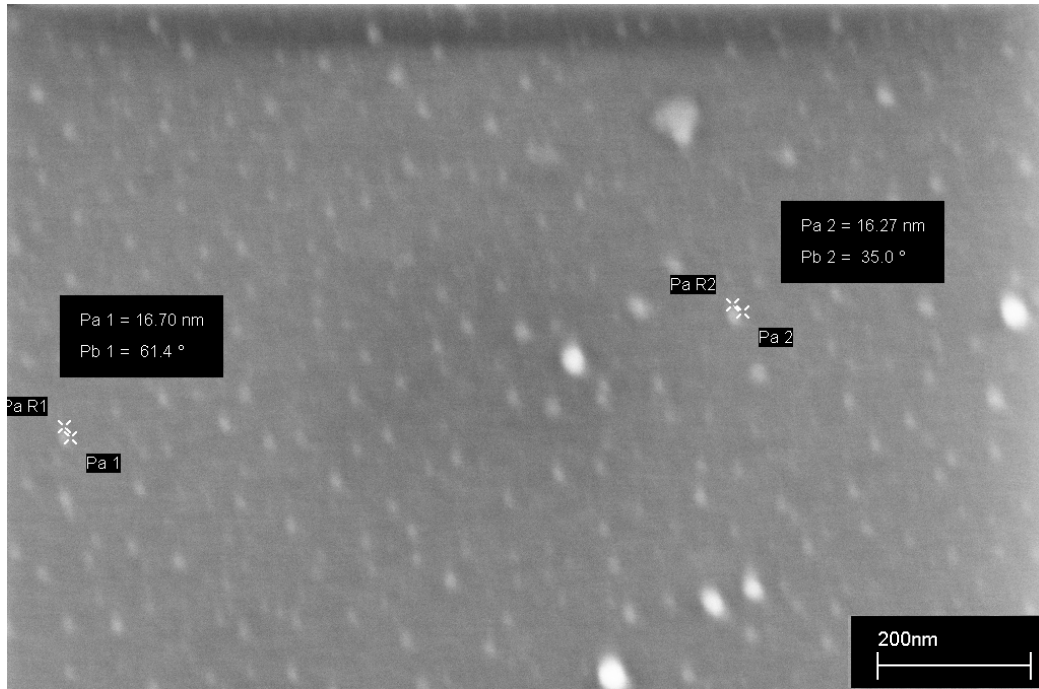


Figure 3. 36: SEM image of PMMA surface after heating-cooling experiment.

Donor: Receiver	Explanation
Glass - PMMA on Si	Two substrates brought to contact, heated to 120, cooled by Cu finger in $N_{2,liq}$
Glass - PMMA on Si	Two substrates brought to contact, heated to 150, cooled by Cu finger in $N_{2,liq}$
Glass - PMMA on Si	Two substrates brought to contact, heated to 120, cooled by direct immersion to $N_{2,liq}$
Glass - PMMA on Si	Two substrates brought to contact, heated to 150, cooled by direct immersion to $N_{2,liq}$
Glass - PMMA on Si	Two substrates brought to contact with paper clips, heated to 120, cooled by direct immersion to $N_{2,liq}$
Glass - PMMA on Si	Two substrates brought to contact with paper clips, heated to 150, cooled by direct immersion to $N_{2,liq}$
Glass - PMMA on Si	Two substrates brought to contact with better paper clips, heated to 120, cooled by direct immersion to $N_{2,liq}$

Table 3. 7: Summary of PMMA cooling/heating experiments

3.5.3 Electrostatic Charging Results

Poly(methyl methacrylate) (PMMA) can be used as a charge storing medium in order to achieve patterning of nanostructures, especially nanoparticles through Coulomb forces. Whitesides and coworkers first introduced the technique to show the patterning and transfer printing of submicrometer particles with this method²⁴. First of all, a set-up (as shown in Figure 3. 37) was used to charge the PMMA thin films on silicon substrate. External voltage source was used to apply electrical potential of 10-20V sweep with steps of 350 mV which takes 25 seconds. Then, charged PMMA substrates were brought to contact with LiF nanoparticles. Representative SEM images from this experiment are shown in Figure 3. 38. From these images it can be said that there is some interaction between charged PMMA and glass substrate. Some bigger particles seemed to be transferred from glass to charged PMMA layer. However, for smaller particles which are around 15 nm the disappearance was not observed in a big region. After this experiment, additional experiment was performed, but this time, the stamp (that is constituted by PDMS coated with cold) was spin coated with LiF loaded micelles and O₂ plasma etched afterwards. Then the potential was applied between stamp and PMMA coated on silicon as shown in Figure 3. 39. However, again a notable result could not be obtained. The reason may lie in the low dimension of particles, and less polarizability in this limit (although LiF itself is a polarizable material in bulk form). The summary of all charging experiments is given in Table 3. 8.

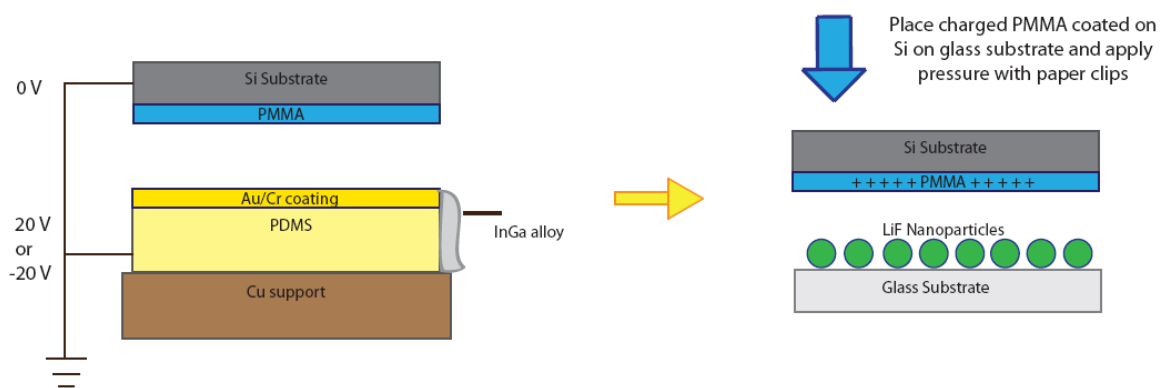


Figure 3. 37: Schematic illustration of PMMA charging experiments

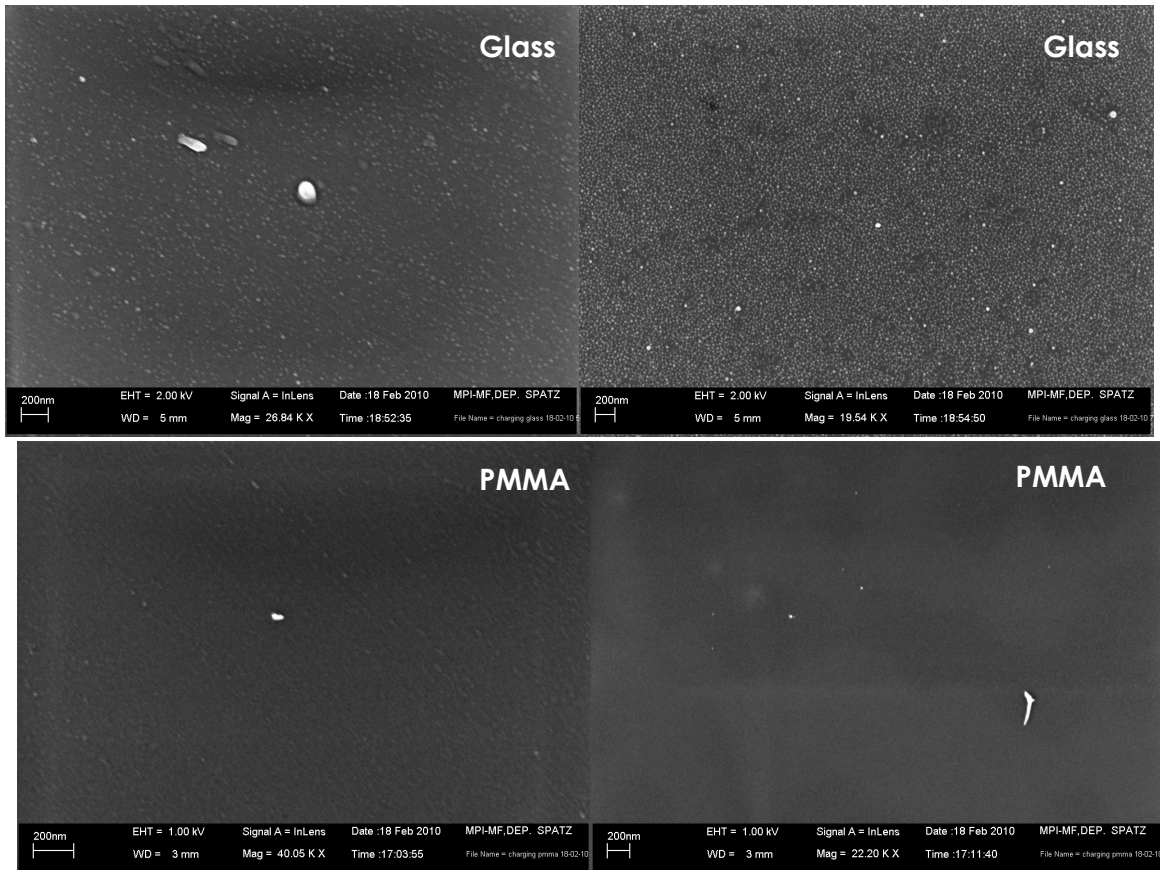


Figure 3. 38: SEM results of charging experiments. Both PMMA and glass surfaces are shown after experiment.

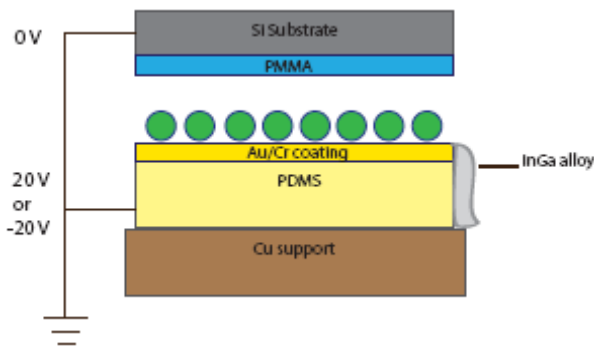


Figure 3. 39: Schematic illustration of direct charging experiment

Donor Substrate	Potential Applied to PDMS	Time (s)	Explanation
Glass with LiF	0 - (+)20 V	40	(+) PMMA pressed on donor for 1h
Glass with LiF	0 - (-)20 V	40	(-) PMMA pressed on donor for 1h
Glass with LiF	+20 V	50	(+) PMMA pressed on donor for 2h
Glass with LiF	-20 V	50	(-) PMMA pressed on donor for 2h
Glass with LiF	+40 V	50	(+) PMMA pressed on donor for 1h
Glass with LiF	-40 V	50	(-) PMMA pressed on donor for 1h
LiF coated on Au	+20 V	50	LiF on Au/PDMS direct charging

Table 3. 8: Summary of charging experiments

3.5.4 Adhesive Tape Experiments

Actually adhesive tape experiment was one of the first experiments performed for nano transfer printing studies. However, because the initial substrate was Si which strongly grabs the nanoparticles with the additional oxide layer formed after plasma etching step, particles were unaffected by adhesive tape. After changing the potential substrate as glass for nanotransfer experiments, adhesive tape experiment was repeated. In addition, before trying any commercial adhesive tapes, initially we used scotch tape which is frequently used in laboratory and ready in hand.

Initially very basic experiments were carried out with scotch tape. The tape was overlaid on LiF nanoparticle coated glass substrates and pressure was applied by the back side of Teflon tweezers (see Figure 3. 40 below). Then scotch tape was taken in a fast manner to assist grabbing of particles. Two surfaces were analyzed by SEM to find transfer regions.

The best results obtained with this experiment are given in Figure 3. 41 and Figure 3. 42. It was good to observe the removal of nanoparticles even with the basic scotch tape. However, large removal areas could not be obtained, possibly due to low adhesion strength and high rough surface of Scotch tape.

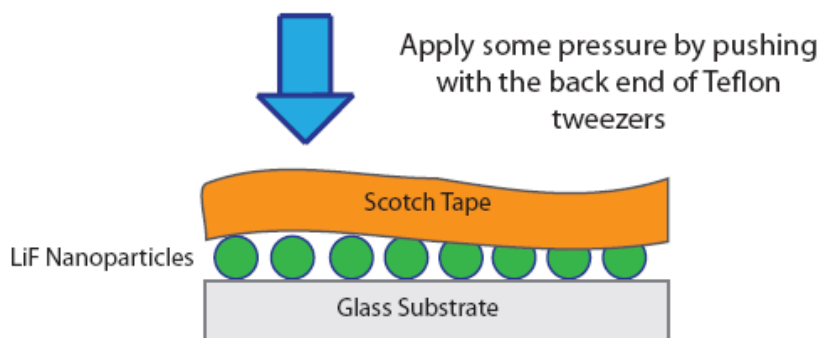


Figure 3. 40: Schematic illustration of a Scotch adhesive tape experiment

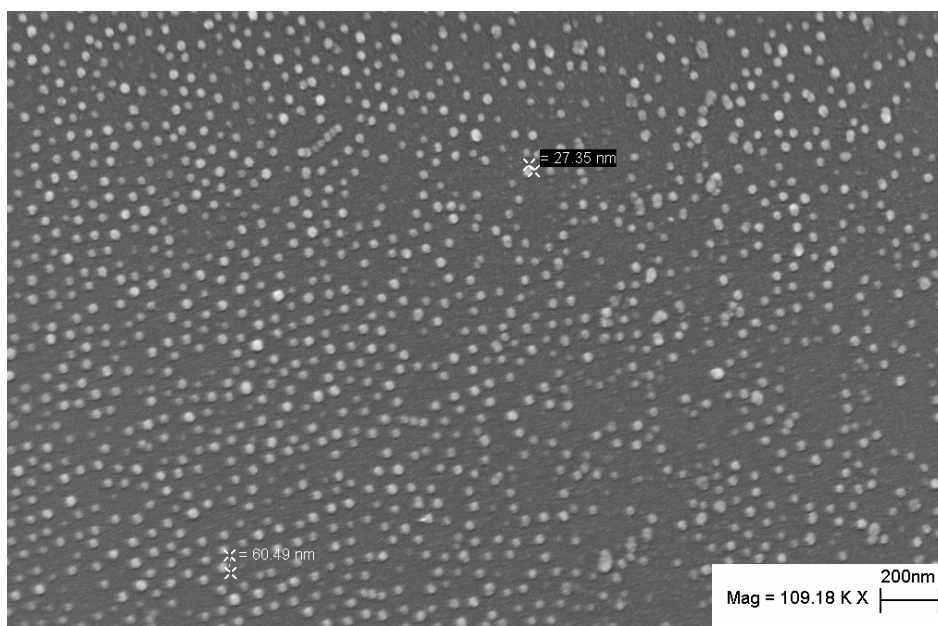


Figure 3. 41: SEM of LiF nanoparticle-coated-glass surface after transfer experiment

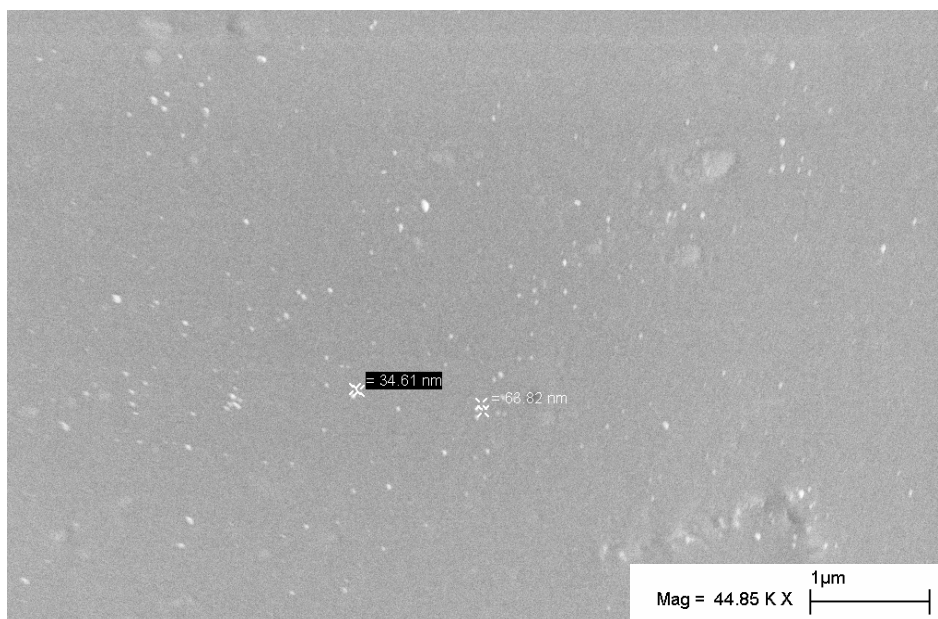


Figure 3. 42: SEM of adhesive tape surface after transfer experiment

After Scotch tape experiments, possible tape candidates were searched. As the result of searching process REVALPHA thermal release tape was chosen. The ability of this tape is that it loses its adhesive strength upon heating to the specified temperature. Therefore, if transfer of nanoparticles on thermal tape is achieved, that printing the particles on organic layers will be easy. For this purposes, direct sticking and peeling experiments were carried out as done with Scotch tape. Although single particle transfer from glass substrate to REVALPHA tape was obtained in several places, a collective transfer could not be obtained. Hence, rather than directly sticking and peeling, REVALPHA thermal release tape was adopted, wince it had proved useful for the transfer printing of graphene²⁵. The experimental procedure under consideration is given in Figure 3. 43.

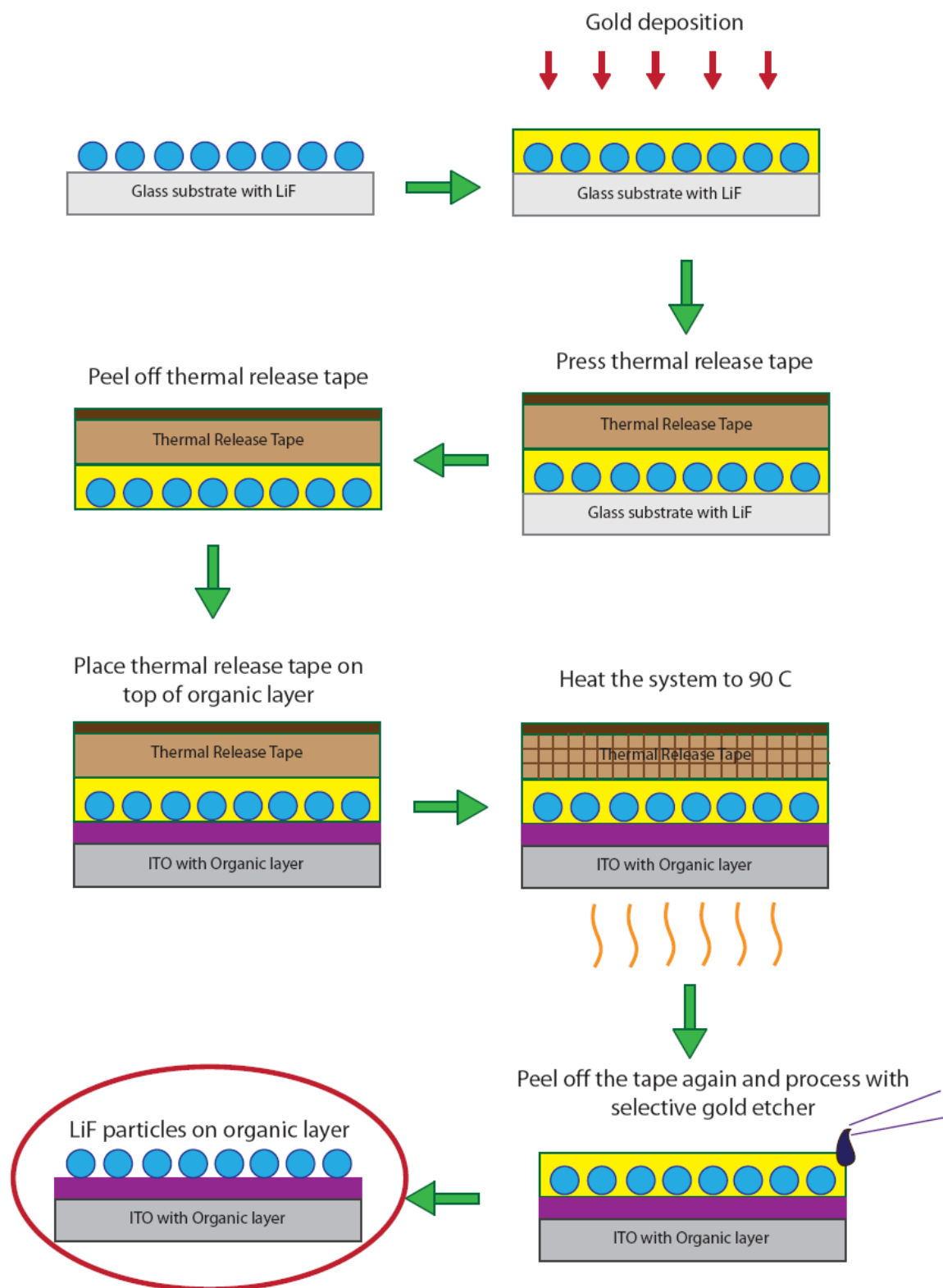


Figure 3. 43: Schematic illustration of transfer printing experiment that will be carried out by REVALPHA thermal release tape

Only the peeling step was performed until now and AFM images of glass layer coated with LiF nanoparticles are given in Figure 3. 44. As it can be seen in the AFM image in the

right, upon peeling coated Au film from the surface, a decent amount of LiF particles were removed. This experiment gave the most promising result among all the transfer printing studies performed in this thesis study. Although here only the preliminary results are presented, with the optimization of the process with further studies, complete transfer of nanoparticles can be achieved by this method.

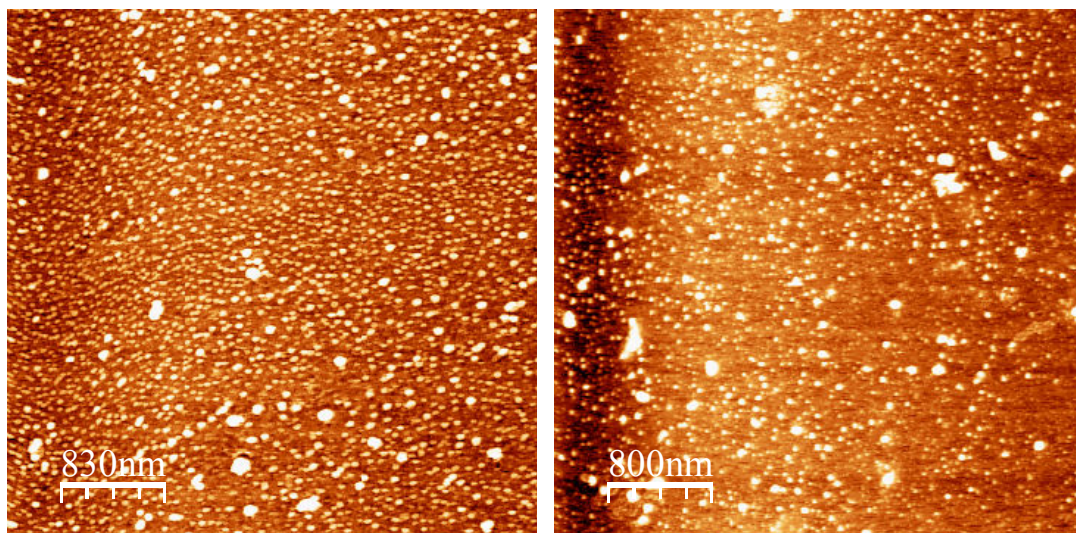


Figure 3. 44: AFM height images of glass substrate coated with LiF particles (x3), before (left) and after (right) peeling.

Chapter 3 References

1. Sarraf-Mamoory, R., Nadery, S., Riahi-Noori, N., The Effect of Precipitation Parameters on Preparation of Lithium Fluoride (LiF) Nano-Powder. *Chem Eng Commun* **194**, 1022-1028 (2007).
2. Kanamura, K., Shiraishi, S., Hideharu, T., Takehara, Z.-I., XPS Analysis of the Surface of a Carbon Electrode Intercalated by Lithium Ions. *Chem. Mater.* **9**, 1797-1804 (1997).
3. Kaestle, G., Boyen, H.-G., Weigl, F., Lengl, G., Herzog, T., Ziemann, P., Riethmüller, S., Mayer, O., Hartmann, C., Spatz, J. P., Moller, M., Ozawa, M., Banhart, F., Garnier, M. G., Oelhafen, P., Micellar Nanoreactors – Preparation and Characterization of Hexagonally Ordered Arrays of Metallic Nanodots. *Adv. Func. Mater.* **13**, 853-861 (2003).
4. Aytun, T., Mutaf, O. F., el-Atwani, O. J., Ow-Yang, C. W., Nanoscale Composition Mapping of Segregation in Micelles with Tapping-Mode Atomic Force Microscopy. *Langmuir* **24**, 14183-14187 (2008).
5. Aytun, T., Turak, A., Halek, G., Baikie, I., Maye, F., Ow-Yang, C. W., A Solution-Processed Alternative to Thermal Evaporated LiF in Electrode Bilayers. Manuscript submitted to *Appl. Phys. Lett.*
6. Hung, L. S., Tang, C. W., Mason, M. G., Enhanced electron injection in organic electroluminescence devices using an Al/LiF electrode. *Appl. Phys. Lett.* **70**, 152-154 (1997).
7. E. Ahlswede, J. Hanisch, and M. Powalla, *Appl. Phys. Lett.* **90** (2007).
8. Feng, X. D., Huang, C. J., Lui, V., Khangura, R. S., Lu, Z. H., Ohmic cathode for low-voltage organic light emitting diodes. *Appl. Phys. Lett.* **86**, 143511 (2005).
9. Nunzio, P. E., Fornarini, L., Martelli, S., Montereali, R. M., Texture Analysis of LiF Thin Films Evaporated onto Amorphous Substrates at Different Temperatures. *Phys Status Solidi A* **164**, 747-756 (1997).
10. Kim, J. S., Lagel, B., Moons, E., Johansson, N., Baikie, I. D., Salaneck, W. R., Friend, R. H., Cacialli, F., Kelvin probe and ultraviolet photoemission measurements of indium tin oxide work function: a comparison. *Synth. Met.* **111**, 311-314 (2000).
11. Lin, Y. J., Baikie, I. D., Chou, W. Y., Lin, S. T., Changes in surface roughness and work function of indium-tin-oxide due to KrF excimer laser irradiation. *J. Vac. Sci. Technol. A* **23**, 1305 (2005).

12. Schlaf, R., Parkinson, B. A., Lee, P. A., Nebesny, K. W., Jabbour, G., Kippelen, B., Peyghambarian, N., Armstrong, N. R., Photoemission spectroscopy of LiF coated on Al and Pt electrodes. *J. Appl. Phys.* **84**, 6729 (1998).
13. Prada, S., Martinez, U., Pacchioni, G., Work function changes induced by deposition of ultrathin dielectric films on metals: A theoretical analysis. *Phys. Rev. B* **78**, 235423 (2008).
14. Zhao, J. M., Zhang, S. T., Wang, X. J., Zhan, Y. Q., Wang, X. Z., Zhong, G. Y., Wang, Z. J., Ding, X. M., Huang, W., Hou, X. Y., Dual role of LiF as a hole-injection buffer in organic light-emitting diodes. *Appl. Phys. Lett.* **84**, 2913-2315 (2004).
15. Zhu, F., Low, B., Zhang, K., Chua, S., Lithium-fluoride-modified indium tin oxide anode for enhanced injection in phenyl-substituted polymer electroluminescent devices. *Appl. Phys. Lett.* **79**, 1205-1207 (2001).
16. Zhao, Y., Liu, S. Y., Hou, J. Y., Effect of LiF buffer layer on the performance of organic electroluminescent devices. *Thin Solid Films* **397**, 208-210 (2001).
17. Milliron, D. J., Hill, I. G., Shen, C., Kahn, A., Schwartz, J., Surface oxidation activates indium tin oxide for hole injection. *J. Appl. Phys.* **87**, 572 (2000).
18. Brabec, C. J., Shaheen, S. E., Winder, C., Sariciftci, N. S., Denk, P., Effect of LiF/metal electrodes on the performance of plastic solar cells. *Appl. Phys. Lett.* **80**, 1288-1290 (2002).
19. Scharber, M. C., Muhlbacher, D., Koppe, M., Denk, P., Waldauf, C., Heeger, A. J. Brabec, C. L., Design Rules for Donor in Bulk-Heterojunction Solar Cells-Towards 10% Energy-Conversion Efficiency. *Adv. Mater.* **18**, 789-794 (2006).
20. Hur, S.-H., Khang, D.-Y., Kocabas, C., Rogers, J. A., Nanotransfer printing by use of noncovalent surface forces: Applications to thin-film transistors that use single-walled carbon nanotube networks and semiconducting polymers. *Appl. Phys. Lett.* **85**, 5730-5732 (2004).
21. Mbenkum, B. N., Schneider, A. S., Schütz, G., Xu, C., Richter, G., van Aken, P. A., Majer, G., Spatz, J. P., Low-Temperature Growth of Silicon Nanotubes and Nanowires on Amorphous Substrates. *ACS Nano* **4**, 1805-1812 (2010).
22. Goh, C., Coakley, K. M., McGehee, M. D., Nanostructuring Titania by Embossing with Polymer Molds Made from Anodic Alumina Templates. *Nano Lett.* **5**, 1545-1549 (2005).

23. Gates, B. D., Xu, Q., Stewart, M., Ryan, D., Willson, C. G., Whitesides, G. M., New Approaches to Nanofabrication: Molding, Printing, and Other Techniques. *Chem. Rev.* **105**, 1171-1196 (2005).
24. Jacobs, H. O., Whitesides, G. M., Submicrometer Patterning of Charge in Thin-Film Electrets. *Science* **291**, 1763-1766 (2001).
25. Song, L., Ci, L., Gao, W., Ajayan, P. M., Transfer Printing of Graphene Using Gold Film. *ACS Nano* **3**, 1353-1356 (2009).
26. McKenna, K. P., Shluger, A. L., Electron-trapping polycrystalline materials with negative electron affinity. *Nat. Mater.* **7**, 859-862 (2008).

CHAPTER 4. CONCLUSION

In this thesis, the synthesis of LiF nanoparticles by use of PS-*b*-P2VP reverse micelles was achieved for the first time. Initially, the prospective reactants, LiOH and HF, were combined in a toluene environment. XPS characterization on the reaction by-product confirmed the synthesis of LiF, by giving the expected binding energy peaks for Li and F atoms, and additionally cubic crystals LiF were observed with SEM. Diblock copolymer micelles were employed as true reactor vessels for the reaction of LiOH and HF to form LiF. The difficulty of the LiOH loading step was handled by using a longer molecular weight (polar) P2VP block, rather than a symmetric diblock copolymer, in order to improve the loaded micelle stability. The verification of the LiOH loading was done by dynamic light scattering. In the size distribution-intensity results, the 50-nm increase in the average diameter signified the success of LiOH loading. The formation of LiF inside the micelle was achieved with the addition of HF to the LiOH loaded micelle composite system. With electron and x-ray diffraction methods, LiF crystal structure patterns were extracted, proving the formation of LiF inside micelles.

Homogenous coating of the LiF loaded micelles were done by spin coating onto a variety of substrates. LiF loaded micelle solution with a concentration of 3mg/ml was spin coated at 2000 rpm, giving denser micelle coverage on the surface. Using a lower concentration or higher spin rates was observed to result in quasi-hexagonal close packed arrangement. In order to remove the polymeric micelle without disturbing the particle arrangement on the surface, O₂ plasma etching was performed to LiF loaded micelles. By the removal of micelles, naked particles were obtained on the surface with monolayer coverage. Verification of LiF nanoparticles on the surface upon removal micelle was done by grazing incidence x-ray diffraction from a synchrotron source. Therefore, the stability of naked nanoparticles on substrate after O₂ plasma was validated.

To assess the performance of synthesized LiF nanoparticles for possible device application, inverted organic diode was fabricated and I-V characteristics were compared to the same device produced with thermally evaporated LiF. The device configurations were Al/LiF/C₆₀/LiF/Al/ITO for thermally evaporated LiF (thermo-LiF) and Al/LiF/C₆₀/LiF_{NANO}/Al/ITO for micelle assisted LiF nanoparticles (sol-LiF) (denoted as

LiF_{NANO}). Although the complexity of production of the device with micelle assisted LiF and brief air exposure of Al cathode, ohmic behavior was observed in most of the I-V measurements of both devices. Ohmic behavior of an organic device is particularly important because this is attained by insertion of LiF between organic layer and Al layer. To further evaluate the potential device application, work function measurements were performed with Kelvin probe (KP) for ITO electrodes coated with thermo-LiF and sol-LiF. For thermo-LiF, the work function of the electrode was decreased (negative $\Delta\Phi$) as expected. However, the work function of ITO was increased (positive $\Delta\Phi$) with sol-LiF and this was not expected. In terms of organic light emitting diode performance (OLED), having thermo-LiF on ITO side is more advantageous because this way the barrier for hole injection is increased and charge balance for electron-hole combination can be achieved. For organic photovoltaics (OPVs) case, having sol-LiF is more advantageous because ITO work function level can be aligned with valence band of PEDOT:PSS, a common hole transport layer in OPVs, by the increase resulted from sol-LiF. For Al cathode side of OPVs, sol-LiF can be a good candidate. Although sol-LiF widens the energy level difference between conduction band of C₆₀ and Al, it may still do its function because it decreases the barrier height, This is also validated by the ohmic contact behavior in the fabricated organic diode and as the objective of this thesis to produce LiF nanoparticle films for OPVs, this may be a good proof of concept. However, in order to conclude this discussion, an organic device should be made from sol-LiF and device performance should be compared with same device made from thermo-LiF.

The possible mechanism for thermo-LiF to decrease the work function can be electrostatic compression and overspill electron cloud from ITO surface. On the other hand, charge transfer should be occurred to increase the work function and in sol-LiF case some electrons must be transferred from ITO. The reason of the charge transfer for sol-LiF case can be attributed to high texturing and polycrystalline structure of LiF in this case as observed in ring electron diffraction patterns because high electron trapping behavior of grain boundaries of LiF was previously reported in the literature. The scientific basis of work function alteration anomaly for LiF produced with two different methods can be better understood with further TEM analysis.

In order to build the desired OPVs, LiF should be coated on organic layers and Al cathode should be deposited in vacuum environment. The micelle technique does not allow direct coating of nanoparticles on organic layers because O₂ plasma is required to remove

micelles and this damages the organic layers as well. For this purposes, several transfer printing studies based on non covalent forces were carried out in this thesis. Initially, it was observed that the donor substrate used for LiF nanoparticles was very effective to achieve particle removal. For silicon substrate particles were almost immobile and this is resulted from the additional oxide growth during O₂ plasma. On the other hand, particles were mobile on glass substrate that even with the scratch of tweezers some particles can be ripped off from the surface. Then, as the material for grabbing LiF nanoparticles from glass surface, PDMS and PMMA were used. Although PDMS was able to grab LiF powder, it was found to be insensitive sub 100 nm structures because of its low elastic modulus. The make PDMS harder and more hydrophilic brief O₂ plasma treatment was performed but even this was not effective for removing particles and this can be attributed to high rough surface of PDMS. As harder material than PDMS, PMMA was used. Heating was applied to PMMA to encapsulate nanoparticles and cooling was applied to separate PMMA. Only for once, nanoparticles were transferred to a very small area on PMMA surface but the technique found to be non reproducible. For using Coulombic forces, charging experiments were performed with PMMA which can trap charges in its matrix. In this case, particles could not be removed, which might be due to the low polarizability of the nanoparticles and additionally, small size (20 nm) of particles may prevent a good contact to PMMA surface.

Lastly, Au coating and thermal release tape was used for nanoscale transfer printing experiment. Au has a much larger surface energy than glass substrate as LiF does and for that reason it is believed that Au can strongly adhere to LiF with the intimate contact formed by thermal evaporation of Au on LiF nanoparticle films directly. The transfer part of the process is achieved by adhesive thermal release tape which loses its stickiness upon heating. The preliminary results of the experiment showed promising removal of LiF nanoparticles from glass substrate. The process should be optimized to remove all LiF particles from the surface and release of the particles on organic surfaces should be elucidated with additional experiments.

Consequently, for further transfer printing studies at nanoscale, there are few important factors to be considered. Firstly, the stamp material should form conformal contact with the LiF nanoparticles. If the surface of the stamp material is rough, or its elastic modulus is small, nanoparticles will not interact strongly with the stamp material. As in charging experiments, even Coulombic forces may not be enough to remove the particles from the

surface. Beside this, even material can form an intimate contact, the forces should be sufficiently high to grab the nanoparticles. This was observed for PMMA heating experiments that heating the polymer over its T_g might help it to form a better contact with LiF nanoparticles however, possibly non covalent forces were not enough to transfer particles to PMMA side. Lastly, the method that is used to receive nanoparticles from glass surface should be double acting, and allow printing of nanoparticles on organic layers. Charging experiments were straightforward in that sense because the charges on PMMA can easily be manipulated. Similarly, PDMS experiments were important because PDMS is an adhesive elastomer but its low surface energy makes it possible to transfer materials from PDMS to other surfaces which mostly have higher surface energy with comparison to PDMS.